Jordan Journal of Mechanical and Industrial Engineering (JJMIE)

JJMIE is a high-quality scientific journal devoted to fields of Mechanical and Industrial Engineering. It is published by Hashemite University in cooperation with the Jordanian Scientific Research and Innovation Support Fund, Ministry of Higher Education and Scientific Research.

SUBMISSION ADDRESS:

Prof. Moh'd Sami Ashhab, Editor-in-Chief
Jordan Journal of Mechanical & Industrial Engineering,
Hashemite University,
PO Box 330127, Zarqa, 13133 , Jordan
E-mail: jjmie@hu.edu.jo

Hashemite Kingdom of Jordan

Hashemite University

Jordan Journal of Mechanical and Industrial Engineering

JJMIE

An International Peer-Reviewed Scientific Journal

Financed by Scientific Research Support Fund

Volume 15, Number 5, December 2021

http://jjmie.hu.edu.jo/

ISSN 1995-6665

Jordan Journal of Mechanical and Industrial Engineering (JJMIE)

JJMIE is a high-quality scientific journal devoted to fields of Mechanical and Industrial Engineering. It is published by Hashemite University in cooperation with the Jordanian Scientific Research and Innovation Support Fund, Ministry of Higher Education and Scientific Research.

Introduction: The Editorial Board is very committed to build the Journal as one of the leading international journals in mechanical and industrial engineering sciences in the next few years. With the support of the Ministry of Higher Education and Scientific Research and Jordanian Universities, it is expected that a heavy resource to be channeled into the Journal to establish its international reputation. The Journal's reputation will be enhanced from arrangements with several organizers of international conferences in publishing selected best papers of the conference proceedings.

Aims and Scope: *Jordan Journal of Mechanical and Industrial Engineering* (JJMIE) is a refereed international journal to be of interest and use to all those concerned with research in various fields of, or closely related to, mechanical and industrial engineering disciplines. *Jordan Journal of Mechanical and Industrial Engineering* aims to provide a highly readable and valuable addition to the literature which will serve as an indispensable reference tool for years to come. The coverage of the journal includes all new theoretical and experimental findings in the fields of mechanical and industrial engineering or any closely related fields (Materials, Manufacturing, Management, Design, Thermal, Fluid, Energy, Control, Mechatronics, and Biomedical). The journal also encourages the submission of critical review articles covering advances in recent research of such fields as well as technical notes.

Guide for Authors

Manuscript Submission:
High-quality submissions to this new journal are welcome now and manuscripts may be either submitted online or email.

Online: For online and email submission upload one copy of the full paper including graphics and all figures at the online, submission site, accessed via http://jjmie.hu.edu.jo. The manuscript must be written in MS Word Format. All correspondence including notification of the Editor's decision and requests for revision, takes place by e-mail and via the Author's homepage, removing the need for a hard-copy paper trail

Submission address and contact :
Prof. Moh'd Sami Ashhab
Editor-in-Chief
Jordan Journal of Mechanical & Industrial Engineering, Hashemite University
PO Box 330127, Zarqa, 13115, Jordan
E-mail: jjmie@hu.edu.jo

Types of contributions*:* Original research papers and Technical reports

Corresponding author: Clearly indicate who is responsible for correspondence at all stages of refereeing and publication, including post-publication. Ensure that telephone and fax numbers (with country and area code) are provided in addition to the e-mail address and the complete postal address. Full postal addresses must be given for all co-authors.

Original material: Submission of an article implies that the work described has not been published previously (except in the form of itstan abstract or as part of a published lecture or academic thesis), that it is not under consideration for publication elsewhere, tha publication is approved by all authors and that, if accepted, it will not be published elsewhere in the same form, in English or in any other language, without the written consent of the Publisher. Authors found to be deliberately contravening the submission guidelines on originality and exclusivity shall not be considered for future publication in this journal.

Withdrawing: If the author chooses to withdraw his article after it has been assessed, he shall reimburse JJMIE with the cost of reviewing the paper.

Manuscript Preparation:

General: Editors reserve the right to adjust style to certain standards of uniformity. Original manuscripts are discarded after .publication unless the Publisher is asked to return original material after use. Please use MS Word for the text of your manuscript

Structure: Follow this order when typing manuscripts: Title, Authors, Authors title, Affiliations, Abstract, Keywords, Introduction, Main text, Conclusions, Acknowledgements, Appendix, References, Figure Captions, Figures and then Tables. Please supply figures imported into the text AND also separately as original graphics files. Collate acknowledgements in a separate section at the end of the article and do not include them on the title page, as a footnote to the title or otherwise.

Text Layout: Use 1.5 line spacing and wide (3 cm) margins. Ensure that each new paragraph is clearly indicated. Present tables and figure legends on separate pages at the end of the manuscript. If possible, consult a recent issue of the journal to become familiar with layout and conventions. All footnotes (except for table and corresponding author footnotes) should be identified with superscript Arabic numbers. To conserve space, authors are requested to mark the less important parts of the paper (such as records of experimental results) for printing in smaller type. For long papers (more than 4000 words) sections which could be deleted without destroying either the sense or the continuity of the paper should be indicated as a guide for the editor. Nomenclature should conform to that most frequently used in the scientific field concerned. Number all pages consecutively; use 12 or 10 pt font size and standard fonts.

<u>Corresponding author</u>: Clearly indicate who is responsible for correspondence at all stages of refereeing and publication, including post-publication. The corresponding author should be identified with an asterisk and footnote. Ensure that telephone and fax numbers (with country and area code) are provided in addition to the e-mail address and the complete postal address. Full postal addresses must be given for all co-authors. Please consult a recent journal paper for style if possible.

<u>Abstract:</u> A self-contained abstract outlining in a single paragraph the aims, scope and conclusions of the paper must be supplied.

<u>Keywords</u>: Immediately after the abstract, provide a maximum of six keywords (avoid, for example, 'and', 'of'). Be sparing with abbreviations: only abbreviations firmly established in the field may be eligible.

<u>Symbols:</u> All Greek letters and unusual symbols should be identified by name in the margin, the first time they are used.

<u>Units</u>: Follow internationally accepted rules and conventions: use the international system of units (SI). If other quantities are mentioned, give their equivalent quantities in SI

<u>Maths:</u> Number consecutively any equations that have to be displayed separately from the text (if referred to explicitly in the text).

<u>References</u>: All publications cited in the text should be presented in a list of references following the text of the manuscript.

Text: Indicate references by number(s) in square brackets in line with the text. The actual authors can be referred to, but the reference number(s) must always be given.

List: Number the references (numbers in square brackets) in the list in the order in which they appear in the text.

<u>Examples</u>:
<u>Reference to a journal publication:</u>
[1] M.S. Mohsen, B.A. Akash, "Evaluation of domestic solar water heating system in Jordan using analytic hierarchy process". Energy Conversion & Management, Vol. 38 (1997) No. 9, 1815-1822.

<u>Reference to a book:</u>
[2] Strunk Jr W, White EB. The elements of style. 3rd ed. New York: Macmillan; 1979.

<u>Reference to a conference proceeding:</u>
[3] B. Akash, S. Odeh, S. Nijmeh, "Modeling of solar-assisted double-tube evaporator heat pump system under local climate conditions". 5th Jordanian International Mechanical Engineering Conference, Amman, Jordan, 2004.

<u>Reference to a chapter in an edited book:</u>
[4] Mettam GR, Adams LB. How to prepare an electronic version of your article. In: Jones BS, Smith RZ, editors. Introduction to the electronic age, New York: E-Publishing Inc; 1999, p. 281-304

<u>Free Online Color</u> : If, together with your accepted article, you submit usable color and black/white figures then the journal will ensure that these figures will appear in color on the journal website electronic version.

<u>Tables:</u> Tables should be numbered consecutively and given suitable captions and each table should begin on a new page. No vertical rules should be used. Tables should not unnecessarily duplicate results presented elsewhere in the manuscript (for example, in graphs). Footnotes to tables should be typed below the table and should be referred to by superscript lowercase letters.

<u>Notification</u>: Authors will be notified of the acceptance of their paper by the editor. The Publisher will also send a notification of receipt of the paper in production.

<u>Copyright</u>: All authors must sign the Transfer of Copyright agreement before the article can be published. This transfer agreement enables Jordan Journal of Mechanical and Industrial Engineering to protect the copyrighted material for the authors, but does not relinquish the authors' proprietary rights. The copyright transfer covers the exclusive rights to reproduce and distribute the article, including reprints, photographic reproductions, microfilm or any other reproductions of similar nature and translations.

<u>Proof Reading</u>: One set of page proofs in MS Word format will be sent by e-mail to the corresponding author, to be checked for typesetting/editing. The corrections should be returned within 48 hours. No changes in, or additions to, the accepted (and subsequently edited) manuscript will be allowed at this stage. Proofreading is solely the author's responsibility. Any queries should be answered in full. Please correct factual errors only, or errors introduced by typesetting. Please note that once your paper has been proofed we publish the identical paper online as in print.

JJMIE

Volume 15, Number 5, December. 2021
ISSN 1995-6665

Jordan Journal of Mechanical and Industrial Engineering

PAGES	PAPERS

JJMIE

Volume 15, Number 5, December. 2021
ISSN 1995-6665
Pages 411 - 417

Jordan Journal of Mechanical and Industrial Engineering

Improving Mechanical Properties of Rice Husk and Straw Fiber Reinforced Polymer Composite through Reinforcement Optimization

Sachin G Ghalme

Mechanical Engineering Department, Sandip Inst. of Tech. and Research Centre, Nashik (MS), India

Received May 1 2021 *Accepted October 6 2021*

Abstract

The generation of lignocellulosic agriculture waste and the residue is unavoidable, and disposal of the same with burning or burying creates environmental issues. In recent years the scientific community is continuously looking for sustainable development using natural resources for development. Rice husk (RH) and straw (RS) are already proposed as natural fiber reinforcing materials for natural fiber reinforced polymer composite (NFRPC). In this article, an attempt has been made to obtain the optimized proportion of rice husk and straw reinforcement in bio epoxy resin for the development of rice husk and straw fiber-reinforced hybrid composite with improved mechanical properties. The grey relational analysis (GRA) methodology is implemented to obtain the optimized proportion of RH and RS for maximization of tensile and flexural strength of polymer composite simultaneously. The experimental and grey relational analysis result presents the addition of 05 and 08 wt% of RS and RH fiber respectively in bio epoxy resin presents rice straw and husk reinforced polymer composite with improved tensile and flexural strength simultaneously.

Keywords: Natural fiber reinforced polymer composite (NFRPC), rice husk (RH), rice straw (RS), mechanical properties, grey relational analysis (GRA);

1. Introduction

Polymer composite has presented itself as advanced materials to satisfy the demand for the development of advanced engineered materials for various applications. Polymer composite shows different chemical constituents due to the continuous matrix phase and various reinforcements. Since composites are fabricated with two or more dissimilar materials, after utilization both materials cannot be easily recycled. They need to be dump in landfills or incinerated. Both these disposal alternatives are expensive, wasteful, and contribute to environmental pollution. The growing concern about the environmental issues and development of advanced materials has forced us to utilize the natural resources for the development of fiber polymer composite, which is environmentally friendly and does not cause any harm in terms of pollution and decompose effortlessly [1]. The requirement for sustainable development attracted the attention of the research community to utilize natural fibers as reinforcing material for polymer composites. Natural fibers are thread-like naturally available structures with a high aspect ratio. They are classified based on their source like vegetable fibers (abaca), animal fibers (silk) and mineral fibers (asbestos) [2]. The vegetable or plant fibers such as rice, groundnut, banana, coir, pineapple leaf, oil palm, flax, jute and many more are nowadays employed as natural reinforcement in polymer composite to replace synthetic fibers such as glass, carbon and Kevlar due to their biodegradability and low cost [3-5]. Plant fibers mainly consist of cellulose. The various examples are linen, jute, cotton, flax, sisal and hemp. These fibers are extracted from the fruits, seeds, leaves, stem and skin of plants. Based on this they are categorized as leaf fiber (collected from leaves, e.g. sisal and agave), seed fiber (collected from seeds or seed cases, e.g. cotton and kapok), bast fiber or skin fiber (collected from the skin or bast surrounding the stem, e.g. jute, kenaf, hemp, ramie, rattan, soyabean, vine and banana fibers), fruit fiber (collected from the fruit of the plant, e.g. coconut, coir fiber) and stalk fiber (stalks of the plant, e.g. straws of wheat, rice, barley and other crops including bamboo, grass and tree wood).

Natural fibers present significant mechanical properties, and in addition to this, they are renewable, eco-friendly, easy to be availabile, renewable, low price and density. They are alternatives to the synthetic fiber components such as glass, carbon used in the fabrication of polymer matrix composites and are significantly susceptible to microorganisms [6-8]. There are enormous applications of NFRP composites in the automotive and aerospace interior, packaging, consumer products, defence, civil, marine, sports and textile industries due to their higher specific properties along with sustainable development and disadvantages associated with the synthetic raw materials [9-12].

Rice is a substantial food crop in the agriculture sector belonging to cereal grains like wheat, barley, oat, and about 1% of the earth's surface comes under this food crop [13-

* Corresponding author e-mail: sachinghalme@hotmail.com.

15]. The rice husk and straw shown in Figure 1 are two major agricultural wastes generate during rice production.

(a) (b)

Figure 1. (a) Rice straw, (b) Rice husk

Rice straw belongs to the stalk fiber and covers a substantial portion of rice yield and is separated from rice using a machine or manually in the field itself. The vital application of rice straw is used as reinforcement for the structural board as it shows good sound-absorbing property [16]. Rice straw also contains cellulose, a potential material for composite. Rice husk is a secondary byproduct during the production of rice grain. It is nonedible hard protecting encapsulation of the rice grain, and for every 1000 Kg of rice paddy, about 20-30% husk is generated [13-18]. Rice husk is abrasive in nature along with low density, toughness and resistance to weathering. It is used as filler in construction and insulation materials, fuel and as composite for manufacturing of bricks, panels, decks, and window and door frames [19].

The main limiting factor associated with the application of NFRPC as reinforcement or filler is their dimensional instability due to their hydrophilic characteristic and poor water resistance. Availability of hydroxyl in cellulose is the main cause for swelling of NFRPCs as it has a tendency of bonding with hydrogen in water [20]. Several authors have studied the mechanical properties of rice straw fiber-reinforced polymer composite [21, 22].

Hybrid composites apply more than one reinforcement or matrix to generate composite with improved properties. M. A. Abd El-baky [23] evaluated the tensile and flexural properties of jute-glass-carbon fiber reinforced epoxy hybrid composite and presented that hybridization of process improved the tensile and flexural properties of jute reinforced composite. Pakravan et al. [24] blended RH with polyvinyl alcohol (PVA) fibers and used it as reinforcement for cementitious hybrid composite. They found improved mechanical properties along with the reduced density of composite due to hybridization. In another study, Jawad K. Oleiwi et al. [25] evaluated the flexural and impact properties of hybrid composite reinforced with bamboo and rice husk particles. They found that flexural and impact strength improved with small particle size and reinforcement concentration.

In earlier studies related to the RH and RS, the effect of individual reinforcement has been considered on mechanical properties. No study deals with hybridization. Optimization of process parameters or during product development help us to achieve a balance between input and output with aim of maximization or minimization of desired output [26,27]. The effect of combined RH and RS in epoxy resin is not evaluated in earlier studies. The current study is aimed at obtaining the optimum proportion of RH and RS in bio epoxy resin for maximizing the tensile and flexural strength of the NFRPC.

2. Materials and Method

2.1. Materials

Rice straws were collected from the local agriculture fields near our campus in Trimbakeshwar (Nashik) region, and husk was collected from local rice mills.

The matrix material used in this investigation was bio epoxy resin Grade Ly-556 and Hardener Hy-951, supplied by Lab Chemicals.

2.2. Methodology: Grey Relational Analysis (GRA)

To complete the systematic and statistical analysis of the experimental results, the experiments were planned and results were analysed with grey relational analysis (GRA). The GRA is a statistical technique implemented to optimize the multi-objective functions [28-31].

Normalization of Data

The collected raw experimental data is normalized into 0 or 1, with two criteria wise lower is better (LB) and higher is better (HB). A LB criterion is used to normalize data when the objective function is to minimize. Equation 1 is used for LB criteria. A HB criterion is used to normalize data when the objective function is to maximize. Equation 2 is used for HB criteria.

$$x_i(k) = \frac{\max y_i(k) - y_i(k)}{\max y_i(k) - \min y_i(k)} \tag{1}$$

$$x_i(k) = \frac{y_i(k) - \min y_i(k)}{\max y_i(k) - \min y_i(k)} \tag{2}$$

Where $x_i(k)$ is the value after the grey relational generation, $\min y_i(k)$ is the smallest value of $y_i(k)$ for the k^{th} response, and $\max y_i(k)$ is the largest value of $y_i(k)$ for the k^{th} response. $i = 1, 2, 3\ldots$ the number of experiments and $k = 1, 2, 3\ldots$ the number of responses.

In this study, I was expecting to maximize both tensile strength and flexural strength. So, Equation 2 is used to normalize experimental data.

Calculation of Grey Relational Coefficient (GRC)

GRC is calculated to determine the relation between ideal and actual normalized experimental data. GRC (ξ) is calculated using equation 3. A relation is established between actual values and normalized values of tensile strength and flexural strength using Equation 3.

$$\xi = \frac{\Delta_{\min} + \psi \Delta_{\max}}{\Delta_{oi}(k) + \psi \Delta_{\max}} \tag{3}$$

Where,

$$\Delta_{oi}(k) = \left\| x_o(k) - x_i(k) \right\|$$

The difference of the absolute value of $x_0(k)$ and $x_i(k)$; ψ is the distinguishing coefficient; $0 < \psi < 1$, Δ_{min} is the smallest value of $\Delta_{oi}(k)$ and Δ_{max} is the largest value of $\Delta_{0i}(k)$.

Calculation of Grey Relational Grade (GRG)

The analysis of multiple outputs characteristics is based on grey relational grade. This will convert multiple responses into a single numerical value. The GRG (γ) is an average sum of GRC and calculated using Equation 4. Its value lies between 0 and 1.

$$\gamma_i = \frac{1}{n}\sum_{k=1}^{n} \xi_i(k) \tag{4}$$

Where n is a number of process responses. In this work, tensile strength and flexural strength are two responses.

3. Experimental Work

3.1. Sample preparation

At first, the RH and RS fibers were ground and were washed thoroughly with water. After that, it was dried under direct sunlight for 8 hours. Then, RH and RS fibers were soaked separately in NaOH solution (1% NaOH powder & 99% distilled water) for 3 hours. After soaking, it was washed again with running water and dried under shade for another 4 hours to remove residual NaOH. Soaking of RH and RS in NaOH solution results in the removal of the natural fats and waxes from the surface. Thus, the removal of fats and waxes from the surface exposes it readily to available chemical reactive groups for interaction with the matrix material. The removal of surface impurities enhances surface roughness owing to the treatment of RH and RS with NaOH. Surface roughness makes the wetting (mechanical interlocking) favorable and leads to improved mechanical properties.

The various proportions of RH, RS and Resin selected are presented in Table 1, as shown above. To achieve the proper curing epoxy resin and hardener were added in the 10:1 proportion. The measured quantity of Resin & Hardener (10:1) was poured into the beaker and stirred well for 25 minutes to make a homogeneous mixture.

Then calculated quantities of RH and RS fibers were then mixed with epoxy & the mixture is stirred for another 30 minutes.

Thereafter, the obtained mixture was poured into metal moulds with different dimensions as per the requirement of the test standards. Silicon releasing agent was spread over the mould for easy removal of cured samples. The sample is then allowed to solidify for 12 hours.

3.2. Mechanical Testing

Tensile Test

Tensile testing is used to measure the force required to break a polymer composite specimen and the extent to which the specimen stretches or elongates to that breaking point. Tensile tests produce a stress-strain diagram, which is used to determine tensile modulus. The data is often used to specify a material to design parts to withstand application force and as a quality control check of materials.

The tensile test was conducted according to the ASTM D3039. The most common specimen for ASTM D3039 is a constant rectangular cross-section, 25 mm wide and 250 mm long, 4-5mm thick. Figure 2 shows the specimen used for the tensile test.

Figure 2. Tensile test specimen

During testing, the specimens were fixed in the grips of a Universal Test Machine. For ASTM D3039, the test speed can be determined by the material specification or time to failure (1 to 10 minutes). A typical test speed for standard test specimens is 2 mm/min (0.05 in/min). An extensometer or strain gauge is used to determine elongation and tensile modulus. The tensile load was applied until the final failure of the specimen. Tensile test data is helpful for the selection of material in the tensile application. Figure 3 shows the tensile test setup used for experimentation.

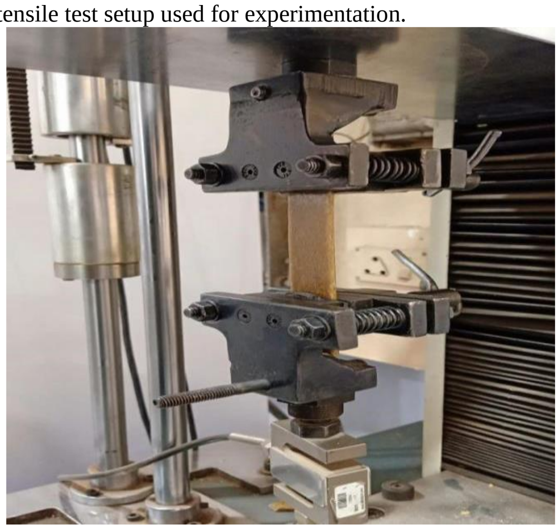

Figure 3. Tensile test setup

Flexural Test

The flexural test measures the force required to bend a beam under three-point loading conditions. The data is often used to select materials for parts that will support loads without flexing. Flexural modulus is used as an indication of a material's stiffness when flexed. The test was conducted according to ASTM D790. A variety of specimen shapes can be used for this test, but the most commonly used specimen size for ASTM is 3.2mm x 12.7mm x 125mm (0.125" x 0.5" x 5.0") and for ISO is 10mm x 4mm x 80mm. Figure 4 shows the specimen used for flexural testing.

Table 1. Compositional proportion

	Wt %														
RS	5	5	5	5	5	8	8	8	8	8	11	11	11	11	11
RH	5	8	11	14	17	5	8	11	14	17	5	8	11	14	17
Resin	90	87	84	81	78	87	84	81	78	75	84	81	78	75	72

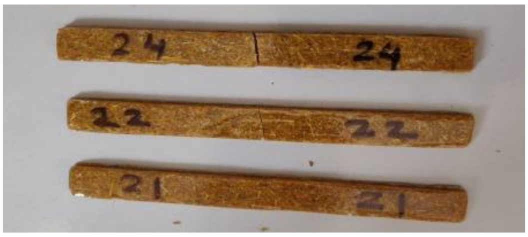

Figure 4. Flexural test specimen

During testing, the specimen lies on a support span, and the load is applied to the center by the loading nose producing three-point bending at a specified rate. The test parameters are the support span, the speed of the loading, and the maximum deflection for the test. These parameters are based on the test specimen thickness and are defined differently by ASTM and ISO. For ASTM D790, the test is stopped when the specimen reaches 5% deflection or the specimen breaks before 5% deflection. Figure 5 shows the setup used for flexural testing.

4. RESULTS AND DISCUSSION

The tensile and flexural tests were conducted as explained in the earlier section, and results are presented in Table 2. Each test was conducted 2 times, and the average value is presented in Table 2.

As presented in a table, the maximum value of tensile strength and flexural strength is different for different proportion. The composite with 5 wt% of RH and 8 wt% of RS provides maximum value for average tensile strength.

Figure 5. Flexural test setup

Table 2. Average values of tensile & flexural strength*

Expt. No.	RS (Wt%)	RH (Wt %)	Resin (Wt %)	Avg. Tensile Strength (N/mm^2)	Avg. Flexural Strength (N/mm^2)
1	5	5	90	16.25	26.995
2	5	8	87	18.095	33.335
3	5	11	84	17.015	31.12
4	5	14	81	15.07	36.04
5	5	17	78	15.675	29.1
6	8	5	87	12.295	32.97
7	8	8	84	15.57	35.52
8	8	11	81	14.34	36.825
9	8	14	78	12.28	31.76
10	8	17	75	12.91	35.695
11	11	5	84	11.835	32.7
12	11	8	81	12.13	36.655
13	11	11	78	12	34.05
14	11	14	75	10.125	24.785
15	11	17	72	14.05	23.645

*Testing at FAN Services, Advanced Materials Testing and Research Lab, Nashik

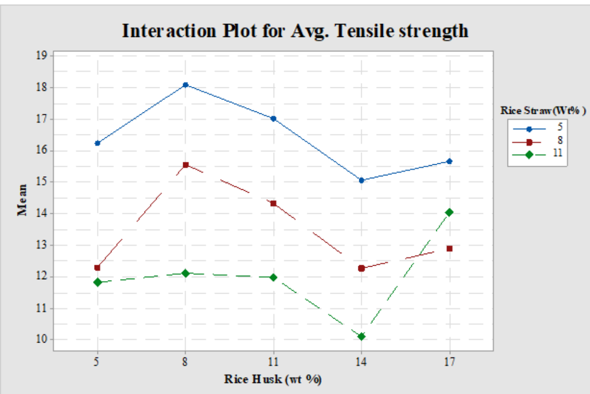

Figure 6. Interaction plot for avg. tensile strength

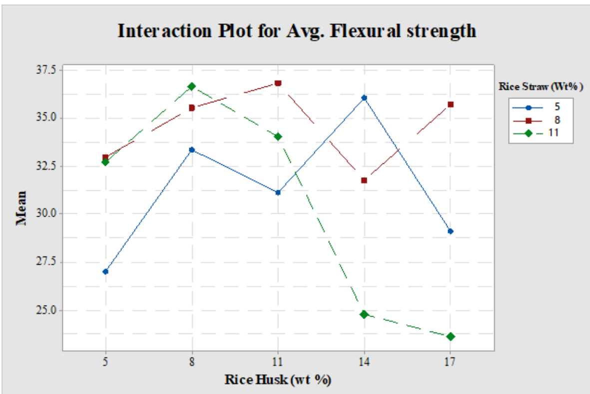

Figure 7. Interaction plot avg. flexural strength

As presented in the interaction plot for tensile strength, the rice straw and husk has a significant interactive effect on tensile strength value. At 8 wt% of RH, it provides the highest value for tensile strength for all proportions of RS. With a further increase in RH proportion, the tensile strength decreases up to 14 wt % and again further increases for 17 wt%.

On a similar line, we can observe the variation in flexural strength. At 8 wt% of RH and 11 wt% of RS, we can observe the maximum flexural strength. As presented in the interaction plot (Figure 7) for flexural strength, the rice straw and husk has a more significant interactive effect on flexural strength.

It is clear from the above analysis, that we are getting the maximum value for the tensile and flexural strength with different proportions of rice husk and straw. The specimen with a higher value of flexural strength may not provide sufficient strength in tensile conditions and vice versa.

Increasing one property may lead to compromise for another property, which is not acceptable in particular applications. In some applications, we are expecting the significant performance of NFRPC in both tensile and flexural/bending conditions. To obtain the maximum performance of specimen in both tensile and flexural testing, it is necessary to define the optimal proportion of reinforcing RH and RS to balance between tensile and flexural strength.

Grey relational analysis is a statistical technique for multi-objective optimization problems [32]. This technique helps to convert the multi-objective problem into a single objective. In this study, maximizing tensile and flexural strength are two objectives to achieve. For this objective, the optimization of RH and RS reinforcement is crucial. In this work, an attempt has been made to obtain the optimal proportion of RH and RS for maximizing tensile and flexural strength without compromising for another property. The results obtained in Table 2 were processed as per Equations 2 to 4 presented in earlier sections.

Both tensile and flexural strength were assigned an equal weightage of 50% for grey relational analysis. The results of the grey relational analysis are presented in Table 3. Weighted grey relational grade (GRG) and corresponding rank are presented in Table 3. In this table, the highest value of wt. GRG with rank 1 shows the optimal condition for RH and RS proportion for maximizing both tensile and flexural strength.

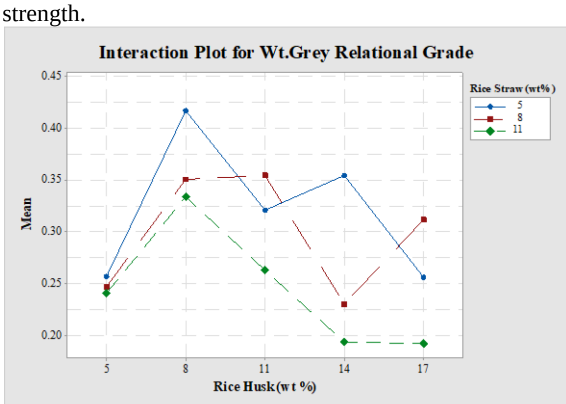

Figure 8. Interaction plot for wt. GRG

Figure 8 presents the interaction plot for a weighted grey relational grade. At 08 wt% of RH and 05 wt% of RS, we get the maximum value for weighted GRG, indicating the optimum proportion of the reinforcing materials for maximizing both properties simultaneously.

5. Analysis of variance (ANOVA)

Finally, Analysis of Variance (ANOVA) was performed to obtain the individual contribution of Wt% RS and RH for weighted Grey Relational Grade (Wt.GRG) or the individual contribution in mechanical properties. Analysis of Variance is a statistical technique that helps to identify the significance of the design/input parameter in relation to the output/desired parameter [33]. The analysis is carried out for the level of significance of 5% (the level of confidence is 95%). Table 4 shows the results of ANOVA.

It is clear from Table 4, that Wt% of RH has a significant contribution of about 51.38% in wt GRG with a P-value of 0.036 (< 0.05, significant). It is a more significant as a major factor contributing to the mechanical property improvement of NFRPC, while Wt% of RS has the contribution of about 25.20% in wt GRG or mechanical properties of NFRPC.

Table 3. Grey relational analysis

Expt. No.	RS (Wt %)	RH (Wt %)	Resin (Wt %)	Avg. Tensile Stren. (N/mm^2)	Avg. Flex. Strength (N/mm^2)	Wt. GRG	GRG Rank
1	5	5	90	16.25	26.995	0.257	9
2	5	8	87	18.095	33.335	0.417	1
3	5	11	84	17.015	31.12	0.321	6
4	5	14	81	15.07	36.04	0.355	3
5	5	17	78	15.675	29.1	0.256	10
6	8	5	87	12.295	32.97	0.247	11
7	8	8	84	15.57	35.52	0.351	4
8	8	11	81	14.34	36.825	0.355	2
9	8	14	78	12.28	31.76	0.23	13
10	8	17	75	12.91	35.695	0.312	7
11	11	5	84	11.835	32.7	0.241	11
12	11	8	81	12.13	36.655	0.334	5
13	11	11	78	12	34.05	0.263	8
14	11	14	75	10.125	24.785	0.194	14
15	11	17	72	14.05	23.645	0.192	15

Table 4. Analysis of Variance (ANOVA)

Source	DF	Seq. SS	Contribution	Adj SS	Adj MS	F-Value	P-Value
Wt% of Rice Straw	2	0.01545	25.20%	0.01545	0.007723	4.31	0.054
Wt% of Rice Husk	4	0.03149	51.38%	0.031499	0.007872	4.39	0.036 (sign.)
Error	8	0.01435	23.10%	0.001435	0.001497		
Total	14	0.06128	100%				

6. CONCLUSION

1. In the area of sustainable product development, a hybrid NFRPC of rice husk particles and rice straw has been developed and proposed with improved mechanical properties.
2. In the area of product development, it is always expected to optimize the proportion of Reinforcing 08 wt% of RH and 05 wt% of RS in polymer composite will provide us with significantly acceptable strength in both tensile and flexural loading conditions.
3. Reinforcing 08 wt% of RH and 05 wt% of RS in polymer composite will provide us with significantly acceptable strength in both tensile and flexural loading conditions.
4. From Analysis of Variance, it is clear that rice husk has significant contribution in improving mechanical properties of rice husk and straw fiber-reinforced polymer composite.

REFERENCES

[1] Jawaid M., and Abdul Khalil HPS, Cellulosic/synthetic fibre reinforced polymer hybrid composites: a review. Carbohydrate Polymers, 2011, 86, pp.1–18.

[2] Vijaya Ramnath B., Manickavasagam VM., Elanchezhian C., Vinodh Krishna C., Karthik S., Saravanan K. Determination of mechanical properties of intra-layer abaca–jute–glass fiber reinforced composite. Materials & Design, 2014, 60: 643–652.

[3] Senthilkumar K., Saba N., Rajini N., Chandrasekar M., Jawaid M., Sienghin S. et al. Mechanical properties evaluation of sisal fibre reinforced polymer composites: a review. Construction and Building Materials, 2018, 174:713.

[4] Lila MK., Singhal A., Banwait SS., Singh I. A recyclability study of bagasse fiber reinforced polypropylene composites. Polymer Degradation and Stability, 2018, 152:272.

[5] Monteiro SN., Calado V., Rodriguez RJS., Margem FM. Thermo gravimetric stability of polymer composites reinforced with less common lignocellulosic fibers-an overview. Journal of Material Research Technology, 2012, 1(2):117.

[6] Majeed K., Hassan A., Abu Bakar A. Barrier, Biodegradation, and mechanical properties of (Rice husk)/ (Montmorillonite) hybrid filler-filled low-density polyethylene nanocomposite films. Journal of Vinyl and Additive Technology, 2017, 23:162–171.

[7] George J., Kumar R., Jayaprahash C., Ramakrishna A., Sabapathy S., Bawa A. Rice bran-filled biodegradable low-density polyethylene films: Development and characterization for packaging applications. Journal of Applied Polymer Science, 2006, 102:4514–4522.

[8] Vaisanen T., Haapala A., Lappalainen R., and Tomppo L. Utilization of agricultural and forest industry waste and residues in natural fiber-polymer composites: A review. Waste Management, 2016, 54:62-73.

[9] Butylina S., Martikka O., Karki T. Thermal performance and optical properties of wood–polymer composites. Journal of Thermoplastic Composite Materials, 2013, 26:60–73.

[10] Jawaid M., Khalil HA. Cellulosic /synthetic fibre reinforced polymer hybrid composites: A review. Carbohydrate Polymer, 2011, 86:1–18.

[11] Layth M., Ansari M., Grace P., Mohammad J., Saiful Islam, M. A Review on Natural Fiber Reinforced Polymer Composite and Its Applications. International Journal of Polymer Science, Vol. 2015.

[12] Kin-tak L., Pui-yan H., Min-Hao Z., David H. Properties of natural fibre composites for structural engineering applications. Composites Part B: Engineering, 2018, 136:222–233.

[13] Adam F., Appaturi JN., and Iqbal A. The utilization of rice husk silica as a catalyst: review and recent progress. Catalysis Today, 2012, 190(1):2–14.

[14] Arjmandi R., Hassan A., Majeed K., et al. Rice husk filled polymer composites. International Journal of Polymer Science, 2015: 1–32.

[15] Faruk O., Bledzki AK., Fink H., et al. Biocomposites reinforced with natural fibers: 2000–2010. Progress in Polymer Science, 2012, 37(11): 1552–1596.

[16] Ramamoorthy SK., Skrifvars M. and Persson A. A review of natural fibers used in biocomposites: plant, animal and regenerated cellulose fibers. Polymer Reviews, 2015, 55(1): 107–162.

[17] Lim SL., Wu TY., Sim EYS., et al. Biotransformation of rice husk into organic fertilizer through vermicomposting. Ecological Engineering, 2012, 41:60–64.

[18] Aprianti E., Shafigh P., Bahri S., et al. Supplementary cementitious materials origin from agricultural wastes-a review. Construction and Building Materials, 2015, 74:176–187.

[19] Mohammed L., Ansari MNM., Pua G., et al. A review on natural fiber reinforced polymer composite and its applications. International Journal of Polymer Science, 2015, 1–15.

[20] Kabir M., Wang H., Lau K., Cardona F. Chemical treatments on plant-based natural fibre reinforced polymer composites: An overview. Composites Part B: Engineering, 2012, 43: 2883–2892.

[21] Sudhakar K., and Srinivas Ch. Investigation of Mechanical Properties of Rice Straw Fibre Polypropylene Composites. International Journal of Engineering Research and Applications, 2014, 4:182-187.

[22] Gultom LA., Dirhamsyah and Dina S. Physical Properties Of Rice Straw Particle Board. Jurnal Hutan Lestari, 2013, 1:458-465.

[23] Abd El-baky MA. Evaluation of Mechanical Properties of Jute/Glass/Carbon Fibers Reinforced Hybrid Composites. Fibers and Polymers, 2017, Vol.18, No.12: 2417-2432.

[24] Pakravan HP., Jamshidi M., Asgharian Jeddi AA. Combination of ground rice husk and polyvinyl

alcohol fiber in cementitious composite. Journal of Environmental Management, 2018, 215: 116-122.

[25] Jawad K. Oleiwi, Qahtan Adnan Hamad and Hadil Jabbar Abdul Rahman. Experimental Investigation of Flexural and Impact Properties of PMMA Reinforced by Bamboo and Rice Husk Powders. International Journal of Mechanical Engineering and Techanology, 2018, 9(10):559–568.

[26] Farooq Sk, Vinay Kumar D., Optimization of Performance and Exhaust Emissions of a PFI SI Engine Operated with Iso-stoichiometric GEM Blends Using Response Surface Methodology. Jordan Journal of Mechanical and Industrial Engineering, 2021, Vol.15 (2):199-207.

[27] Shukry H., Aghdeab, Laith A., Mohammed , Alaa M. Ubaid, Optimization of CNC Turning for Aluminum Alloy Using Simulated Annealing Method. Jordan Journal of Mechanical and Industrial Engineering, 2015, Vol. 9 (1):39-44.

[28] Ghalme S., Koinkar P., Bhalerao Y. Effect of Aluminium Oxide (Al_2O_3) Nanoparticles Addition into Lubricating Oil on Tribological Performance. Tribology in Industry, 2020, Vol. 42 (3):494-502.

[29] Aslantasa K., Ekicib E., Cicek A. Optimization of process parameters for micro milling of Ti-6Al-4V alloy using Taguchi-based gray relational analysis. Measurement, 2018.

[30] Zulfiqar Ali Raza, Naseer Ahmad, Shahid Kamal. Multi-response optimization of rhamnolipid production using grey rational analysis in Taguchi method. Biotechnology Reports, 2014, 3:86–94.

[31] Prakash Kumar Sahu, Sukhomay Pal. Multi-response optimization of process parameters in friction stir welded AM20 magnesium alloy by Taguchi grey relational analysis. Journal of Magnesium and Alloys, 2015, 3:36-46.

[32] Ghalme S., Bhalerao Y., Phapale K. Analysis of Factors Affecting Delamination in Drilling GFRP Composite. Journal of Computational and Applied Research in Mechanical Engineering, 2021, Vol.10 (2): 281-289.

[33] Saadat Ali Rizvi, , Tewari S., Optimization of Welding Parameters by Using Taguchi Method and Study of Fracture Mode Characterization of SS304H Welded by GMA Welding. Jordan Journal of Mechanical and Industrial Engineering, 2018, Vol. 12 (1):17-22.

JJMIE

Volume 15, Number 5, December. 2021
ISSN 1995-6665
Pages 419 – 429

Jordan Journal of Mechanical and Industrial Engineering

Analytical Formula of Positive Position Solution of 2PPa-PSS 3-Translational Parallel Mechanism with Low Coupling-degree and its Numerical Application

Junjie Gong[a], Wei Wei[a,b,c*], Sixu Peng[a], Kechen Zhang[a]

[a]*School of Mechanical Engineering, Guangxi University, Nanning 530004, China*

[b]*School of Mechanical and Automotive Engineering,South China University of Technology, Guangzhou, China*

[c]*School of Mechanical Engineering,Guilin University of Aerospace Technology, Guilin, China*

Received January 7 2021 *Accepted October 18 2021*

Abstract

Most of the parallel mechanisms (PM) with low coupling degree cannot directly obtain the analytical expression of the positive position solution of the PM, which makes it difficult to carry out the follow-up research on the kinematic accuracy analysis and trajectory planning of the PM. Based on the topological structure theory, this paper analyzes the position and orientation characteristic(POC), DOF and coupling degree of 2PPa-PSS PM. Afterward, the kinematic mathematical model of 2PPa-PSS PM is established based on the order single open chain of kinematic modeling principle. The moving platform of the mechanism is set as an equilateral triangle, and the intermediate variables are solved by combining the constraints of the two chains. The positive position solution of the PM in analytical form is obtained. The correctness of the kinematic model of the mechanism is verified by numerical calculation. Then, according to the positive position solution analytical expression, we can work out the complete workspace of the PM, and the significant influence of the driving increment on the attitude change of the moving platform is analyzed by using the analysis method based on the orthogonal test. According to the results of orthogonal experiment, the best driving range of the mechanism is obtained.

Keywords: Positive position solution; Parallel mechanism; Coupling degree; Workspace; Orthogonal test;

1. Introduction

Motion analysis is the basic task of parallel mechanism, and position analysis is the basis of velocity analysis, acceleration analysis and other follow-up research [1]. Due to the mutual constraints between the branches and chains, the structure of the low-degree-of-freedom parallel mechanism is complex, and the positive position solution of the parallel mechanism in analytical form is difficult to be obtained. The application research of parallel mechanism [2-3] is limited to the analytical expression of inverse position solution, and it is difficult to carry out the follow-up research on the influence of its complete workspace, drive on the attitude change of moving platform and dynamic forward solution.

At present, for parallel mechanisms with non-zero coupling degree, there is not generally positive position solution analytical form. Only with special topological structure can we obtain the analytic expression of positive position solution. This kind of mechanism can be applied to space precise positioning [4-6] or attitude adjustment equipment [7-10], which has high research value [11-14]. Ma et al. [15] analyzed the kinematics and workspace of a 2-PrRS-PR(P)S parallel mechanism by using the closed-loop equation. Arian et al. [16] analyzed the kinematics and dynamics of a three degree of freedom gantry tau robot. Cuan-Urquizo et al. [17] obtained a closed solution of the positive and inverse position solution of the 3-CUP parallel mechanism. Zeng et al. [18-19] analyzed the positive and inverse position solution, Jacobian matrix and stiffness performance of the three-translation parallel manipulator. Liu et al. [20] introduced a new 6-DOF orthogonal parallel mechanism, and its dynamic model was established to analyze the kinematic characteristics. Yan et al. [21] proposeda systematically approach for structure synthesis of parallel manipulator is based on position and orientation characteristic (POC) matrix, by which a detailed application is focused on the synthesis of 2-translation and 2-rotation parallel mechanisms. Zeng et al. [22-24] have done a lot of research on decoupling of parallel mechanism. For example, Zeng et al. [22] synthesized the rotary decoupled parallel mechanism based on the screw theory, proposed the selection principle of the input pair of the rotary driving limb, and formed the type synthesis method of the rotary decoupled parallel mechanism. Secondly, Zeng et al. [23] also proposed a decoupled 2T1R parallel mechanism, deduced the analytical solution expressions of the forward and inverse positions of the mechanism, and verified the decoupling characteristics of the mechanism; In addition, Zeng et al. [24] makes a systematic comparative analysis of 3-RPUR

* Corresponding author e-mail: 491651601@qq.com.

and 3-CPR parallel mechanisms. The results show that the coupling of parallel mechanisms has mutual effects on the workspace, dexterity, speed, payload capacity and stiffness of the mechanism.

However, there are the following problems in the study of parallel mechanism. When the coupling degree of mechanism is not zero, the positive position solution of mechanism can't be obtained directly [25]. Therefore, most of the workspace of parallel mechanism can only be solved based on the inverse position solution. However, it is difficult to obtain a complete workspace by using the analytical formula of the inverse position solution [1]. ② The input-output motion decoupling characteristics of parallel mechanism can only be qualitatively analyzed, but not quantitative analysis of the influence of each driving on the moving platform makes the motion control and trajectory planning more complex [26-27].

Based on the topological structure theory of parallel mechanism, this paper analyzes the position and orientation characteristic, DOF and coupling degree of a low coupling 2PPa-PSS 3-Translation parallel mechanism with special topological structure. The moving platform is set as an equilateral triangle, and the intermediate variables are solved by combining the constraint equations of Branch II and branch III. Based on the kinematic modeling principle of single open chain, the analytic expression positive position solution of the parallel mechanism is obtained. Based on the analytic expression of the positive position solution, the complete working space of the parallel mechanism is drawn. Afterward, the orthogonal test is designed to analyze the significant influence of the driving mechanism on the coordinate change of the moving platform, and the optimal driving range is obtained. Finally, according to the singular position of the mechanism, the index of testing the driving is obtained, which provides a reference for further optimization analysis and real-time control of the mechanism.

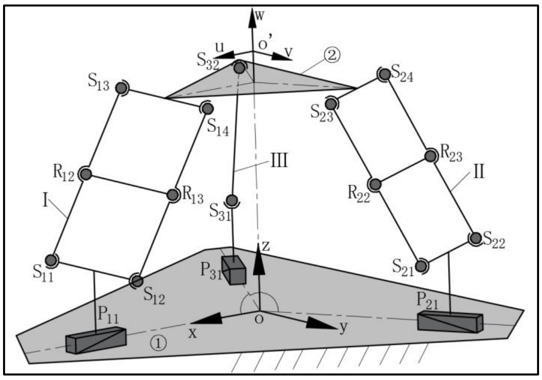

Figure 1. 2PPa-PSSParallel Mechanism

2. Description of mechanism structure

According to the topological structure theory and design method of parallel mechanism, this paper presents a three translation parallel mechanism driven by three moving pairs, as shown in Figure 1. The whole mechanism is composed of static platform ①, moving platform ② and three branches, in which Branch I and Branch are the same hybrid single open chain (*HSOC*), that is, The moving pair P and the moving platform 2 are respectively connected in the 4S parallelogram and arranged on the opposite side, which is recorded as follows $HSOC_i$: $P\left(SRS\right)_2$ (i = I, II).The connection relationship of the kinematic pairs of Branch I and Branch is identical. Branch III is a single-open-chain (*SOC*), that is, the prismatic pair P_{31}, spherical pair S_{31} and spherical pair S_{32} are connected in series connection, they are recorded as $SOC_{\text{III}}:PSS$.

The whole mechanism is triangular and asymmetrical, which has three characteristics: simple structure, easy to manufacture and easy to assemble.

3. Analysis the topological structure of mechanism

3.1. Analysis the POC set of mechanism

The structure of hybrid single open chain I and hybrid single open chain II of the parallel mechanism is identical, and its topological structure can be expressed as:

$C_i\left\{P_{i1}-\Diamond\left(4S-2R\right)\right\}\left(i=1,2\right)$

The topological structure of single open chain III is: $C_3\left\{P_{31}-S_{31}-S_{32}\right\}$. According to the topological structure theory and the *POC* equation of parallel mechanism,the *POC* set of mechanism is solved.

The *POC* equation of parallel mechanism is [25]

$$M_{bi}=\bigcup_{j=1}^{k}M_{sj} \tag{1}$$

$$M_{pa}=\bigcap_{i=1}^{n}M_{bi} \tag{2}$$

where: M_{pa} is the *POC* set of the mechanism moving platform; M_{bi} represent the *POC* set the *i*-th at the end of branch chain; M_{sj} denote the *POC* set of the *j*-th sub single open chain in the branch chain;

Branch I and Branch II have the same structure, and the end of them generate the *POC* set is identical. Owing to the motion output of parallelogram $\Diamond\left(4S-2R\right)$ is equivalent to 2T1R, according to formula (1), we can get

$$M_{bi}=\begin{bmatrix} t^1\left(\|P_{i1}\right) \\ r^0 \end{bmatrix}\bigcup\begin{bmatrix} t^2 \\ r^1\|\left(S_{i1}S_{i2}\right) \end{bmatrix}=\begin{bmatrix} t^3 \\ r^1\|\left(S_{i1}S_{i2}\right) \end{bmatrix}\left(i=1,2\right)$$

Since Branch III is an unconstrained branch, of which the end generates the *POC* set is

$$M_{b3}=\begin{bmatrix} t^3 \\ r^3 \end{bmatrix}$$

POC set of moving platform ② is

$$M_{pa}=M_{b1}\bigcap M_{b2}\bigcap M_{b3}$$

$$=\begin{bmatrix} t^3 \\ r^1\|\left(S_{11}S_{12}\right) \end{bmatrix}\bigcap\begin{bmatrix} t^3 \\ r^1\|\left(S_{21}S_{22}\right) \end{bmatrix}\bigcap\begin{bmatrix} t^3 \\ r^3 \end{bmatrix}=\begin{bmatrix} t^3 \\ r^0 \end{bmatrix}$$

The result reveal that the position and orientation characteristic of any point on the moving platform ② is three translation $\left(3T0R\right)$ which is the translation of three directions of the XYZ axis.

3.2. Calculation of degree of freedom and coupling degree of parallel mechanism

The formula of parallel mechanism is [25]

$$F=\sum_{i=1}^{m} f_i-\sum_{j=1}^{v}\xi_{Lj} \tag{3}$$

$$\xi_{Lj}=\dim.\left\{\left(\bigcap_{i=1}^{j} M_{bi}\right)\bigcup M_{b(j+1)}\right\} \tag{4}$$

where: F is the degree of freedom of the mechanism, f_i represents the degree of freedom of the i-th kinematic pair (excluding passive degree of freedom), m denotes the number of kinematic pairs of the mechanism, n is the number of mechanism components, $v=m-n+1$ represents the number of independent loops, ξ_{Lj} is the number of independent displacement equations of the j-th independent loop, $\bigcap_{i=1}^{j} M_{bi}$ denotes the *POC* set of the sub parallel mechanism composed of the first i branches, $M_{b(j+1)}$ is the set of the end components of the first $j+1$ branches.

The formula of the coupling degree κ of the mechanism is [25]

$$\begin{aligned}\kappa&=\frac{1}{2}\min.\left\{\sum_{j=1}^{v}\left|\Delta_j\right|\right\}\\&=\frac{1}{2}\min.\left\{\sum_{j=1}^{v}\left|\sum_{i=1}^{m_j} f_i-I_j-\xi_{Lj}\right|\right\}\end{aligned} \tag{5}$$

where: $\min.\{\square\}$ represents that the basic kinematic chain (BKC) is decomposed into v -th $SOC_j\left(\Delta_j\right)$, and there are many decomposition schemes, $\left(\sum\left|\Delta_j\right|\right)$ is the smallest.

The parallel mechanism can be divided into two independent circuits:

$SOC_1=\{-P_{11}\perp R_{11}\|\lozenge(4S-2P)\|R_{14}-R_{24}\|\lozenge(4S-2P)$
$\|R_{21}\perp P_{21}-\}$

$SOC_2=\{-P_{31}-S_{31}-S_{32}-\}$

According to equations (3) and (4), the number of independent displacement equations of the first independent loop is determined

$$\begin{aligned}\xi_{L1}&=\dim.\left\{M_{b1}\bigcup M_{b2}\right\}\\&=\dim.\left\{\begin{bmatrix}t^3\\ r^1(\|R_{11})\end{bmatrix}\bigcup\begin{bmatrix}t^3\\ r^1(\|R_{21})\end{bmatrix}\right\}=5\end{aligned}$$

$$F_{(1-2)}=\sum_{i=1}^{8} f_i-\xi_{L1}=8-5=3$$

$$M_{pa(1-2)}=M_{b1}\bigcap M_{b2}=\begin{bmatrix}t^3\\ r^0\end{bmatrix}$$

The number of independent displacement equations of the second independent loop is

$$\xi_{L2}=\dim.\left\{M_{pa(1-2)}\bigcup M_{b3}\right\}=\dim.\left\{\begin{bmatrix}t^3\\ r^3\end{bmatrix}\right\}=6$$

According to formula (3), the degree of freedom of the parallel mechanism can be obtained

$$F=\sum_{i=1}^{11} f_i-\sum_{j=1}^{2}\xi_{Lj}=(8+6)-(5+6)=3$$

The results reveal that when the three moving pairs P_{11}, P_{21} and P_{31} on the static platform ① are used as driving pairs, the parallel mechanism can achieve 3-D translational motion output.

The constraints degrees of two single open chains are as follows

$$\Delta_1=\sum_{i=1}^{8} f_i-I_1-\xi_{L1}=8-2-5=1$$

$$\Delta_2=\sum_{i=1}^{3} f_i-I_2-\xi_{L2}=6-1-6=-1$$

By substituting the results of the above two formulas into equation 5, we can get

$$\kappa=\frac{1}{2}\sum_{j=1}^{2}\left|\Delta_j\right|=\frac{1}{2}\left(1+|-1|\right)=1$$

The results indicate that the coupling degree of the parallel mechanism is $\kappa=1$. In most cases, it is difficult for the parallel mechanism whose coupling degree is not zero to get the analytical formula of the positive position solution of the parallel mechanism, and the parallel mechanism can get the analytical formula of the positive position solution by setting the intermediate variables.

4. Kinematic analysis of parallel mechanism

4.1. Coordinate system and parameter setting

The parallel mechanism is driven by three moving pairs P_{11}, P_{21} and P_{31}. Three driving pairs are distributed on the same platform ①, and their axis angle is 120 °. According to figure 1, the kinematic modeling of the parallel mechanism is established, as shown in Figure 2.

The static coordinate system $o-xyz$ is established on the static platform ①. The coordinate origin o is the center of gravity of the static platform, and the x-axis coincides with the P_{11} axis. The x-axis rotates 90 ° anticlockwise around the origin o to be the y-axis, which has an angle of 30 ° with the axis of P_{21} .The z-axis is determined by the Cartesian coordinate system of the right hand. The coordinate system $o'-xyz$ is set on the top of the moving platform ②, and the coordinate origin o' is located on the top of the center of gravity D point of the moving platform ②, $o'D=l_4$ .The u-axis coincides with P_{11} axis and points to C_1 . The u-axis rotates 90 ° anticlockwise around the origin o' to form the v-axis. The determination method of w-axis is the same as that of z-axis.

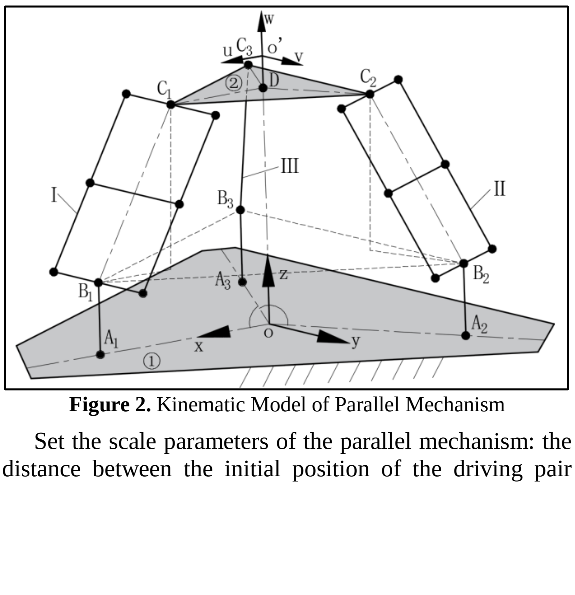

Figure 2. Kinematic Model of Parallel Mechanism

Set the scale parameters of the parallel mechanism: the distance between the initial position of the driving pair

P_{11}, P_{21} and P_{31} and the origin o are d_1, d_2 and d_3 respectively, that is, $oA_i = d_i$ (i=1, 2, 3, same below). The moving range of the driving pair is $[0, s_i]$. The length of each rod are $A_iB_i = l_1$, $B_iC_i = l_2$ and $C_iD = l_3$. The shape of moving platform is equilateral triangle, whose side length is $\sqrt{3}l_3$, and the size of each angle is $\angle A_ioA_j = \angle C_iDC_j = 120^\circ$. On account of $A_iB_i = l_1$, B_1, B_2 and B_3 are in the same plane and parallel to the xoy plane. Set the intermediate variable angle between B_iC_i and plane $B_1B_2B_3$ is α^*. The projection of B_iC_i on $B_1B_2B_3$ is B_iC_i'. The intermediate variable angle between B_iC_i' and oA_1 is β^*, where $i = 1,2,3$, $j = 1,2,3$, $i \neq j$, the schematic diagram of the angle position of the intermediate variable is shown in Figure 3.

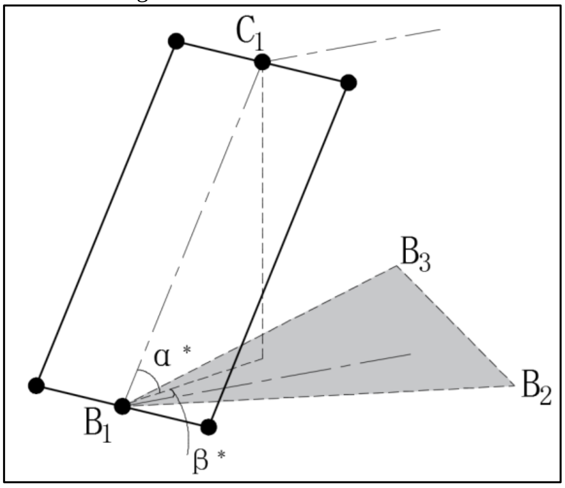

Figure 3. Schematic diagram of intermediate variable angle

4.2. Analysis of positive position solution of parallel mechanism

It is known that the motion range of the driving pair P_{11}, P_{21} and P_{31} are $[0, s_i]$ and the initial positions of them are d_1, d_2 and d_3 respectively. Next,we can use the condition to solve the coordinates (x, y, z) of o' on the moving platform ②.

According to the static coordinate system established by the kinematic model of the mechanism, the coordinates of each point can be obtained as follows:

$A_1(d_1 + s_1, 0, 0)$, $B_1(d_1 + s_1, 0, l_1)$

$A_2\left(-(d_2 + s_2)/2, \sqrt{3}(d_2 + s_2)/2, 0\right)$

$B_2\left(-(d_2 + s_2)/2, \sqrt{3}(d_2 + s_2)/2, l_1\right)$

$A_3\left(-(d_3 + s_3)/2, -\sqrt{3}(d_3 + s_3)/2, 0\right)$

$B_3\left(-(d_3 + s_3)/2, -\sqrt{3}(d_3 + s_3)/2, l_1\right)$

(1) On the *SOC* of $\Delta_1 = 1$, using the intermediate variables angle α^* and angle β^*, the coordinate of C_1 and C_2 relative to the static coordinate system *o-xyz* can be obtained by geometric method, that is

$$C_1^* = \begin{bmatrix} d_1 + s_1 - l_2\cos\alpha^*\cos\beta^* \\ l_2\cos\alpha^*\sin\beta^* \\ l_1 + l_2\sin\alpha^* \end{bmatrix}$$

$$C_2^* = \begin{bmatrix} d_1 + s_1 - l_2\cos\alpha^*\cos\beta^* - 3l_3/2 \\ l_2\cos\alpha^*\sin\beta^* + \sqrt{3}l_3/2 \\ l_1 + l_2\sin\alpha^* \end{bmatrix}$$

(2) According to the position matrix of the moving coordinate system *o-uvw* relative to the static coordinate system *o-xyz*, the position matrix of the moving coordinate system is

$$^{o}\boldsymbol{p}_{o'} = \begin{bmatrix} x & y & z \end{bmatrix}^T \tag{6}$$

According to formula(6), combining the coordinates of C_1 and C_2, we can get

$C_1^* = C_1 + {}^{o}\boldsymbol{p}_{o'}$

On the *SOC* with $\Delta_2 = -1$, the coordinates of C_1, C_2 and C_3 in the moving coordinate system *o-uvw* are

${}^{o'}C_1(l_3, 0, -l_4)$, ${}^{o'}C_2\left(-l_3/2, \sqrt{3}l_3/2, -l_4\right)$,

${}^{o'}C_3\left(-l_3/2, -\sqrt{3}l_3/2, -l_4\right)$

Coordinate of intermediate variable of point C_3^* is

$$C_3^* = \left(-\frac{l_3}{2} + x, -\frac{\sqrt{3}l_3}{2} + y, -l_4 + z\right)$$

By $B_2C_2 = B_3C_3 = l_2$, the constraint equation of parallel mechanism can be established:

$$\begin{cases} \left(x_{C_2}^* - x_{B_2}\right)^2 + \left(y_{C_2}^* - y_{B_2}\right)^2 + \left(z_{C_2}^* - z_{B_2}\right)^2 = l_2^2 \\ \left(x_{C_3}^* - x_{B_3}\right)^2 + \left(y_{C_3}^* - y_{B_3}\right)^2 + \left(z_{C_3}^* - z_{B_3}\right)^2 = l_2^2 \end{cases} \tag{7}$$

In this paper, we cleverly designed the moving platform of the parallel mechanism as an equilateral triangle, that is,

$$C_1C_2 = \sqrt{3}C_1D = \sqrt{3}l_3 \tag{8}$$

Because the equivalent relationship of the side length of the moving platform is known, the intermediate variables angle α^* and β^* can be solved by combining the link length constraint equation (7) of branch chain II and branch chain III..This is the key to solving the analytic expression of the positive position solution.

The coordinates of B_2 and C_2 are substituted into equation(7), which is sorted out and simplified, we can get

$$\begin{cases} A\cos\alpha^*\sin\beta^* + B\cos\alpha^*\cos\beta^* + C = 0 \\ D\cos\alpha^*\sin\beta^* + E\cos\alpha^*\cos\beta^* + F = 0 \end{cases}$$

where

$A = \sqrt{3}l_2(l_3 - d_2 - s_2)$

$B = -2l_2\left[d_1 + s_1 + (d_2 + s_2 - 3l_3)/2\right]$

$C = \left[d_1 + s_1 + (d_2 + s_2 - 3l_3)/2\right]^2 + 3(l_3 - d_2 - s_2)^2/4$

$D = \sqrt{3}l_2(d_3 + s_3 - l_3)$

$E = -2l_2\left(d_1 + s_1 + (d_3 + s_3 - 3l_3)/2\right)$

$F = \left[d_1 + s_1 + (d_3 + s_3 - 3l_3)/2\right]^2 + 3(d_2 + s_2 - l_3)^2/4$

By solving equation (7), we can get

$$\begin{cases} \beta^* = \arctan\dfrac{-BF-CE}{AF+CD} \\ \alpha^* = \arccos\dfrac{-C}{A\sin\beta + B\cos\beta} \end{cases}$$

Due to $C_iD = l_3$, substituting angle α^* and angle β^* into the coordinates of C_2^*, we can get the analytical formula (9) of the positive position solution of the o' point on the moving platform

$$\begin{cases} x = d_1 + s_1 - l_2\cos\alpha^*\cos\beta^* - l_3 \\ y = l_2\cos\alpha^*\sin\beta^* \\ z = l_1 + l_2\sin\alpha^* + l_4 \end{cases} \tag{9}$$

4.3. Analysis of inverse solution position of parallel mechanism

Given the coordinates (x, y, z) of o' point in the moving coordinate system of moving platform ②, the distance $s_i(i=1,2,3)$ required to move the driving pair is calculated.

First, the absolute coordinates of point C_1, C_2 and C_3 are obtained:

$$C_1(x+l_3, y, z-l_4) \quad C_2\left(x-\frac{l_3}{2}, y+\frac{\sqrt{3}l_3}{2}, z-l_4\right)$$

$$C_3\left(x-\frac{l_3}{2}, y-\frac{\sqrt{3}l_3}{2}, z-l_4\right)$$

Owing to $B_iC_i = l_2(i=1,2,3)$, we can establish constraint equation as follows:

$$\begin{cases} \left(x_{C_1}-x_{B_1}\right)^2+\left(y_{C_1}-y_{B_1}\right)^2+\left(z_{C_1}-z_{B_1}\right)^2 = l_2^2 \\ \left(x_{C_2}-x_{B_2}\right)^2+\left(y_{C_2}-y_{B_2}\right)^2+\left(z_{C_2}-z_{B_2}\right)^2 = l_2^2 \\ \left(x_{C_3}-x_{B_3}\right)^2+\left(y_{C_3}-y_{B_3}\right)^2+\left(z_{C_3}-z_{B_3}\right)^2 = l_2^2 \end{cases} \tag{10}$$

Substituting the coordinates of point B_i and C_i into equation (10)

$$\begin{cases} s_1 = x + l_3 - d_1 \mp \sqrt{l_2^2 - y^2 - (z-l_4-l_1)^2} \\ s_2 = \dfrac{-E_1 \pm \sqrt{E_1^2 - 4F_1}}{2} - d_2 \\ s_3 = \dfrac{-E_2 \pm \sqrt{E_2^2 - 4F_2}}{2} - d_3 \end{cases}$$

where

$$E_1 = x - \sqrt{3}y - 2l_3$$

$$E_2 = x - \sqrt{3}y + l_3$$

$$F_1 = (x-l_3/2)^2 + \left(y+\sqrt{3}l_3/2\right)^2 + (z-l_4-l_1)^2 - l_2^2$$

$$F_2 = (x-l_3/2)^2 + \left(y-\sqrt{3}l_3/2\right)^2 + (z-l_4-l_1)^2 - l_2^2$$

The results show that there are 8 groups of inverse solutions and 8 configurations of the mechanism.

4.4. Verification of positive and inverse analytical expressions of position for mechanism.

Set the scale parameters of the paralle mechanism as follows l_1= 50mm, l_2= 400mm, l_3= 60mm, l_4= 60mm, d_1= d_2= d_3= 60mm.

Table 1. Positive solution value of mechanism position I

Coordinate	x/mm	y/mm	z/mm
Value	71.6565	17.3731	448.2069

Table 2. Inverse solution of mechanism position I

Serial number	s_1/mm	s_2/mm	s_3/mm
1	274.5280	170.7403	145.9299
2	274.5280	170.7403	-267.6775
3	274.5280	-232.3057	145.9299
4	274.5280	-232.3057	-267.6775
5	-151.2150	170.7403	145.9299
6	-151.2150	170.7403	-267.6775
7	-151.2150	-232.3057	145.9299
8	-151.2150	-232.3057	-267.6775

Set the moving range of the three driving pairs to be the same, all of which are $s_i \in [0,350](i=1,2,3)$. The scale parameters of the mechanism are substituted into the positive position solution(9). Take two sets of data respectively. Setting the first group data of driving pair are s_1 = 274.2579mm, s_2 = 170.7403mm, s_3 = 145.9299mm respectively. Setting the second group data of coordinates of the moving platform is (71.6565, 17.3731, 448.2069). Take two groups of data respectively and use Matlab programming to calculate the positive solution of mechanism position, as shown in Table 1 and Table 2.

Take the data in Table 1 and substitute it into equation (10) to calculate the inverse position solution data of the mechanism, as shown in Table 2.

The results show that the positive and inverse solutions obtained by Matlab software are completely matched, which shows that the analytical formula of the positive and inverse position solutions of the parallel mechanism is correct.

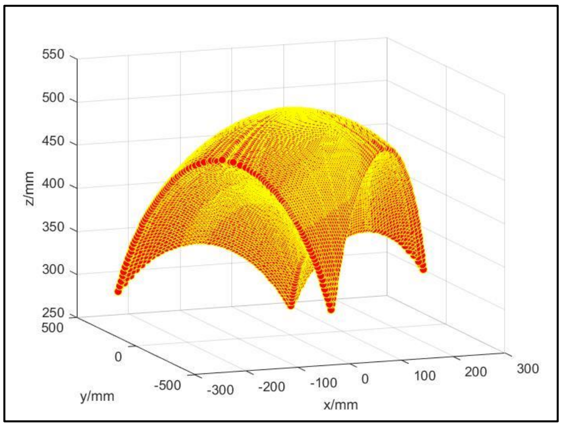

Figure 4. 3D figure of workplace for the mechanism

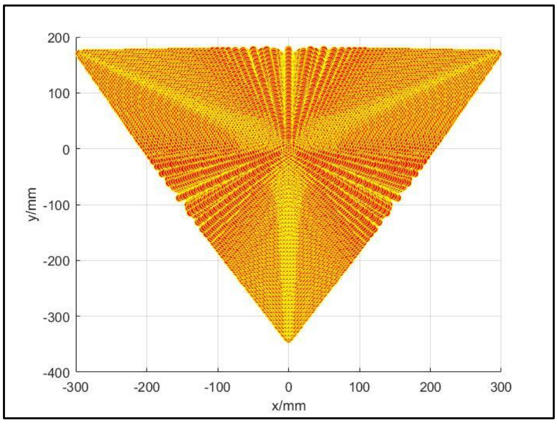

(a) xy-Direction view of workplace for the mechanism

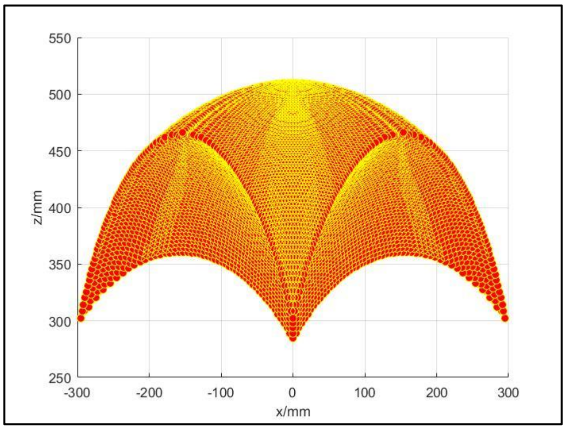

(b)xz-Direction view of workplace for the mechanism

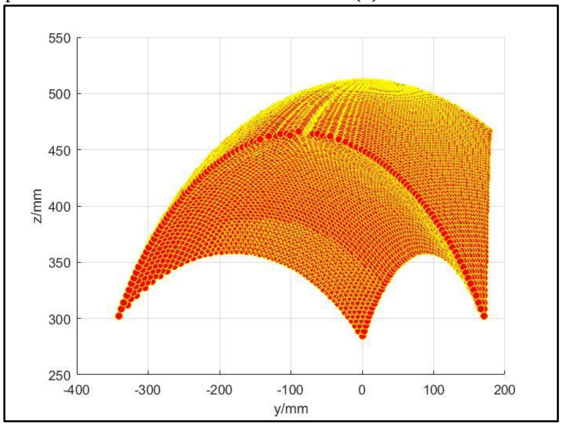

(c)yz-Direction view of workplace for the mechanism

Figure 5. Three views of mechanism motion space

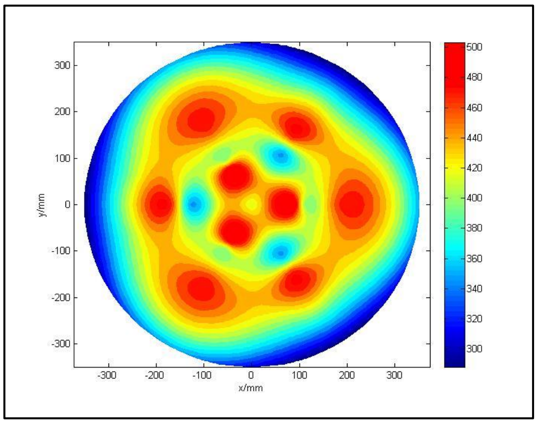

Figure 6. Cloud figure of workplace for the mechanism

5. Analysis of parallel mechanism motion performance

5.1. Workspace analysis

The motion range of driving pair P_{11} P_{12} and P_{13} is set as [0, 350mm], their initial position are $d_1=d_2=d_3=60$mm, and their step length are all 7mm. According to the positive analytical formula of mechanism (9), the stereogram and cloud diagram of working space of mechanism are obtained by Matlab software programming, as shown in Fig. 4, Fig. 5 and Fig. 6.

Analysis of Fig. 4, Fig. 5 and Fig.6 shows that:

1) The workspace of the parallel mechanism is symmetrically distributed, continuous and free of cavities, with good performance. When all three driving pairs are at the starting point, the mechanism reaches the workspace boundary.

2) Within the set range of the working stroke of the mechanism driving pair, the working space does not contain singular points, the effective working space is large and the range is centralized, which has a good use value.

5.2. Singularity analysis of parallel mechanism

5.2.1. Singularity principle of parallel mechanism

By analyzing whether the determinant of Jacobian matrix is zero, we can judge whether the mechanism is singular. The singular configuration of parallel mechanism can be divided into three categories: (1) the input singularity will occur when the $|J_q|=0$ and $|J_p|\neq 0$; (2) the output singularity will occur when the $|J_p|=0$ and $|J_q|\neq 0$; (3) the comprehensive singularity will occur when the $|J_q|=0$ and $|J_p|=0$ .The drive range of the parallel mechanism should be avoided near the singular location.

Both sides of the constraint equation (10) of the link length of the mechanism derive the time at the same time, and the relationship between the output speed $v=[\dot{x} \quad \dot{y} \quad \dot{z}]^T$ of the end platform of the mechanism and the input speed $\dot{x}=[\dot{s}_1 \quad \dot{s}_2 \quad \dot{s}_3]^T$ of the driving pair is obtained as follows

$$J_p v = J_q \dot{x} \tag{11}$$

where

$$J_p=\begin{bmatrix} v_{11} & v_{12} & v_{13} \\ v_{21} & v_{22} & v_{23} \\ v_{31} & v_{32} & v_{33} \end{bmatrix} \tag{12}$$

$$J_q = diag(u_{11}, u_{22}, u_{33}) \tag{13}$$

$$v_{11}=x_{B_1}-x_{C_1}, \quad v_{12}=y_{B_1}-y_{C_1}, \quad v_{13}=z_{B_1}-z_{C_1},$$
$$v_{21}=x_{B_2}-x_{C_2}, \quad v_{22}=y_{B_2}-y_{C_2}, \quad v_{23}=z_{B_2}-z_{C_2},$$
$$v_{31}=x_{B_3}-x_{C_3}, \quad v_{32}=y_{B_3}-y_{C_3}, \quad v_{33}=z_{B_3}-z_{C_3},$$
$$u_{11}=(x_{B_1}-x_{C_1})s_1,$$
$$u_{22}=s_2(x_{C_2}-x_{B_2})/2+\sqrt{3}s_2(y_{C_2}-y_{B_2})/2$$
$$u_{33}=s_3(x_{C_3}-x_{B_3})/2-\sqrt{3}s_3(y_{C_3}-y_{B_3})/2$$

5.2.2. Input singularity

If any element of the diagonal of equation (12) is zero, the input singularity of the mechanism will occur when $|J_q|=0$ and $|J_p|\neq 0$.

Owing to u_1=0 , u_2=0 , u_3=0 , we can obtain

$$\left.\begin{array}{l} x_{B_1}=x_{C_1} \\ x_{C_2}=x_{B_2}, y_{C_2}=y_{B_2} \\ x_{C_3}=x_{B_3}, y_{C_3}=y_{B_3} \end{array}\right\} \tag{14}$$

When the coordinate of the $B_i(i=1,2,3)$ and $C_i(i=1,2,3)$ satisfies any equation in the formula (14), then $|J_q|=0$. In other words, A_i, B_i and $C_i(i=1,2,3)$ are collinear, the input singularity occurs.It indicates that the moving platform of the paralle mechanism reaches the boundary of the workspace.

5.2.3. Output singularity

The output singularity of the parallel mechanism will occur when $|J_p|=0$ and $|J_q|\neq 0$. In other words, the driving pair can't drive the moving platform even if the force on the moving platform is very small. If we regard the corresponding row of formula (12) as a vector, we can get

$$J_p=[V_1 \quad V_2 \quad V_3]^T$$

1. When any two vectors are linearly related, $|J_p|$ equals zero.

Setting $V_1=\eta V_2$ (where η is a coefficient), B_1C_1 and B_2C_2 are parallel in space, that is $[v_{11} \quad v_{12} \quad v_{13}]=\eta[v_{21} \quad v_{22} \quad v_{23}]$.

2. When the three vectors are linearly correlated, $|J_p|$ equals zero.

Setting $V_1=\eta_1 V_2+\eta_2 V_3$ (where η_1 and η_2 are coefficient), B_1C_1, B_2C_2 and B_3C_3 are parallel in space, that is $[v_{11} \quad v_{12} \quad v_{13}]=\eta_1[v_{21} \quad v_{22} \quad v_{23}]=\eta_2[v_{31} \quad v_{32} \quad v_{33}]$.

5.3. Comprehensive singularity

The mechanism will have synthetic singularity when $|J_q|=0$ and $|J_p|=0$, that is, input singularity and output singularity occur at the same time, and the mechanism satisfies A_i, B_i and C_i three-point collinear and B_iC_i // B_jC_j (i=1, 2, 3, j=1, 2, 3 and $i \neq j$).

6. Driving significance analysis

6.1. Orthogonal test scheme design and range analysis

It can be seen from equation (9) that the drive of the mechanism leads to the nonlinear change of the coordinates of the moving platform. Therefore, in the whole driving range, the driving change has little influence on the coordinate increment of the moving platform. In other words, we look for the driving range with the largest reduction of displacement, which is convenient for the real-time control of the parallel mechanism. Therefore, the optimal driving range of the parallel mechanism is solved by designing the orthogonal experiment. Taking the coordinate difference of the moving platform of the parallel mechanism as the research object, the significant influence of the driving pair on the coordinate change of the moving platform is explored. The target parameters of the test object are the changes of the coordinates of the moving platform Δx, Δy and Δz .The structural parameters expressing the coordinate change of the moving platform are the increments of s_1, s_2 and s_3, the increment equal s = 70mm.

The starting points of the five increments of the three drivers are 0, 70mm, 140mm, 210mm, 280mm, respectively. It is assumed that there is no interaction between the three driving displacements in the control process [28].

The orthogonal Table $L_p(t^q)$ is used to arrange the experiment, where L is the code of the orthogonal table, p is the number of experiments, t is the horizontal number, and q is the number of influencing factors. In this paper, the orthogonal table q=3, is selected as shown in Table 3.

Table 3. Values of s_1, s_2 and s_3 at different levels in orthogonal tests

Level	s_1/mm	s_2/mm	s_3/mm
1	0	0	0
2	70	70	70
3	140	140	140
4	210	210	210
5	280	280	280

The results of orthogonal test were analyzed, as shown in Table 4. Calculate the numerical value and range of the three factors under the five levels, and test whether the *j*th column factor has significant influence on the test result statistic F_j .Under the given significance level α , if $F_j \geq F_{1-\alpha}\left(f_j, f_e\right)$ is satisfied, it can be considered that the factors arranged in this column have a significant influence on the coordinate change of the moving platform of the mechanism, otherwise, the influence is not significant.

Table 4. Range analysis

Test	The influence of driving on x				The influence of driving on y				The influence of driving on z			
	s_1	s_2	s_3	Error term	s_1	s_2	s_3	Error term	s_1	s_2	s_3	Error term
K_{1j}	94.93	-47.47	-56.74	4.27	0.00	82.21	-98.28	-8.52	-116.18	-116.18	-112.66	-199.34
K_{2j}	-28.79	-43.61	-2.30	-37.92	-13.16	-20.43	-3.99	5.15	-156.12	-132.29	-162.51	-182.71
K_{3j}	-41.66	19.09	8.36	-56.75	-2.02	-37.09	14.47	6.87	-180.44	-180.44	-189.85	-173.60
K_{4j}	-79.32	15.02	13.53	-3.02	9.54	-29.10	23.43	0.70	-184.91	-208.73	-215.91	-166.16
K_{5j}	-11.35	-9.23	-29.24	27.22	-17.21	-18.44	41.51	-27.02	-253.73	-253.73	-210.43	-169.57
R_j	174.26	66.55	70.27	83.97	26.75	119.30	139.78	33.92	137.55	137.55	103.24	33.18

6.2. Significance analysis

According to the orthogonal test scheme and range analysis method, the orthogonal influence factors are used for numerical calculation to obtain 25 sets of orthogonal combination values as shown in Table 5.

Table 5. Numerical results of orthogonal test combination

Level	1	2	3	*Δx*/mm	*Δy*/mm	*Δz*/mm
1	1	1	1	0.00	0.00	-7.96
2	1	2	1	11.06	0.00	-15.67
3	1	3	3	21.24	0.00	-22.33
4	1	4	4	28.58	0.00	-29.57
5	1	5	5	34.04	0.00	-40.66
6	2	1	2	-5.53	9.58	-15.67
7	2	2	3	-0.76	-1.32	-26.10
8	2	3	4	3.55	-2.64	-36.95
9	2	4	5	8.10	-2.89	-50.81
10	2	5	1	-34.14	-15.89	-26.59
11	3	1	3	-10.62	18.39	-22.33
12	3	2	4	-4.06	1.75	-36.95
13	3	3	5	-1.00	-1.73	-51.33
14	3	4	1	-19.04	-18.93	-25.76
15	3	5	2	-6.95	-1.50	-44.07
16	4	1	4	-14.29	24.75	-29.57
17	4	2	5	-53.16	16.65	-26.98
18	4	3	1	-6.87	-25.95	-25.76
19	4	4	2	-3.06	-5.30	-43.04
20	4	5	3	-1.94	-0.61	-59.55
21	5	1	5	-17.02	29.48	-40.66
22	5	2	1	3.31	-37.51	-26.59
23	5	3	2	2.17	-6.77	-44.07
24	5	4	3	0.44	-1.99	-59.55
25	5	5	4	-0.25	-0.43	-82.86

The data were processed according to the method of variance analysis.The statistic used to test whether the driving increment of the j-th column has a significant effect on the dynamic platform increment is F_j . According to the F distribution Table, we can get $F_{0.90}\left(4,8\right)$ =2.81, $F_{0.95}\left(4,8\right)=3.84$ and $F_{0.99}\cdot\left(4,8\right)$ =7.01. The statistics of the increment Δx of the x-coordinate of the moving platform corresponding to the three driving increments are, $F_{\Delta x\Delta s_1}=6.58$, $F_{\Delta x\Delta s_2}$ =1.52 and $F_{\Delta x\Delta s_3}=1.32$ respectively. Under the significance level of $\alpha=0.05$, the increase of s_1 has a significant effect on the change of moving platform coordinate Δx , while s_2 and s_3 have no significant effect on the change of moving platform coordinate Δx .

The statistics of the increment Δy of the y-coordinate of the moving platform corresponding to the three driving increments are $F_{\Delta y\Delta s_1}=1.04$, $F_{\Delta y\Delta s_2}=$ 21.78, $F_{\Delta y\Delta s_3}$ $=27.24$ respectively. Under the signific-ance level of $\alpha=0.01$, the increase of s_1 has no significant effect on the change of moving platform coordinate Δy , while s_2 and s_3 have significant influence on the change of moving platform y-coordinate, and the order of significant influence is as follows *s3*, *s2*.

The statistics of the increment Δz of the z-coordinate of the moving platform corresponding to the three driving increments are, $F_{\Delta y\Delta s1}$= 1.04, $F_{\Delta y\Delta s2}$=21.78, $F_{\Delta y\Delta s3}$=27.24, respectively. Under the significance level of $\alpha=0.01$, the three drives have significant effects on the changes of the moving platform, and the order of significant influence ares*2*, *s1*,and *s3*.

6.3. Analysis of the change characteristics of target parameters

In order to more intuitively analyze the influence of each factor level on the coordinate increment of the moving platform, we can comprehensively analyze the results according to the orthogonal test theory [19]. Sum the results of calculation at the level of each driving increment, and then calculate the average value. We can draw a graph of the influence of the driving on the coordinates of the moving platform, as shown in Figure 7.

As can be seen from fig. 7 (a), with the increase of s_1, the influence on the x-coordinate Δx of the moving platform decreases at first and then increases, and its variation range is (-15.9mm,19.0mm).. With the increase of s_2 and s_3 , their influences on the x-coordinate Δx of the moving platform increase at first and then decrease, and their variation ranges are smaller, which are (-

9.5mm,3.8mm) and (-11.3mm,2.7mm) respectively. Therefore, it is easier to control the change of the x-coordinate of the moving platform by selecting the drive s_1.

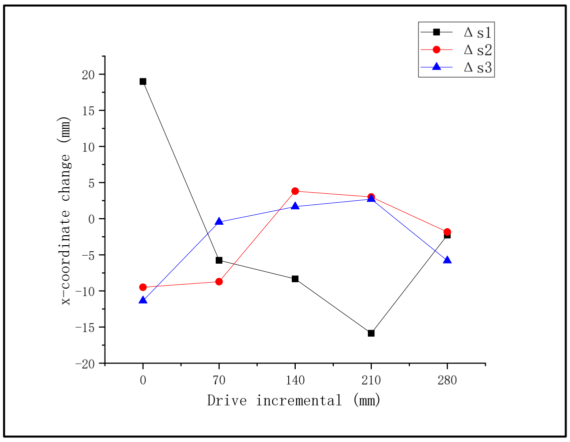

(a) x-coordinate change

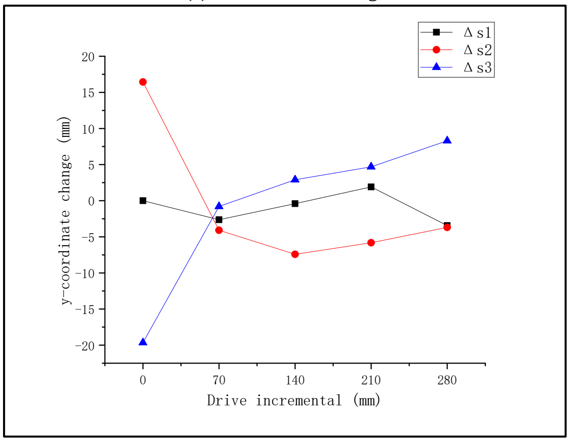

(b)y-coordinate change

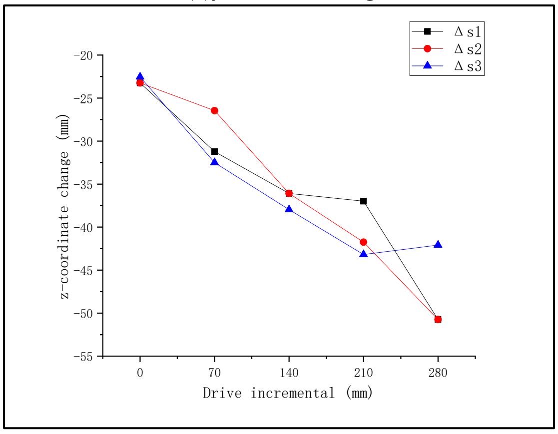

(c)z-coordinate change

Figure 7. Coordinate increment of moving platform changes with driving increment.

As can be seen from fig. 7 (b), with the increase of s_1, the influence on the y-coordinate Δy of the moving platform fluctuates in a very small range, and its variation range is (-3.4mm, 1.9mm) . With the increase of s_2, the influence on the y-coordinate Δy of the moving platform decreases at first, and then tends to smooth, and its variation range is (-3.7mm, 1.9mm). With the increase of s_3, the influence on the y-coordinate Δy of the moving platform increases at first and then tends to smooth, and its variation range is (-7.42mm, 16.44mm). Therefore, driving s_2 and s_3 can control the y-coordinate of the moving platform more easily.

As can be seen from fig. 7(c), with the increase of s_1, s_2 and s_3, the z-coordinate Δz of the moving platform all show a downward trend, and their changing ranges are (-50.75mm, -23.24m), (-50.75mm, -23.24mm) and (-43.18mm, -22.53mm), respectively. Therefore, driving s_1, s_2 and s_3 can effectively control the z-coordinates of the moving platform.

According to the comprehensive balance principle, the optimal driving range of the parallel mechanism is (70mm, 350mm). The influence of the driving increment on the coordinate increment of the moving platform can provide a reference basis for the real-time control and further optimization analysis of the parallel mechanism.

7. Experimental results and analysis

The physical prototype model is made according to the mechanism parameters of simulation analysis, as shown in Figure 8. The theoretical basis of significance analysis is the analytical formula of forward kinematics solution. Therefore, it is necessary to verify the correctness of equation (9) through experiments. It can be seen from Figure 7 that the driving increment has the greatest impact on the displacement of z-axis of the moving platform. Therefore, the z-axis displacement of the moving platform is selected for experimental verification.

Figure 8. Physical prototype model of 2PPa-PSS PM

Firstly, the moving pairs P_1, P_2 and P_3 are set at the initial position, and then the displacement in the Z direction of the end platform is measured by the laser rangefinder, to verify the correctness of the analytical formula of the forward kinematics solution. In addition, the accuracy of the laser rangefinder is 1mm. The experimental results are compared with the theoretical analysis, as shown in Figure 9.

According to Fig. 7(c), the three moving pairs have the same influence on the displacement of the moving platform in the Z direction, which is also proved by the experimental test results. According to figure 9, within the driving range of [0, 150mm], the coordinate changes in the Z direction of the moving platform are basically the same. The correctness of equation (9) is verified.

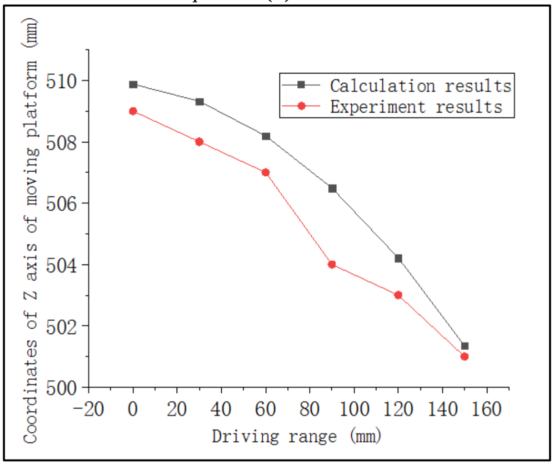

Figure 9. Z-axis displacement of 2PPa-PSS PM moving platform

8. Conclusions

The main conclusions are as follows:

1. The topological structure characteristics of a low coupling degree 3T PM are analyzed, and it is concluded that the degree of freedom is 3 and the coupling degree is 1. The kinematics model is established, and the analytical formula of positive and inverse position solution of the PM is solved based on the sequential single open chain method. The correctness of the analytical formula is verified by numerical calculation.

2. Based on the analytical formula of positive position solution, the complete discrete point workspace of the PM is obtained. The workspace of the PM is large and there is no cavity in the interior. Then, the singular configuration of the mechanism is analyzed based on the analytic expression of the inverse position solution.

3. The orthogonal test scheme is designed, and the coordinate change of the moving platform is numerically simulated. At different levels of the orthogonal experimental design, the three driving increments have significant effects on the coordinate changes of the moving platform. Finally, it is concluded that the optimal driving range of the parallel mechanism is 70mm - 350mm.

Declaration of conflicting interests

The author(s) declared no potential conflicts of interest with respect to the research, authorship, and /or publication of this article.

Funding

The author(s) disclosed receipt of the following financial support for the research, authorship, and/or publication of this article: The work was supported by the Guangxi Natural Science Foundation of China [2018GXNSFBA281080].

Reference

[1] Ranjan, J.; Damien, C.; Luc, B.; Fabrice, R.; Guillaume M.; "Workspace, joint space and singularities of a family of delta-like robot", Mechanism and Machine Theory,127, pp. 73-95, 2018. https://doi.org/10.1016/j.mechmachtheory.2018.05.004

[2] Zhao J.; Wu C, C.; Yang, G, L.; Chen C, Y.; Chen S, L.; Xiong C, Y.; Zhang C.; "Kinematics analysis and workspace optimization for a 4-DOF 3T1R parallel manipulator". Mechanism and Machine Theory, 167, 2022, 104484. https://doi.org/10.1016/j.mechmachtheory.2021.104484

[3] Xu LM.; Chen QH.; He LY.; Li QC.; "Kinematic analysis and design of a novel 3T1R 2-(PRR)2RH hybrid manipulator". Mechanism and Machine Theory, 112, pp. 105-122, 2017. https://doi.org/10.1016/j.mechmachtheory.2017.01.009

[4] Masoud, Z.; Nazzal, M.; Alhazza, K.; "Multimode input shaping control of flexible robotic manipulators using frequency-modulation". Jordan Journal of Mechanical and Industrial Engineering, 10(3), pp. 179-188, 2016. http://jjmie.hu.edu.jo/vol%2010-3/JJMIE-137-15-F-1.pdf

[5] Gong J, J.; Wei, W.; Cai G, W.; Liu Y, X.; Peng S, X.; "Kinematic Performance Analysis of a Controllable Mechanism Welding Robot with Joint Clearance". 2020 4th International Conference on Measurement Instrumentation and Electronics, Chengdu, People's Republic of China, 2020. https://doi.org/10.1051/matecconf/202032703006

[6] Mohammad, Al-K.; Omar, B.; Ibrahim Al-A.; "Exploration algorithm technique for multi-robot collaboration". Jordan Journal of Mechanical and Industrial Engineering, 5(2), pp. 177-184, 2011. http://jjmie.hu.edu.jo/files/v5n2/JJMIE-47-11%20Revised%20Adawan(10).pdf

[7] Gregorio, R. D.; "Kinematics of a new spherical manipulator with three equal legs: The 3-URC wrist".Robotic System, 18(5), pp.213-219, 2001. https://doi.org/10.1002/rob.1017

[8] Stock, M., Miller, K.; "Optimal Kinematic Design of Spatial Parallel Manipulators: Application to Linear Delta Robot". Journal of Mechanical Design,125(2), pp. 292-301,2003. https://doi.org/10.1115/1.1563632

[9] Luo, X.; Xie, F. G.; Liu, X. J.; "Kinematic calibration of the 3-degree-of-freedom redundantly actuated spatial parallel module of a five-axis hybrid machine". Proceedings of the Institution of Mechanical Engineers, Part B: Journal of Engineering Manufacture, 234(9), pp. 1185-1197, 2020. https://doi.org/10.1177/0954405420911299

[10] Zhang, F.X.; Chen, S. L.; He, Y. Y.; Ye, G. Y.; Zhang, C.; Yang, G, L.; "A Kinematic Calibration Method of a 3T1R 4-Degree-of-Freedom Symmetrical Parallel Manipulator". Symmetry, 12(3), pp. 1-16, 2020. https://doi.org/10.3390/sym12030357

[11] Deng, J. M.; Wang, W.; Shen, H. P.; Ma Z. H.; Li, Y. F.; Duan, S. L.; "Research on a Novel 3-DOF Planar Parallel Manipulator Driven by Three-Slider and its Larger Workspace Analysis".Applied Mechanics and Materials, 1503, pp. 590-593, 2012. https://doi.org/10.4028/www.scientific.net/AMM.130-134.590

[12] Li, Y. W.; Wang, J. S.; Liu, X. J.; Wang, L. P.; "Dynamic performance comparison and counterweight optimization of two 3-DOF parallel manipulators for a new hybrid machine tool". Mechanism and Machine Theory, 45(11), pp. 1668-1680, 2010. https://doi.org/10.1016/j.mechmachtheory.2010.06.009

[13] Latifah, N.; Stéphane C.; Philippe, Wenger.; Josef, S.; Manfred, H.; "Reconfiguration analysis of a 4-RUU parallel manipulator". Mechanism and Machine Theory, 96(2), pp. 269-289, 2016. https://doi.org/10.1016/j.mechmachtheory.2015.09.004

[14] Kelaiaia, R.; Company, O.; Zaatri, A.;"Multiobjective Optimazation of a Linear Delta Parallel Robot". Mechanism and Machine Theory, 50(2), pp. 159-178,2012. https://doi.org/10.1016/j.mechmachtheory.2011.11.004

[15] Ma, K.; Ma, H.; Tian, H.; "Kinematic analysis of a novel 2-PrRS-PR(P)S metamorphic parallel mechanism". Advances in Mechanical Engineering, 11(11), pp. 1-15, 2019. https://doi.org/10.1177/1687814019889776

[16] Arian, A.; Danaei, B.; Abdi, H.; Nahavandi, S.; "Kinematic and dynamic analysis of the Gantry-Tau, a 3-DOF translational parallel manipulator". Applied Mathematical Modelling, 51, pp. 217-231, 2017. https://doi.org/10.1016/j.apm.2017.06.012

[17] Cuan-Urquizo, E.; Rodriguez-Leal, E.;"Kinematic analysis of the 3-CUP parallel mechanism". Robotics and Computer-Integrated Manufacturing, 29(5), pp. 382-395, 2013. https://doi.org/10.1016/j.rcim.2013.03.002

[18] Zeng, Q.; Ehmann, K. F.; Cao, J.; "Tri-pyramid Robot: Design and kinematic analysis of a 3-DOF translational parallel manipulator", Robotics and Computer-Integrated Manufacturing, 30(6), pp. 648-657, 2014. https://doi.org/10.1016/j.rcim.2014.06.002

[19] Zeng, Q.; Ehmann, K. F.; Cao, J.; "Tri-pyramid Robot: stiffness modeling of a 3-DOF translational parallel manipulator". Robotica, 34(2), pp. 383-402, 2016. https://doi.org/10.1017/S0263574714001520

[20] Liu, X, L.; Wang, Q, Q.; Malikov, A.; Wang, H, R.; "The design and dynamic analysis of a novel 6-DOF parallel mechanism". International Journal of Machine Learning and Cybernetics, 3(1), pp. 27-37, 2012. https://doi.org/10.1007/s13042-011-0040-1

[21] Yan, Y.; Luo, YF.; Shi, ZX.; Yao, WK.; Yang, TL.; "Structure synthesis of two-translation and two-rotation parallel mechanisms based on the POC-based approach". 1st International Conference on Mechanical Engineering, Phuket, Thailand, 2011. https://doi.org/10.4028/www.scientific.net/AMM.52-54.759

[22] Zeng, D, X.; Huang, Z.; "Type synthesis of the rotational decoupled parallel mechanism based on screw theory".Science China-Technological Sciences, 54(4), pp. 998-1004, 2011. https://doi.org/10.1007/s11431-010-4239-2

[23] Zeng, D, X.; Jing, G, N .; Su, Y, L.; Wang, Y.; Hou, Y, L.; "A novel decoupled parallel mechanism with two translational and one rotational degree of freedom and its performance indices analysis". Advances in Mechanical Engineering, 8(5), pp. 1-10, 2016. http://doi.org/10.1177/1687814016646936

[24] Zeng, D, X.; Hou, Y, L.; Lu, W, J.; Huang, Z.; "Comparative Analysis of Characteristics of the Coupled and Decoupled Parallel Mechanisms". Chinese Journal of Mechanical Engineering, 23(4), pp. 468-476, 2010. http://doi.org/10.3901/CJME.2010.04.468

[25] Yang T, L.;Liu, X, A.; Shen, H. P., HangL, B.; Luo Y, F.; Jin Q.; "Topology Design of Robot Mechanisms".Springer, Singapore, 2018. http://doi.org/10.1007/978-981-10-5532-4

[26] Hou, Y, L.; Zeng, D, X.; Zhang, Z, Y.; Wang, C, M.; Hu, X, Z.; "A Novel Two Degrees of Freedom Rotational Decoupled Parallel Mechanism". 2nd International Conference on Advanced Design and Manufacturing Engineering, Taiyuan, People's Republic of China, 2012. http://doi.org/10.4028/www.scientific.net/AMM.215-216.293

[27] Yu, S, S.; Zhang, J, J.; Li, W, M.; Yang, X, H.; "New Decoupled 2-Dof Parallel Mechanism with Fully Spherical Workspace".5th Annual International Conference on Information System and Artificial Intelligence, Zhejiang, People's Republic of China, 2020. http://doi.org/10.1088/1742-6596/1575/1/012104

[28] Shu, L. S., Wang, B., He, Y. Y.,"Optimization of Process Parameters of Laser Cladding 304L Alloy Powder Based on Orthogonal Experiment".Mechanical Engineering Science, 1(2), pp. 18-24, 2019. https://doi.org/10.33142/me.v1i2.1656

JJMIE

Volume 15, Number 5, December. 2021
ISSN 1995-6665
Pages 431 – 439

Jordan Journal of Mechanical and Industrial Engineering

Application of Potential Energy Method for Driver Seat Suspension System Using Quasi-Zero Stiffness: A Numerical and Experimental Study

Mostafizur Rahman, Md. Arafat Rahman*

Department of Mechanical Engineering - Chittagong University of Engineering &Technology, Chattogram-4349, Bangladesh

Received September 16 2020 *Accepted October 6 2021*

Abstract

To improve comfort, a quasi-zero stiffness (QZS) drivers' seat suspension system is designed and fabricated based on potential energy method. At first, the mathematical model for the seat suspension is established. Thereafter, a model of seat suspension system with natural frequency of 2.45 Hz is fabricated to check validity of this method. A negative stiffness spring (NSS) is used as added system to reduce the natural frequency to 1.78 Hz. In addition, double NSS is added to suspension system to obtain QZS and natural frequency observed to near about 0.84 Hz. Hence, vibration magnitude of seat suspension is reduced to 27.3% in case of single NSS and 65.7% for double NSS compared with suspension system without NSS. Compared with the original seat suspension system, the new suspension system with NSS has better vibration isolation characteristics and can electively improve drivers' ride comfort.

Keywords: Vibration; Natural frequency; Transmissibility; Suspension system; Potential energy; Quasi-zero stiffness; Stability;

1. Introduction

While riding and driving, vehicles' drivers seem to be exposed to much vibration which causes uncomfortable and pain to body resulting in decreasing their working period as well as working efficiency[1]. An important requirement of vehicle design is to attenuate vibration level transmitted to driver's seat from chassis[2]. Vibration is unwanted and anticipated not only in human body but also in any engineering structure and in vehicle seat suspension system as well due to stability and life cycle concern[3, 4]. This type of unexpected vibration needs to be remedied by designing proper and an efficient seat suspension system. It is noted that purchasing vehicle is selective criterion which is not only limited by development of horse power or torque of the engine, fuel economy condition, and hundred km/h speed of vehicle[5]. Hence, an efficient, low natural frequency, and low vibration transmissibility seat suspension system is taken into consideration with great importance while designing vehicle[6]. Suspension designer can model seat suspension system by three categories, such as active, semi-active, and passive system [7]. Active system is capable of reducing natural frequency below 1 Hz using control units along with common suspension elements, such as mass, spring, and damper[8]. A renowned company 'BOSE' developed an active system of cost about $5000 which is very high with respect to commonly used passenger car [9]. In addition, 'ISUZU' company fabricated a semi-active system of natural frequency below 1 Hz of cost about $4000[10]. A seat suspension system of low natural frequency means the system is efficient in attenuating vibration magnitude. However, suspension designer needs to think about performance and cost at the same time when he/she designs. In contrast, active and semi-active system cannot function properly in very rough and tough environment if controlling unit is failed[11]. Passive system can be a better choice for high speed, heavy-duty, industrial, and agricultural vehicles in terms of performance and cost as well[12]. It is noted that natural frequency of passive suspension system is observed between 1-2 Hz which is used in most of the passenger's vehicles[13]. Hence, passive system needs to be modified in such way that it can attenuate vibration below natural frequency of 1 Hz. In addition, passive suspension system is modeled as single degree of freedom (SDOF) system consisting of mass, springs, and dampers as shown in Fig. 1. Mass of the driver seat includes mass of suspension frame, seat cushion, and mass of driver itself. This mass is supported by a spring with stiffness (K) and a damper with damping co-efficient (C).

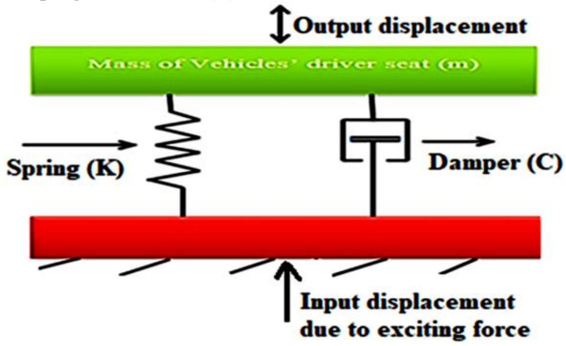

Figure 1. Schematic representation of SDOF damped passive seat suspension system.

* Corresponding author e-mail: arafat@cuet.ac.bd.

It is noted that un-damped natural frequency of the system can be given as follows

$$f_n=\frac{1}{2\pi}\sqrt{\frac{K}{m}} \quad (1)$$

In addition, damped natural frequency is written as

$$f_d=f_n\sqrt{1-\zeta^2} \quad (2)$$

where damping ratio, $\zeta=\frac{C}{2\sqrt{mK}}=\frac{\text{Actual damping}}{\text{Critical damping}}$

It is worthy to mention that $f_d < f_n$ and it will obviously be better for comfort if un-damped natural frequency is near about or below damped natural frequency[14]. Because damper is a sophisticated and costly suspension element, for simplicity, damper in passive suspension system can be replaced by some approaches capable of reducing natural frequency and vibration transmissibility. Hence, un-damped passive system needs to be designed in such way that it can reduce level of vibration below 1 Hz. It is highly essential to understand the source of vibration, its nature and direction, the transmission path of the vibration energy to problem location, and natural frequency before designing un-damped passive system. Figure 2 shows vibration transmission model to vehicles' driver seat. As noted, vibration transmission path is the main point where different modifications are performed to increase vibration attenuation bandwidth. Design modifications on source and sink do not reduce vibration transmissibility whereas; vibration transmission path has received more attentions from automotive engineers for minimizing vibration. Several analytical, numerical, and experimental approaches have been developed for investigating the response of suspension system with added system, such as negative stiffness system (NSS).Hall et al. [15] reported vehicle seat vibration isolation and motion control through use of horizontal non-linear springs and slender beam structure. Kashdan et al. [16]designed and constructed a constrained bi-stable structure with negative stiffness behavior for providing extreme vibrational absorptive capacity. In addition, Meng et al. [17]designed and presented a novel quasi-zero stiffness vibration isolator by combining a disk spring as negative stiffness element with a vertical linear spring.

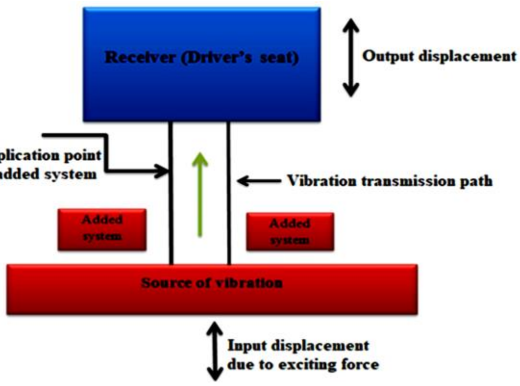

Figure 2. Added system to vibration transmission path (Reproduced from [13])

Palomares et al.[18]fabricated a suspension system consisting of vertical pneumatic spring with a damper and two pneumatic linear actuators for controlling vibro-isolation properties of suspension system. However, Rahman et al.[19]designed and proposed a vehicle drivers' seat suspension system totally in passive way using double negative stiffness system. In this study, un-damped passive seat suspension system is designed using double NSS as added system to vibration transmission path. Model of modified passive seat suspension system is mathematically analyzed by potential energy method. A new seat suspension system is fabricated and experimentally investigated for validation of mathematical model.

2. Mathematical Modeling by Potential Energy Method

Conventional un-damped passive seat suspension system consists of a payload mass and linear vertical spring and it is capable of reducing natural frequency below 1 Hz if the linear vertical spring is of at least 0.2 m which is practically unfeasible[20]. Equation (1) signifies that natural frequency is decreased by two ways: such as increasing mass and decreasing stiffness. However, those are not effective in actual practice since increasing mass of the system leads to increase the bulkiness of system[21]. In addition, stiffness of spring needs to be increased at the same time for reduction of vertical static displacement and stable support of as mass[22]. However, natural frequency is not reduced. In contrast, decreasing stiffness of vertical spring is not an effective way to reduce natural frequency due to large static deflection. This dichotomy relation of mass and spring with natural frequency of the suspension system is eliminated by implying quasi-zero stiffness. Here, NSS which is itself a unstable system, can be added with main system to obtain quasi-zero stiffness for reducing natural frequency. Figure 3 shows a new seat suspension system with double NSS. Here, mass (M) is moved downward due to externally applied force; vertical spring becomes compressed and gains potential energy. It tends to bring back the mass in equilibrium position very quickly due to restoring force resulting in much vibration. Hence, vertical spring faces resistance to going back to equilibrium position very quickly if NSS is added as supplementary system. NSS reduces functional stiffness of total system without reducing own stiffness of vertical spring. It will be clear from mathematical relationship obtained by potential energy method.

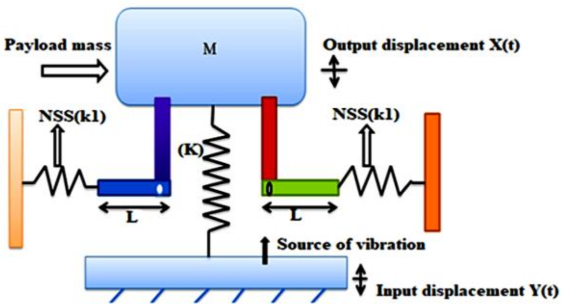

Figure 3. Schematic representation of un-damped passive seat suspension system with double NSS.

Potential energy of the system as shown in Fig. 3 without NSS can be given as follows

$$U_1=\frac{1}{2}KX^2 \quad (3)$$

In addition, potential energy of the added double NSS system can be written as

$$U_2 = \frac{1}{2} \times 2k_1(\partial_O + \sqrt{L^2 - X^2} - L)^2$$

$$= k_1(\partial_O + \sqrt{L^2 - X^2} - L)^2 \quad (4)$$

where, ∂_o is initial deflection of spring of NSS from equilibrium position when subjected to designed payload mass. Hence, total potential energy of the system can be reduced to, $U=U_1+U_2$

$$U(x) = \frac{1}{2} KX^2 + k_1(\partial o + \sqrt{L^2 - X^2} - L)^2 \quad (5)$$

It is noted that 1st derivative of potential energy function of an elastic system with respect to displacement is spring force[23]. From Equation (5), it can be written as

$$\frac{\partial U}{\partial X} = KX - 2k_1\left\{1 + \frac{\partial_o - L}{\sqrt{L^2 - X^2}}\right\}X \quad (6)$$

In addition, 2nd derivative of potential energy function of an elastic system with respect to displacement is stiffness of that elastic system[23].Hence, Equation (6)is reduced to

$$\frac{\partial^2 U}{\partial X^2} = K - 2k_1 - \frac{\partial}{\partial x}\left\{\frac{(\partial_o - L)X}{\sqrt{L^2 - X^2}}\right\} \quad (7)$$

Equation 7 represents that it is non-linear stiffness equation. It is noted that the only term K (stiffness) exists in this equation when it is treated as linear stiffness equation. It is worthy to mention that the other term is canceled out if we consider ∂_o=L (initial deflection of NSS spring equal to bar length). Hence, the system will be linear. It is noted that natural frequency of linear system is lower than the natural frequency of non-linear system[24]. Hence, from Equation (5) potential energy function can be written at ∂_o=L as follows,

$$U(x) = \frac{1}{2} KX^2 + k_1L^2 - k_1X^2 \quad (8)$$

From Equation (6), spring force can be written at ∂_o=L as follows,

$$F(X) = KX - 2k_1X \quad (9)$$

From Equation (7), stiffness of the system can be shown at ∂_o=L as follows,

$$\frac{\partial^2 U}{\partial X^2} = K_{Total} = K - 2k_1 \quad (10)$$

Natural frequency is as follows,

$$f_n = \frac{1}{2\pi}\sqrt{\frac{K_{Total}}{M}} = \frac{1}{2\pi}\sqrt{\frac{K - 2k_1}{M}} \quad (11)$$

In addition, displacement transmissibility can be reported as,

$$\frac{X}{Y} = \sqrt{\frac{1 + 4\zeta^2\left(\frac{f}{f_n}\right)^2}{\left(1 - \left(\frac{f}{f_n}\right)^2\right)^2 + 4\zeta^2\left(\frac{f}{f_n}\right)^2}} \quad (12)$$

Displacement transmissibility becomes, $\frac{X}{Y} = \sqrt{\frac{1}{(1-r^2)^2}}$ as no damping element ζ is used in model as shown in Fig. 3, where frequency ratio, $r = \frac{f}{f_n} = \frac{\text{Exciting frequency}}{\text{Natural frequency}}$. It is noted that exciting frequency means the frequency at which the seat suspension system vibrates due to external disturbances. ζ= damping ratio of seat suspension system $= \frac{\text{Actual damping}}{\text{Critical damping}}$.The NSS subtracts stiffness from vertical spring without reducing its own main stiffness. Furthermore, double NSS subtracts equal to its twice stiffness, and resultant stiffness should be as low as possible to lower natural frequency. Stiffness difference between vertical spring and NSS should always be positive, never can be equal to zero or negative for stability concern[25]. It is worthy to mention that considering stiffness of spring, seat suspension system needs to be designed in such way that stiffness difference tends to be zero, not exactly equal to zero, which is termed as Quasi-Zero stiffness[22-23]. Suspension elements should better be strong enough to withstand static load and at the same time, should be soft enough to absorb vibration, as it is required in designing suspension system[27]. It is contradictory, however, that seat suspension system having quasi-zero stiffness results in high static stiffness to carry payload and low dynamic stiffness to absorb vibration for reducing natural frequency.

Figure 3 shows three types of seat suspension using NSS as supplementary system. Figure 3(a) has been modified by using single NSS and Fig. 3(b) by another NSS.

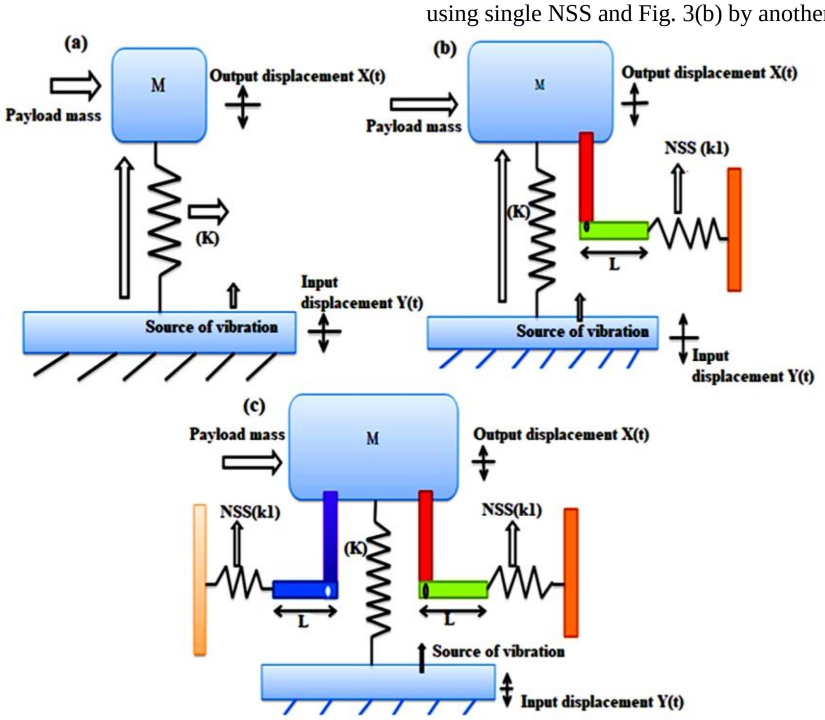

Figure 3. Schematic representation of Un-damped passive seat suspension system: (a) without NSS (b) with single NSS (c) with double NSS.

Effect of adding NSS with original system is to reduce natural frequency shown in Fig. 4. As noted natural frequency is obtained as 2.34 Hz against total mass, M=25 kg (Dead mass 15 kg, seat mass 7.5 kg and suspension seismic mass 2.5 kg) with only vertical spring of stiffness K=5500 N/m. Natural frequency is reduced to 1.70 Hz by adding single NSS of stiffness 2500 N/m and to 0.81 Hz adding double NSS of same stiffness. However, Wanget al.[28] reported natural frequency of below 1 Hz using damped suspension parameters. Hence, un-damped system shows better effectiveness than retrospectively damped one. In addition, vibration attenuation power of seat suspension with single NSS is more than suspension without NSS at high frequency. However, vibration attenuation power of seat suspension with double NSS is more than suspension system without NSS and with single NSS.

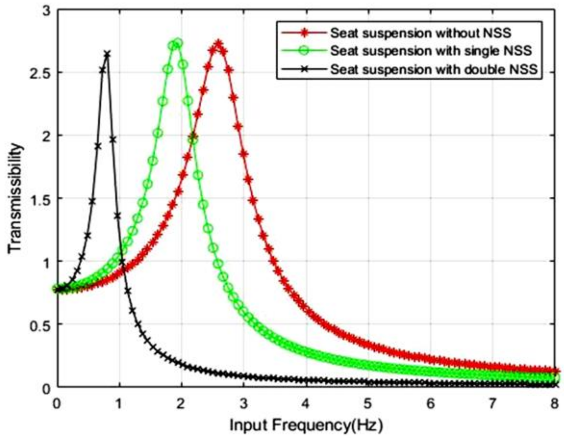

Figure 4. Variation of transmissibility with exciting input frequency for un-damped system during mathematical simulation.

Vibration transmission path is modified by using NSS replacing damper collaterally arranged with vertical spring, as this study is not dealing with damper used in seat suspension. A conventional damped system slightly reduces natural frequency and transmissibility as compared with un-damped seat suspension system with double NSS shown in Fig. 5. Figure 5 shows variation of natural frequency and vibration transmissibility of damped system for different damping co-efficient. Damped system consisting of vertical spring (stiffness 5500 N/m) collaterally arranged with a damper with damping co-efficient of 10 Ns/m, 20 Ns/m, and 30 Ns/shows natural frequency of 0.82 Hz. In addition, increasing damping co-efficient keeps natural frequency almost same. However, change of transmissibility is not significantly observeddue to changing viscous damping property. In contrast, 0.81 Hz natural frequency is obtained from seat suspension with double NSS, which is slightly lower than damped system.

Potential energy is a big factor for analysis vibration of vibrating system. If the change of slope of potential energy curve of SDOF with respect to displacement is reduced, then natural frequency and vibration transmissibility of that system is decreased[29]. Figure 6 shows that potential energy curve is obtained from upward and downward displacement of 3 mm from equilibrium position. It is noted that slope of the potential energy curves has relation such as a>b>c.Hence,itindicates slope of potential energy curve of seat suspension system with double NSS is lower than slope of potential energy curve of seat suspension system with single NSS and slope of potential energy curve of seat suspension system without NSS. It is concluded that lower slope of potential energy curve means slow releasing of restoring energy and more vibration attenuation bandwidth. In addition, the potential function is a convex one when an isolation system is stable [25]. Furthermore, the potential function of the added system is a concave function and it achieves the maximum value at the equilibrium point as shown in Fig. 6. Hence, the proposed new seat suspension with NSS is stable system as the potential function is a convex one as shown in Fig. 6.

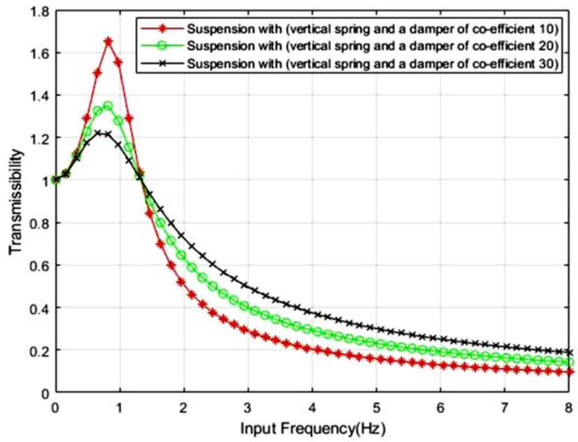

Figure 5. Variation of transmissibility with exciting input frequency for damped system during mathematical simulation.

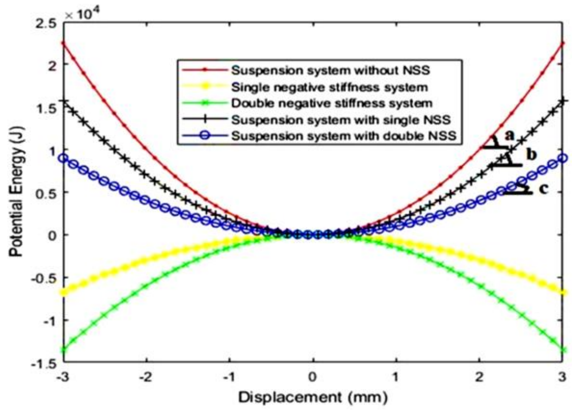

Figure 6. Change of potential energy of un-damped passive system during mathematical simulation.

In addition, the stability of seat suspension system shown in this study is further analyzed by varying damping co-efficient. The influences of suspension parameters are focused on improving vibration isolation performance neglecting the stability concern. Stability of suspension system is studied by varying exciting force frequency, exciting force acceleration, non-linearity of springs, and damping co-efficient [30].Varying damping co-efficient is an alternative way to check stability for an un-damped system [31]. Varying damping co-efficient has significant effect on displacement transmissibility ratio from Eqn. (12) and resonance frequency as shown in Fig.7. Amplitude of response and resonance frequency of seat suspension system without and with double NSS is increased and decreased in similar fashion with the increase and decrease of damping co-efficient as shown in Figs.7(a) and 7(b) respectively. However, it is reported that the stability conditions are independent of the excitation amplitude[32]. It is noted that any bifurcation of response and resonance frequency is not observed in Figs.7(a) and 7(b) with sudden jump down or jump up in unstable region[33].For a structurally unstable system, the bifurcation point is the critical value of a parameter that triggers a sudden or 'catastrophic' change in the response[33].In addition, increasing in damping co-efficient led to the reduction of transmissibility in resonant region with that in higher frequencies unaffected[35]. Furthermore, the unstable regions are decreased as the damping radio increases. This similar phenomenon also observed during analysis of stability of system with quasi-zero stiffness vibration isolator[36]. Hence, the solution of differential equation obtained from mathematical modeling of seat suspension system is stable[37]. Therefore, this feature can improve the isolation performance of the seat suspension system in a certain extent.

3. Working Principle of NSS

NSS is used as added system with main system in order to increase vibration isolation bandwidth of seat suspension system[38]. It is noted that NSS as an added system is unstable, but can be stable when combined with main system[39]. It consists of horizontal tensional springs, one link connected with upper frame of suspension system, and another link moves upward and downward. Furthermore, one end of horizontal spring is fixed at supporting stand, and other end with the moving shaft. Spring connected with shaft moves right to left and vice-versa through horizontal moving rail as shown in Fig. 8.

Negative stiffness springs are in equilibrium position as shown in Fig. 9(a). In contrast, when connecting, links move upward due to movement of system, upper links tend to move upward and the bar moves right to left and vice-versa as shown in Figs. 9(b) and 9(c). Negative stiffness springs reduce stiffness from vertical spring functionally not actually during movement and tend to make resistance at the time of sudden movement of vertical spring toward upward and downward direction. Total system is forced to move upward and downward direction slowly as a result the system experiences low magnitude vibration. This is the way NSS subtracts stiffness equal to its own from vertical spring as shown in Fig. 9. As seen, the system is in equilibrium position in Fig. 9(a), upward position in Fig. 9(b), and downward position in Fig. 9(c).

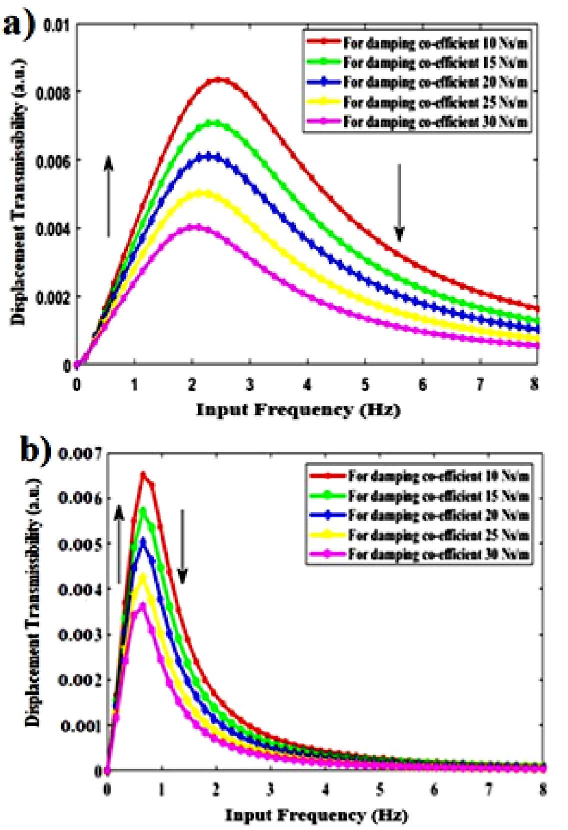

Figure 7. Effect of varying damping co-efficient on displacement transmissibility of seat suspension (a) without and (b) with double NSS.

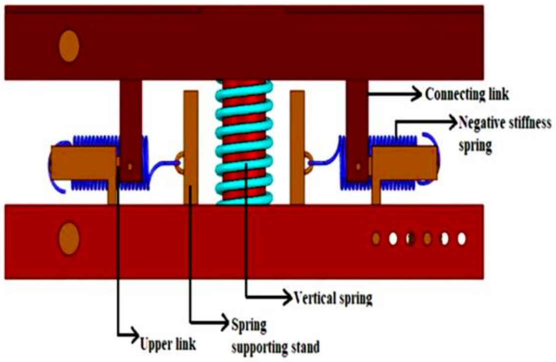

Figure 8. CAD model of structure of NSS.

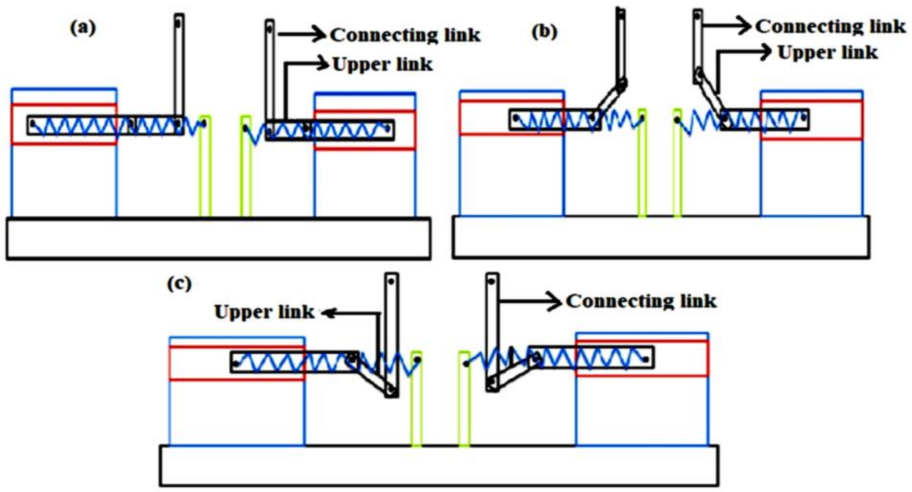

Figure 9. Working principle of NSS when system at (a) equilibrium position, (b) upward position, and (c) downward position.

4. Experimental Model

An efficient low natural frequency seat suspension system is a compromise between vibrating environment, working period, and working efficiency of people[40].Efficiency of seat suspension system depends on reducing displacement transmissibility, increasing vibration attenuation bandwidth and increased by modifying seat suspension parameters[41]. In this work, CAD model of experimental setup shown in Fig. 6consists of three major sections such as mechanical vibration exciter, suspension system, and seat with dead weight. Firstly, CAD model is developed considering design parameters. Furthermore, experimental model is fabricated exactly considering the design parameters. Figure10 shows the CAD model and Table 1 lists the design parameters used in fabricating suspension system. Stiffness of vertical spring and NSS are measured precisely both numerically and experimentally. Other geometries of different parts are measured very carefully.

In addition, four knuckles of dimension (length: 380mm, width: 25mm, thickness: 3mm), four horizontal and vertical bars of (length: 80mm, width: 10mm and thickness: 3mm), upper frame and lower frame of same dimensioning (length: 560mm, width: 460mm, material thickness of 3mm) are assembled to make experimental setup. A square shaped mechanical vibration exciter (72cm×72cm) consisting of six spring of same stiffness (1500 N/m), shaft-pulley bearing mechanism connected with motor shaft through a belt is used to create exciting force for giving input displacement.

Table 1. Parameters used in designing suspension system

Serial No.	Name	Value
01	Mass (M)	25 Kg
02	Stiffness of main spring (K)	5500 N/m
03	Stiffness of negative spring (k_1)	2500 N/m
04	Initial length of negative stiffness spring	130 mm
05	Bar Length (L)	70 mm
06	Initial deflection of spring (∂_o)	70 mm

An inverter (Micro-processor/DSP, IGDP, 50 HZ, PF>0.9) is used to control motor speed for shaking exciter top surface at different electric frequency. Figure 11(a) shows single negative stiffness spring and Fig. 11(b) shows double negative stiffness spring added with main system to reduce natural frequency. An accelerometer (Brand: Lutron, Model: BVB-8207SD, SD card with data logger) having four magnetic probes is used for taking peak-to-peak displacement, peak velocity and acceleration reading. Exciting frequency of exciter top surface occurs using the above-mentioned readings as shown in Fig. 11(c). Driver seat is mounted on the top surface of the exciter as shown in Fig. 11(d), which excites at high frequency with increase of motor speed and at low frequency with decrease of motor speed.

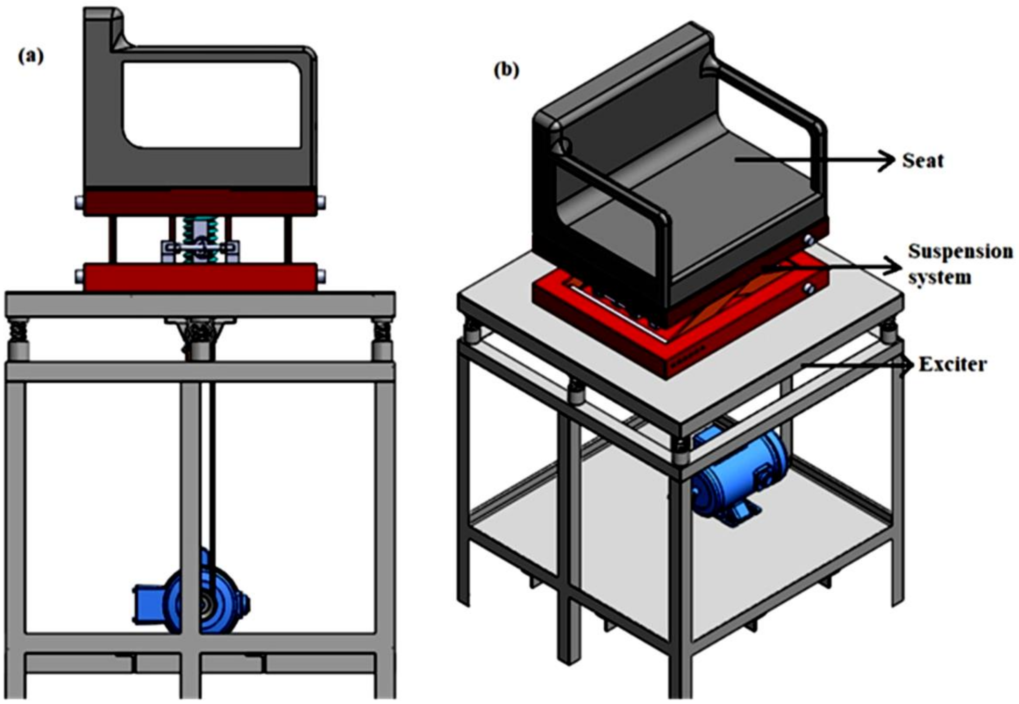

Figure 10.CAD model of experimental set up (a) front view (b) isometric view

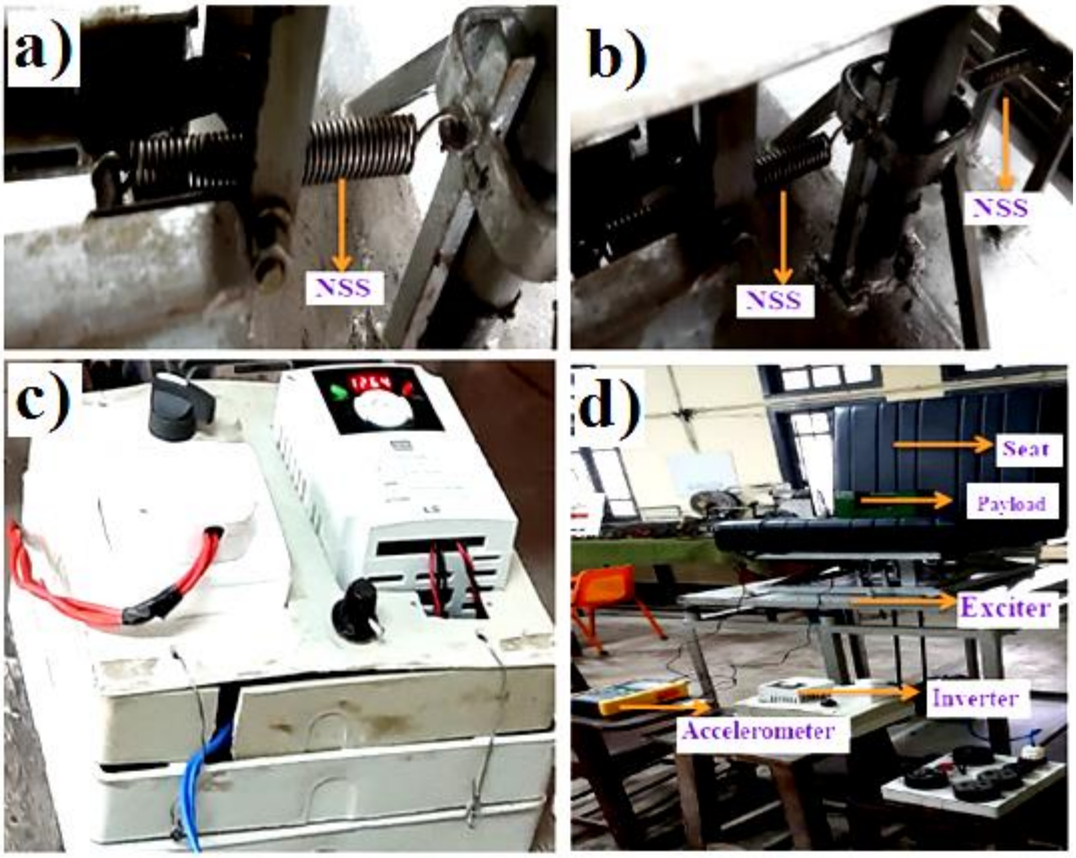

Figure 11. Images of (a) Single negative stiffness spring (b) Double negative stiffness spring (c) Inverter circuit (d) Experimental model.

In order to calculate displacement transmissibility, displacement reading of exciter top surface is taken as input signal whereas displacement of seat as output signal. Motor starts to run, and exciter tends to shake the system at about 7 Hz electric frequency. This process was continued up to 24 Hz of electric frequency with the increment of 1 Hz frequency consecutively, and peak-to-peak displacement, peak velocity and acceleration readings against each frequency are saved in external storage of accelerometer.

5. Experimental Results and Discussion

Effect of adding NSS with main system is shown in Fig. 12 obtained from experimental investigation. Four channels of vibration meter (Brand: Lutron, Model: BVB-8207SD) was used to take readings such as displacement, velocity, and acceleration with different exciting frequency. Natural frequency of 2.45 Hz is obtained for main system without NSS. However, natural frequency is reduced to 1.78 Hz for adding single NSS with main system.

In addition, 0.84 Hz natural frequency, a significant change is obtained from system with double NSS. It is worthy to mention that 26.3% and 65.88% vibration magnitude is reduced in case of using single NSS and double NSS with main system, respectively. In this study, there is some variation observed between mathematical simulation and experimental results. Main causes of this variation are due to the non-linearity, unbalancing of model in dynamic condition, dry friction among various parts, and improper machining of the parts assembled. In addition, linearity condition is considered for formulating mathematical equations. However, non-linearity exists in the experimental setup. Variation in natural frequency between mathematical simulation and experimental results of 4.6% for original seat suspension system without NSS, 4.9% for single NSS with main system and 3.96% for double NSS with main system is observed.

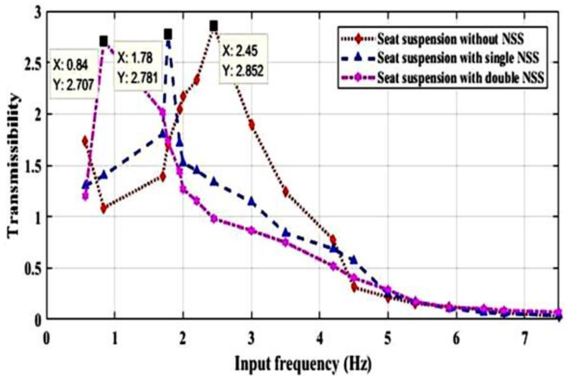

Figure 12. Comparison of natural frequency and transmissibility from experimental investigation.

6. Conclusions

This study represents an experimental and mathematical investigation on a driver seat suspension fabricated by using quasi-zero stiffness system. Adding of NSS with un-damped seat suspension system to decrease potential energy and natural frequency shows the ability of vibration attenuation bandwidth. At first, a setup is modeled with natural frequency of 2.34 Hz using mass-spring system without any NSS. Mathematical simulation results show that natural frequency of modified model can be reduced to 1.69Hz using single NSS and to 0.81 Hz using double NSS. In addition, natural frequency of 2.45 Hz for without NSS, 1.78 Hz for single NSS, and 0.84Hz for double NSS are observed from experimental results. Hence, vibration magnitude of seat suspension is reduced to 27.3% in case of single NSS and 65.7% for double NSS compared with suspension system without NSS. This type of un-damped passive seat suspension system will be costly economically compared to semi-active and active system. In addition, damper costis considered about $500 whereas replacing damper by adding double NSS with original seat suspension system costs about $70. Proposed seat suspension system is comparably suited in vehicles' driver seat in the context of vibration attenuation power, low cost, simplicity in design and installation. In addition, vibration attenuation mechanism using quasi-zero stiffness is applicable in machine having continuous vibrating parts, rotating shafts, and in machines such as brick breaking, concrete mixing, portable rice mill, sewing machine, and in agricultural machines.

Acknowledgements

This research is financially supported by Directorate of Research & Extension (DRE), Chittagong University of Engineering and Technology, Chittagong-4349, Bangladesh through research project entitled of "Design and fabrication of low natural frequency driver seat suspension system".

Conflicts of Interest: The authors declare no Conflict of interest.

References

[1] G. J. Stein, R. Zahoransky, T. P. Gunston, L. Burstro, and L. Meyer, "Modelling and simulation of a fore-and-aft driver ' s seat suspension system with road excitation," vol. 38, pp. 396–409, 2008, doi: 10.1016/j.ergon.2007.10.016.

[2] M. A. Książek and D. Ziemiański, "Optimal driver seat suspension for a hybrid model of sitting human body," *J. Terramechanics*, vol. 49, no. 5, pp. 255–261, 2012, doi: 10.1016/j.jterra.2012.07.001.

[3] S. M. Nacy, N. K. Alsahib, and F. F. Mustafa, "Vibration Analysis of Plates With Spot Welded Stiffeners," *Jordan Journal of Mechanical and Industrial Engineering , Vol.*, vol. 3, no. 4, pp. 272–279, 2009.

[4] X. Sun and X. Jing, "A nonlinear vibration isolator achieving high-static-low-dynamic stiffness and tunable anti-resonance frequency band," *Mech. Syst. Signal Process.*, vol. 80, pp. 166–188, 2016, doi: 10.1016/j.ymssp.2016.04.011.

[5] Y. Bian, Z. Gao, J. Hu, and M. Fan, "ACCEPTED MANUSCRIPT A semi-active control method for decreasing longitudinal torsional vibration of vehicle engine system : theory and experiments," *J. Sound Vib.*, 2018, doi: 10.1016/j.jsv.2018.09.051.

[6] I. Maciejewski, S. Glowinski, and T. Krzyzynski, "Active control of a seat suspension with the system adaptation to varying load mass," *Mechatronics*, vol. 24, no. 8, pp. 1242–1253, 2014, doi: 10.1016/j.mechatronics.2014.10.008.

[7] D. Ning, S. Sun, J. Zhang, H. Du, W. Li, and X. Wang, "An active seat suspension design for vibration control of heavy-duty vehicles," *J. Low Freq. Noise, Vib. Act. Control*, vol. 35, no. 4, pp. 264–278, 2016, doi: 10.1177/0263092316676389.

[8] K. Rajagopal and L. Ponnusamy, "Hybrid DEBBO algorithm for tuning the parameters of PID controller applied to vehicle active suspension system," *Jordan Journal of Mechanical and Industrial Engineering.*, vol. 9, no. 2, pp. 85–101, 2015.

[9] L. Thanh and K. Kwan, "Active pneumatic vibration isolation system using negative stiffness structures for a vehicle seat," *J. Sound Vib.*, vol. 333, no. 5, pp. 1245–1268, 2014, doi: 10.1016/j.jsv.2013.10.027.

[10] R. Jeyasenthil and S. B. Choi, "Mechatronics A novel semi-active control strategy based on the quantitative feedback theory for a vehicle suspension system with magneto-rheological damper," *Mechatronics*, vol. 54, no. June, pp. 36–51, 2018, doi: 10.1016/j.mechatronics.2018.06.016.

[11] H. R. Fernandes and A. P. Garcia, "ScienceDirect Design and control of an active suspension system for unmanned agricultural vehicles for field operations," *Biosyst. Eng.*, vol. 174, pp. 107–114, 2018, doi: 10.1016/j.biosystemseng.2018.06.016.

[12] D. Cakmak, H. Wolf, and M. Joki, "Passive and active vibration isolation systems using inerter," vol. 418, pp. 163–183, 2018, doi: 10.1016/j.jsv.2017.12.031.

[13] P. S. Tae and S. C. Banik, "Design of a Vehicle Suspension System with Negative Stiffness System," *IST Trans. Mech. Sys. - Theory Appl.*, vol. 1, no. 1, pp. 6–12, 2010.

[14] R. N. Yerrawar and R. R. Arakerimath, "ScienceDirect Development of Methodology for Semi Active Suspension System Using MR Damper," *Mater. Today Proc.*, vol. 4, no. 8, pp. 9294–9303, 2017, doi: 10.1016/j.matpr.2017.07.289.

[15] H. Hall, S. Loghavi, R. Singh, and S. Noll, "Analysis of Negative Stiffness Devices with Application to Vehicle Seat Suspensions," no. April, 2015, [Online]. Available: https://kb.osu.edu/dspace/bitstream/handle/1811/68613/1/Saeid_Thesis_RS_4-15.pdf.

[16] L. Kashdan, C. C. Seepersad, M. Haberman, and P. S. Wilson, "Design, fabrication, and evaluation of negative stiffness elements using SLS," *Rapid Prototyp. J.*, vol. 18, no. 3, pp. 194–200, 2012, doi: 10.1108/13552541211218108.

[17] L. Meng, J. Sun, and W. Wu, "Theoretical Design and Characteristics Analysis of a Quasi-Zero Stiffness Isolator Using a Disk Spring as Negative Stiffness Element," *Shock Vib.*, vol. 2015, pp. 1–19, 2015, doi: 10.1155/2015/813763.

[18] E. Palomares, A. J. Nieto, A. L. Morales, J. M. Chicharro, and P. Pintado, "Numerical and experimental analysis of a vibration isolator equipped with a negative stiffness system," *J. Sound Vib.*, vol. 414, pp. 31–42, 2017, doi: 10.1016/j.jsv.2017.11.006.

[19] M. Rahman, M. A. Rahman, M. A. M. Hossain, F. A. Koly, and M. M. M. Talukder, "MATHEMATICAL SIMULATION OF DRIVER SEAT SUSPENSION SYSTEM USING QUASI-ZERO STIFFNESS SYSTEM," vol. 2019, no. April, 2019.

[20] A. A. et al. . Assaad Alsahlani et al., "Design and Analysis of Coil Spring in Vehicles Using Finite Elements Method," *Int. J. Mech. Prod. Eng. Res. Dev.*, vol. 8, no. 4, pp. 615–624, 2018, doi: 10.24247/ijmperdaug201864.

[21] M. Zhao, "Is the negative equivalent stiffness of a system possible?," *Phys. Educ.*, vol. 51, no. 1, 2016, doi: 10.1088/0031-9120/51/1/013002.

[22] M. Ghadiri, K. Malekzadeh, and F. A. Ghasemi, "Free vibration of an axially preloaded laminated composite beam carrying a spring-mass-damper system with a non-ideal support," *Jordan Journal of Mechanical and Industrial Engineering.*, vol. 9, no. 3, pp. 195–207, 2015.

[23] A. Rahman, B. Salam, and T. Islam, "An Improved Design of Anti Vibration Mount for lower Natural Frequency," 2010.

[24] A. G. Mohite and A. C. Mitra, "Development of Linear and Non-linear Vehicle Suspension Model," *Mater. Today Proc.*, vol. 5, no. 2, pp. 4317–4326, 2018, doi: 10.1016/j.matpr.2017.11.697.

[25] S. T. Park and T. T. Luu, “A new method for reducing the natural frequency of single degree of freedom systems,” *J. Sound Vib.*, vol. 300, no. 1–2, pp. 422–428, 2007, doi: 10.1016/j.jsv.2006.08.017.

[26] W. S. Robertson, M. R. F. Kidner, B. S. Cazzolato, and A. C. Zander, “Theoretical design parameters for a quasi-zero stiffness magnetic spring for vibration isolation,” *J. Sound Vib.*, vol. 326, no. 1–2, pp. 88–103, 2009, doi: 10.1016/j.jsv.2009.04.015.

[27] R. Kieneke, C. Graf, and J. Maas, “Active seat suspension with two degrees of freedom for military vehicles,” *IFAC Proc. Vol.*, vol. 46, no. 5, pp. 523–529, 2013, doi: 10.3182/20130410-3-CN-2034.00085.

[28] A. Heidarian and X. Wang, “Review on seat suspension system technology development,” *Appl. Sci.*, vol. 9, no. 14, 2019, doi: 10.3390/app9142834.

[29] K. Deprez, D. Moshou, J. Anthonis, J. De Baerdemaeker, and H. Ramon, “Improvement of vibrational comfort on agricultural vehicles by passive and semi-active cabin suspensions,” *Comput. Electron. Agric.*, vol. 49, no. 3, pp. 431–440, 2005, doi: 10.1016/j.compag.2005.08.009.

[30] J. Yao, J. Q. Zhang, M. M. Zhao, and Z. J. Wei, “Analysis of dynamic stability of nonlinear suspension,” *Adv. Mech. Eng.*, vol. 10, no. 3, pp. 1–10, 2018, doi: 10.1177/1687814018766648.

[31] S. P. Mhatre, S. Hatwalane, S. Thorat, and B. S. Kothavale, “Semi - Active Suspension system with M . R . Damper for car seat vibratio n - A Review,” vol. 4, no. 4, pp. 391–394, 2016.

[32] C. Cheng, S. Li, Y. Wang, and X. Jiang, “Force and displacement transmissibility of a quasi-zero stiffness vibration isolator with geometric nonlinear damping,” *Nonlinear Dyn.*, vol. 87, no. 4, pp. 2267–2279, 2017, doi: 10.1007/s11071-016-3188-0.

[33] K. Chai, J. Lou, Q. Yang, and S. Liu, “Characteristic analysis of vibration isolation system based on high-static-low-dynamic stiffness,” *J. Vibroengineering*, vol. 19, no. 6, pp. 4120–4137, 2017, doi: 10.21595/jve.2017.18268.

[34] A. Papangelo, M. Ciavarella, and N. Hoffmann, “Subcritical bifurcation in a self-excited single-degree-of-freedom system with velocity weakening–strengthening friction law: analytical results and comparison with experiments,” *Nonlinear Dyn.*, vol. 90, no. 3, pp. 2037–2046, 2017, doi: 10.1007/s11071-017-3779-4.

[35] N. K. A. Al-sahib, A. N. Jameel, and O. F. Abdulateef, “Investigation into the Vibration Characteristics and Stability of A Welded Pipe Conveying Fluid,” *Jordan Journal of Mechanical and Industrial Engineering.*, vol. 4, no. 3, pp. 378–387, 2010.

[36] A. D. Shaw and A. Carrella, “Force displacement curves of a snapping bistable plate,” *Conf. Proc. Soc. Exp. Mech. Ser.*, vol. 3, pp. 191–197, 2012, doi: 10.1007/978-1-4614-2416-1_14.

[37] Q. Wu, Z. Ma, and L. Zhang, “Numerical simulation and nonlinear stability analysis of Francis Hydraulic Turbine-Seal system,” *Jordan Journal of Mechanical and Industrial Engineering.*, vol. 9, no. 4, pp. 253–261, 2015.

[38] H. Pu, S. Yuan, Y. Peng, K. Meng, J. Zhao, and R. Xie, “Multi-layer electromagnetic spring with tunable negative stiffness for semi-active vibration isolation,” *Mech. Syst. Signal Process.*, vol. 121, pp. 942–960, 2019, doi: 10.1016/j.ymssp.2018.12.028.

[39] T. D. Le and K. K. Ahn, “A vibration isolation system in low frequency excitation region using negative stiffness structure for vehicle seat,” *J. Sound Vib.*, vol. 330, no. 26, pp. 6311–6335, 2011, doi: 10.1016/j.jsv.2011.07.039.

[40] M. Hoić, N. Kranjčević, Z. Herold, and M. Kostelac, “Design of an Active Seat Suspension for a Passenger Vehicle,” *Proc. Des. Soc. Des. Conf.*, vol. 1, no. 2019, pp. 2511–2520, 2020, doi: 10.1017/dsd.2020.119.

[41] T. Mizuno, M. Takasaki, D. Kishita, and K. Hirakawa, “Vibration isolation system combining zero-power magnetic suspension with springs,” *Control Eng. Pract.*, vol. 15, no. 2, pp. 187–196, 2007, doi: 10.1016/j.conengprac.2006.06.001.

JJMIE

Volume 15, Number 5, December. 2021
ISSN 1995-6665
Pages 441 – 449

Jordan Journal of Mechanical and Industrial Engineering

Impact of Abrasive Grit Size and MQL Supply on the Surface Roughness in Belt Grinding of a Case Hardened Steel

Amine Hamdi*, Sidi Mohammed Merghache

Laboratory of mechanical engineering, materials and structures, Faculty of Sciences and Technology, University of El Wancharissi-Tissemsilt, 38000, Algeria

Received April 29 2021 *Accepted October 6 2021*

Abstract

In automotive industries, the belt grinding (BG) is a mechanical manufacturing process by removing material using a tool called an abrasive belt. This technique enables high surface quality and reproducibility of high-precision mechanical parts to be achieved. The main objective of this paper is to provide a detailed account of the effect of superfinishing on the surface texture of 16MC5 casehardened steel by the belt grinding process under the alumina abrasive grains (Al_2O_3) with average sizes (60, 40, 30, 20 and 9 μm), respectively. The surface quality was characterized by one surface roughness parameter (Ra) and three parameters of the Abbott-Firestone curve (Rpk, Rk and Rvk) in order to determine the relationship between the grains size reduction and the surface texture. As all mechanical machining processes with undefined tool geometry (e.g. grinding, polishing, lapping,...etc.), experimental results obtained during measurements suggest a clear relationship between the reduction in abrasive grains size and the surface texture. The minimum quantity lubrication (MQL) also decreases the surface roughness; the lubrication addition helps to achieve better surface quality than the dry belt grinding.

Keywords: Abrasive grains, Belt grinding, Superfinishing, Surface texture;

1. Introduction

The belt grinding process is a machining technology ranked among the superfinishing processes by chip removal. In the automotive industry, it is very important for the superfinishing of automotive engine components subjected to variable (cyclical) requests in time, such as: crankshafts, camshafts, valves ... etc. The texture of its surface is obtained by mechanical action of a cutting tool consisting of a large number of high hardness abrasive grits, randomly between them and the small applied on elastic polyester backing and maintained by a resin. In the socio-economic world, the innovation of this method is to place the machining device on a conventional lathe. Therefore, the significant investments in the machine or even in the level of the infrastructure are not necessary. Over the last decade, abrasive belt grinding has attracted much attention from industry and academia due to the rapid development of abrasive belts [1, 2]. Mezghani et al. [3–5] has also found that this superfinishing process is extensively used in the automotive industry to finish the journals crankshaft. In this research, the authors indicate that the essential goal of belt grinding is to improve surface texture and to increase wear resistance and fatigue life. However, the cutting tool (abrasive belt in this case) is a critical variable that affects the surface quality.

Previous research [6, 7] has shown that the arithmetical mean height parameter of profile *Ra* passes by 0,27 μm to 0,09 μm and the core roughness depth *Rk* passes by 0,9 μm to 0,38 μm if one operates on a bearing steel 100Cr6 (AISI 52100) of 62 HRC hardness for hard turning and belt finishing. The same researcher, but studying the surface roughness of the same hard steel before and after belt finishing in another paper [8], found that the initial arithmetic average of the roughness profile *Ra* = 0,25 μm had been improved to 0,1 μm after belt grinding, reflecting a 60% decrease. In addition, the belt grinding process removes the average width of the roughness profile elements created by hard turning. This constitutes a major benefit in terms of limiting the working surface running-in time. After two belt grinding operations with 30 μm and 9 μm grains, the mean peak spacing parameter *Rsm* decreases significantly, the value of this parameter obtained with the CBN cutting tool by the hard turning is 62,5 μm and becomes 20,5 μm after the belt grinding with the abrasive grit size reduction (30 μm + 9 μm). Furthermore, after both finished abrasive processes, the root mean square (RMS) slopes $R\Delta q$ decreases and oscillates slightly about 4° [9]. Therefore, the abrasive belt machining is considered a flexible and very precise superfinishing method [8–11].

The effect of two-passes belt grinding using abrasive belts with 30 μm and 9 μm grains on the standard 3D surface roughness parameters of hardened steel 41Cr4 with a hardness 57 ± 1 HRC was established by Grzesik et al. [12]. They showed that this machining technique greatly improves the 3D surface roughness parameters for nine seconds of belt grinding with the supply of oil mist provided by a *MQL* system, the surface arithmetic average roughness *Sa* parameter decreases successively from 0,4 μm to 0,04 μm and the maximum surface height *Sz* obtained is 1,33 μm. Minimum quantity lubrication (*MQL*) is currently a

* Corresponding author e-mail: hamdi_amine@ymail.com.

promising alternative to traditional application of fluid coolant [13]. Wang et al. [14] presented a study on the influence of applied force and finishing duration on residual stresses produced during dry belt grinding of bearing parts (AISI52100). When measuring these stresses, the authors observed high compressive residual stresses in the external layer of about 5-10 µm. However, the belt grinding time has no significant effect on the stress distribution and the growing applied force may increase surface circumferential residual stresses marginally, but has an unavoidable impact in the oscillation direction. Simultaneously, Wang et al. [15] investigated the changes produced by dry belt grinding operations on the surface texture of the part and the wear of the abrasive tool. The belt ground material in this work is bearing steel (100Cr6: AISI 52100) with a hardness equal to 62 HRC. The authors indicate that the abrasive grains wear of the cutting tool can be evaluated by three surface roughness parameters (3D: *Sz*, *Sdq* and *Spc*).

In the year 2013, Jourani et al. [16] produced a three-dimensional numerical model (3D) in abrasive belt machining. The abrasive grains made up of the belt-grinding tool are represented by cones of two abrasive papers S20 and S30. The effect of the local geometry of abrasive grains on two machining output variables (friction coefficient (μ) and wear rate (f_{ab})) is studied using this multi-asperity model. During the process, the belt ground surface is represented by a perfectly flat surface and penetrators with different attack angles (abrasive grains) do not deform. The results show a proportional relationship between the output parameters (μ and f_{ab}) and the penetration depth (δ_i). In addition, the same correlation found between the calculated quantities (μ and f_{ab}) and the abrasive grains size (S20 and S30). By the same method and for the same superfinishing process, Jourani [17] developed a three-dimensional model (3D) to study the temperature distribution at the interface abrasive paper/belt ground part. The output variable (T) determined under the effect of the curvature radius (R_i) and the attack angle (α_i) of each abrasive grain. The latter is represented by a cone with a hemispherical tip (R_i). The numerical results indicate a proportional relationship between the output parameter distribution (T) and the both input parameters (R_i and α_i). Recently, Hamdi et al. [18] studied the impact of seven polymer contact rollers (PS-R, POM C-R, PA 6-R, PPC-R, PPH-R, HDPE-R and LDPE-R) on the belt ground surface texture. The latter was characterized by eight roughness parameters (*Ra*, *Rz*, *Rp*, *Rv*, *Rsk*, *Rku*, *Rsm* and *Rdq*) and five parameters of the Abbott-Firestone curve (*Rpk*, *Rk*, *Rvk*, *Mr1* and *Mr2*). The material machined in this experimental study is 16MC5 hardness steel 52 HRC and the abrasive belts used are abrasive grain size 30 µm and 20 µm. After a comparison between the results of seven rollers, the authors indicate that the polyamide roller PA 6 of hardness 60 Shore D gives a better surface texture than that obtained by other rollers of the same hardness or of different hardness. However, optimal medium pressure between the abrasive tool and the belt ground workpiece allows chip removal without fracturing the abrasive grains.

A recent study examined the abrasive belt superfinishing, whereby there are several finishing operations, which are used, in the final stage of manufacture of the high-quality mechanical parts making up the automotive engine in order to reduce the friction between the surfaces, for example, they cited: antifriction coating technology, texturing technology, or more generally, reducing surface roughness [19]. Very recently, the belt grinding has become a very efficient method of superfinishing crankshaft journals and pins to minimize surface peaks, improve geometric efficiency and increase wear resistance and fatigue [19, 20]. Typically, this is achieved by processing three or more belt grinding steps while successfully reducing the size of the grits [19, 20]. There are actually three common superfinishing techniques for abrasive grains, but there are different kinematic techniques: grinding, belt grinding, and belt finishing. The grinding is a very well known operation. The belt is endless in the belt grinding, and the worn grains return still in contact. Moreover, on the belt, no oscillation is applied. On the contrary, fresh grains are continuously inserted into contact in the above application, while worn grains are removed at the same time [21]. Based on a numerical method, Wang et al. [22] proposed a study of geometry interaction between abrasive grains of the belt and workpiece during belt grinding. The results found indicate that the roughness parameter *Ra* is significantly influenced by the belt length and the abrasive wear height, while the cutting depth has an insignificant effect on the same parameter (*Ra*).

However, the studies on the belt grinding under the effect of the abrasives grits size are still lacking. The goal of this paper is therefore to successively investigate the impact of this technique on the belt ground surface texture (five-pass belt grinding). In particular, the surface roughness parameters and the bearing area curve (BAC) parameters were determined.

2. Experimental procedures

2.1. Material, workpiece and tool

The belt grinding operations related to the roughness and bearing area curve parameters were realized on 16MC5 (%C 0,14/0,18) casehardened steel test pieces that are 52 HRC in hardness. The material induction hardening and quenched, quenching is done in oil at a temperature of 860 °C, followed by income to 200 °C. The belt-grinding device on which the superfinishing operations were performed is shown in Figure 1 [18, 23]. The abrasive belts used in the belt grinding tests in this experimental study consist of a flexible backing, resin and a single layer of Al_2O_3 abrasive grains of varying sizes: 60 µm, 40 µm, 30 µm, 20 µm and 9 µm (see Figure 2).

The white ceramics inserts used are square-shaped, removable and fixed by an SNGN 120808 flange that is mounted on a tool holder of CSSNR3225 P12 designation. Cutting parameters used were: cutting speed : Vc = 100 m/min, feed rate : f = 0,1 mm/rev and depth of cut : ap = 0,3 mm.

For each measurement of the belt ground surface texture, a 2D TAYLOR HOBSON profilometer with a 2 µm diamond stylus radius is used. According to the ISO 4288 and ISO 13565 standards, the roughness profiles were carried over an evaluation length equal to Ln = 4,8 mm, a cut-off length was set at 0.8 mm and using a Gaussian filter. An AltiSurf®500 optical metrology unit is also used to improve the visualization of the roughness of the machined surfaces. It allows for a thorough examination of the 3D topography of the belt ground surface texture [23].

The belt grinding conditions which are set during all the tests are shown in Table 1.

3. Experimental results and discussion

3.1. Surface Roughness

In the Figure 3 the variation in the surface quality (Ra) is shown as a function of the reduction in the size of abrasive grits without and with lubrication.

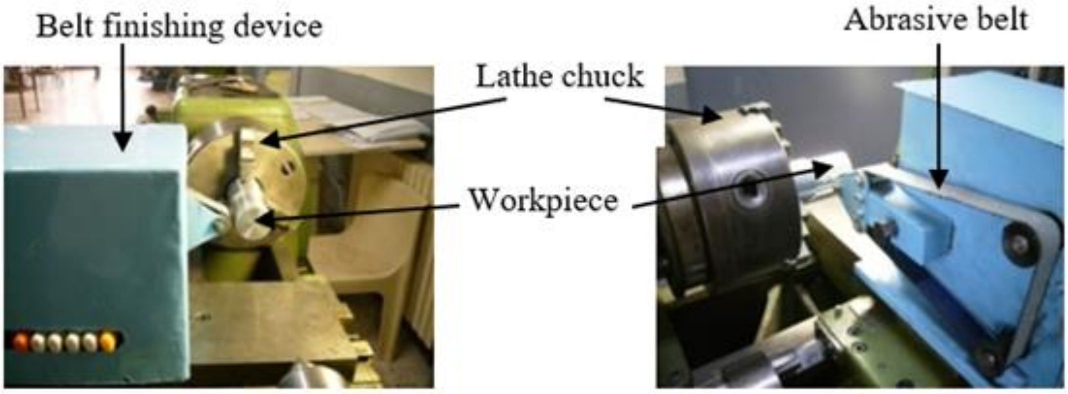

Figure 1. Belt grinding device mounted on a conventional lathe.

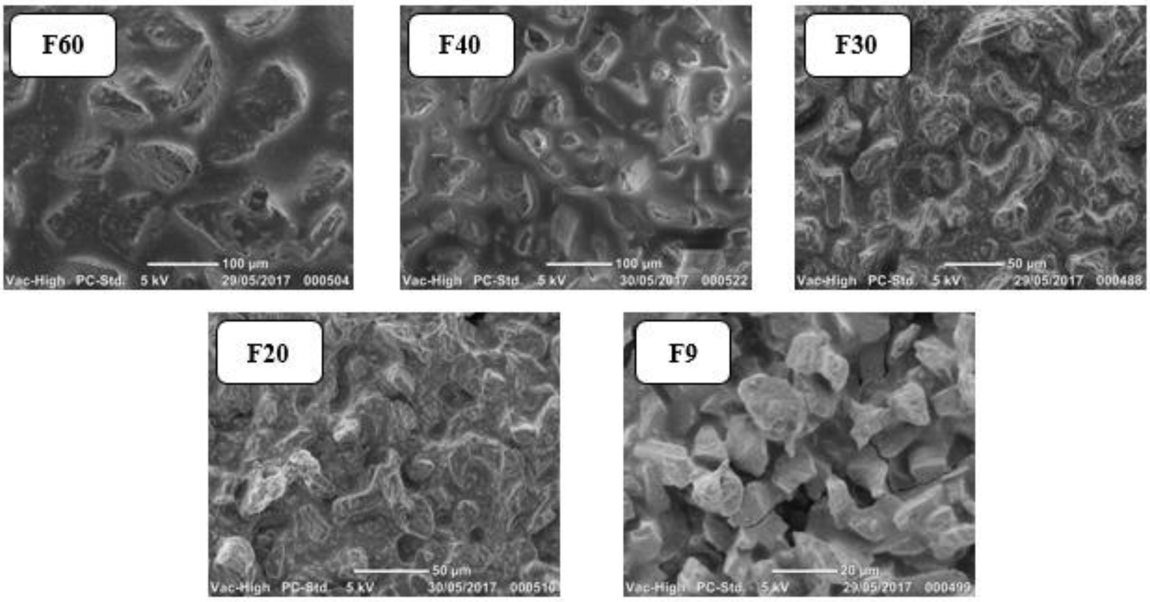

Figure 2. SEM images of new abrasive belts.

Table 1. Belt grinding conditions set during all tests

Working conditions	Value
Rotation speed of the workpiece	900 rev/min
Applied force between belt and workpiece (Fn)	100 N
Belt feed (Va)	44 rev/min
Belt grinding duration ($t_{belt\ grinding}$)	9 s
Oscillation amplitude (a_{osc})	0 mm
Oscillation frequency (n_{osc})	0 mm
Lubrication system (microlubrication: Minimum Quantity Lubrication (MQL))	Oil Tasfalout 22^{M} diluted to 1/10. The mineral oil flow rate is 60 ml/h and injected at very high velocity (80 m/s). A single nozzle is oriented between the workpiece and the abrasive belt (cutting zone).

From this Figure 3, surface state represented by the arithmetic average of roughness profile *Ra*improves progressively when the abrasive grits size decreases. This explains why the roughness of the hard steel surface tends to decrease under the effect of grits size. Both profile roughness parameters of the hard turning are: *Ra* = 0,781 µm and after belt grinding without lubrication up to the abrasive grits size 9 µm, they decrease: *Ra* = 0,049 µm, which represents a reduction of about 94 %. Concerning the second case with lubrication, they are much better: *Ra* = 0,020 µm, which represents a reduction of about 97 %, for the same grits size (9 µm). The *Ra* parameter is less than 1 µm in both cases of belt grinding, which meets the surface quality criterion of high precision machining [24].

The equations adopted in this analysis are linear in shape since they have the uppermost coefficients of determination (denoted R^2). So, the linear regression equation of the arithmetic average of roughness profile (Ra) with lubrication is given by formula (1) and without lubrication is expressed by formula (2). The value of the coefficient of determination (R^2) is 98,1%, 98,6%, respectively.

$$Ra_{\text{With lubrication}} = 0{,}009\text{Gs} - 0{,}087 \quad (R^2 = 0{,}981) \qquad (1)$$

$$Ra_{\text{Without lubrication}} = 0{,}011\text{Gs} - 0{,}07 \quad (R^2 = 0{,}986) \qquad (2)$$

Thus, it can be noted in Figure 4, that the peaks of the belt grinding of abrasive grains size reduction with or without lubrication are distinctly low compared to the peaks of hard turning. Indeed, this finding can be explained by the fact that the contact surface between the grits and the finished surface is larger during the belt grinding by large grits, so the grits eliminate more macro-geometric defects and prepare the surface in the next step, mean or fine grits. However, finer grits in contact with the surface constitute a smaller contact surface and thus remove more micro-geometrical defects. The roughness decreases proportionately with the reduction in the size of abrasive grits, suggesting a correlation between surface quality and grain size. This phenomenon of the belt grinding process is similar to the work of Belkhir et al. [25] which relates to optical glass polishing. This observation is confirmed further by Figure 5, compared with the second case without lubrication, the peaks obtained by belt grinding decreasing the size of abrasive grains (up to 9 µm) with lubrication are higher. Therefore, this approach helps the process to clip the peaks of the roughness leash, which greatly improves the final surface of the hard steel.

Comparing our results with others obtained by a finishing process of the same principle and commonly used in the automotive industry (grinding), we take for example, the results of a recent research by Grzesik et al. [26]. These researchers rectified a 41Cr4 (AISI 5140 equivalent) steel of hardness 57 ± 1 HRC by a conventional cylindrical grinder using mono-crystalline aloxite Al_2O_3 wheel with 5 passes plus spark-out. The obtained roughness parameter *Ra* was about 0,3 µm and the other *Rz* was 2,4 µm. Therefore, this last parameter is superior to 1 µm (high-precision machining surface quality criterion with *Rz* < 1 µm), although is close to the precision machining interval with *Rz* = 2,5-4 µm [12, 24–27].

Kenda et al. [27] studied the effect of the abrasive flow machining (AFM) process parameters on the surface integrity of the hardness 59 HRC heat treated tool steel AlS1 D2 in recent polishing process. By electrical discharge machining operation (EDM), the initial state of the parts was obtained. They measured the roughness before and after the abrasive flow machining in two directions (along and transverse). According to this study, the lower roughness (*Ra*, *Rz* and *Rt*) are obtained for the direction of longitudinal measurement to the workpiece and the maximum pressure (6.0 MPa). The reduction ratio of the arithmetic average of roughness profile is about 86 per cent. In this comparison, the reduction ratio of Ra of belt grinding with lubrication is about 97 per cent.

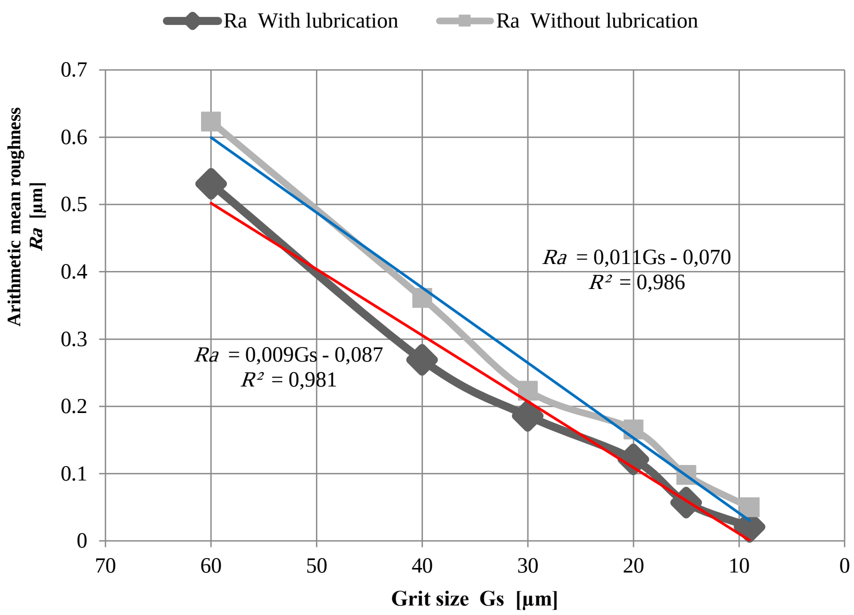

Figure 3. Ra generated by the belt grinding process without and with lubrication under abrasive grit size reduction.

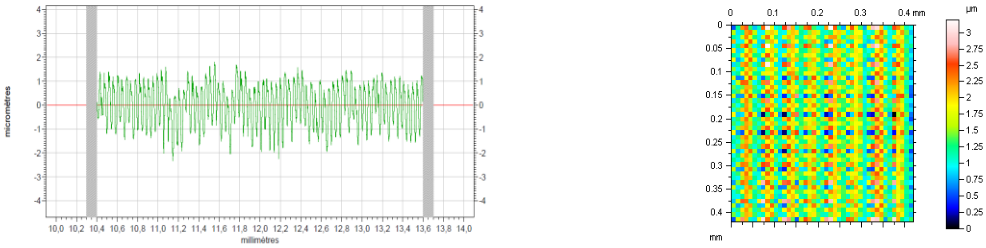

(a) After hard turning (HT)

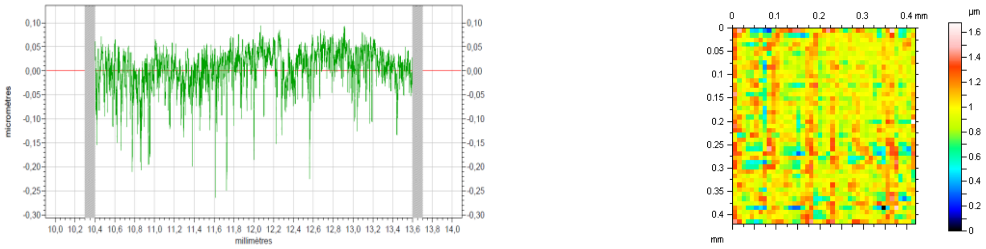

(b) Grains size: 60 µm + 40 µm + 30 µm + 20 µm + 9 µm

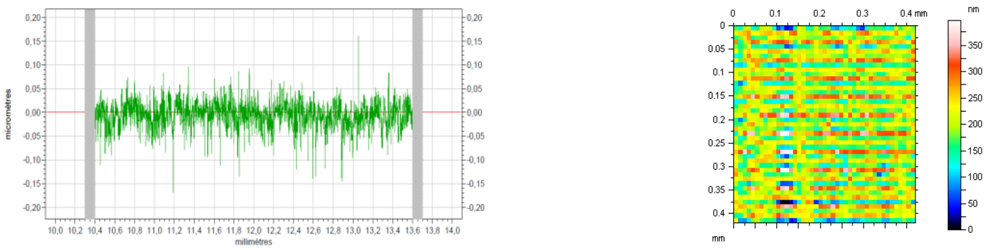

(c) Grains size: 60 µm + 40 µm + 30 µm + 20 µm + 9 µm

Figure 4. Surface profiles generated by: (a) after hard turning, (b) successful belt grinding without lubrication, (c) successful belt grinding with lubrication.

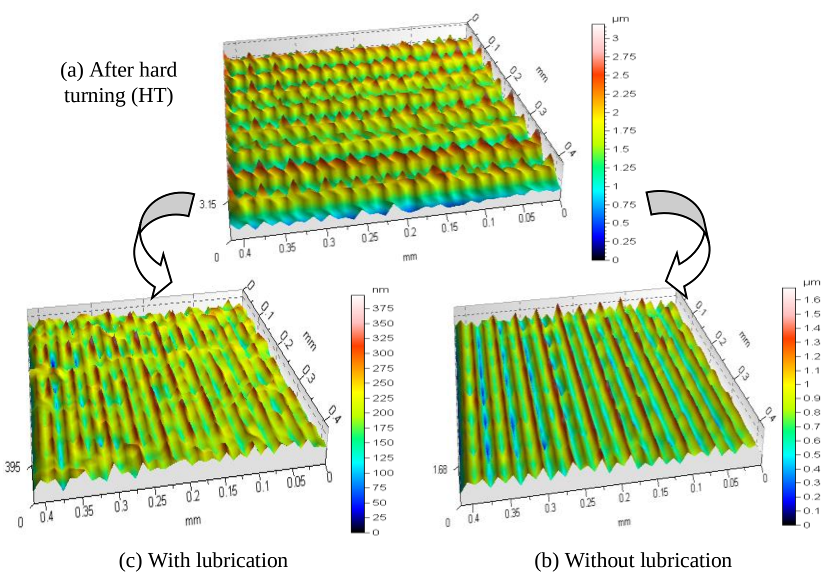

Figure 5. Surface topography 3D generated by successive belt grinding (up to 9 µm) without and with lubrication.

This process does not make it possible to eliminate the extra thickness such as the extra thickness from grinding. The belt finishing does not introduce heating only over a small number of asperity peaks and the contact temperatures distribution increases with the abrasive grains size [28], contrary to the grinding, which induces a modification of the microstructure of the surface layer of part. Moreover, contrary to ground surfaces, the characteristics of superfine surfaces are completely constant, as well on the part itself as in all the parts of a series.

This comparison clearly shows that belt ground surfaces are best compared to ground surfaces or obtained with abrasive flow machining. In addition, the technique of superfinishing by abrasive belt induces compressive residual stresses in a very thin sublayer of around 5-10 µm according to the previous study by Rech et al. [21]. By this great improvement in surface roughness and compressive residual stresses, the belt grinding process greatly improves the surface integrity, which positively influences fatigue strength and improves service life of the mechanical parts.

Finally, after this section, we can notice that the high-precision finishing process by belt grinding attacks the hollow profile crests of hard turning which resists little wear and gives a full profile that is more resistant to wear. The surface integrity can not only be completely changed during the application of lubricated belt grinding process, but also improved compared to dry finish turning (hard turning) as reported by Courbon et al. [29]. In a study of dry hard turning of AISI D3 steel of hardness 62 HRC, Bhemuni and Rao Chalamalasetti[30] used central composite design (CCD) to perform experimental testing and response surface methodology (RSM) to model Ra roughness. The best roughness found is 0.561 µm by the following cutting parameters: Vc = 165 m/min, f = 0,05 mm/rev et ap = 0,3 mm. In their conclusion, the author indicates that the roughness found is close to that obtained in grinding. Sureshchandra Maheshwari and Ratnakar Gawande [31] studied the improvement of surface quality of AA 6351 by the stiff burnishing process. The previous methods (CCD + RSM) are used to do the experimental part and the second digital part. The best roughness found is: Ra = 0,057 µm. So, after this comparison, the belt grinding remains the most effective technique in order to obtain a better surface quality.

3.2. Bearing ratio parameters

Nowadays, characterization of the belt ground surface texture affected by the ISO 13565 standard takes an important place by the automotive industry; this method based on analysis of the material/bearing ratio curve (or Abbott-Firestone curve) parameters of roughness profiles. According to Hamdi et al. [32], the surface functionality can be described by the parameters of the bearing ratio curve (Rpk, Rk and Rvk), plus other roughness parameters (like for example: Ra, Rt, Rsm, ... etc.). The following Figures 6–7 shows the variation of various parameters from bearing area of belt grinding depending to grits size reduction.

These parameters are determined from the bearing ratio curve by integrating the distribution of height over the whole surface. They are shown of particular interest to characterize the surface texture [19]. According to Figure 6, we note that the three curves (Rpk, Rk and Rvk) represent almost the same trend; there is proportionality between the three parameters and the abrasive grits size reduction. The final reduced peak height Rpk of belt grinding with lubrication to the grits size up to 9 µm is about 96 per cent less than the initial Rpk and without lubrication is about 94 per cent, which transmit a percentage of 4 per cent of the asperities to remove during the first hours of honing operation (Rpk represents the material portion in the vicinity of peaks being removed during sliding interactions. So, the running-in period can be shortened as much as possible [33]). The final kernal roughness depth (or core roughness depth) parameter Rk is about 96 per cent less than the initial and 95 per cent for dry belt grinding, it represents the material quantity available for wear to the engine life. In regards to, the third parameter (reduced valley depth) Rvk, it is less than the initial state of a percentage of about 93 per cent and 88 per cent of dry belt grinding, leaving 7 per cent of those who will never be worn to retain the lubricant required for proper functioning. Khellouki et al. [6] studied via a design of experiments, the effects and the interactions of the belt finishing parameters on the surface state of AISI 52100 bearing steel. It's have shown that the belt finishing improves considerably the surface bearing curve parameters (Rk pass by 0,9 µm to 0,38 µm, Rpk pass by 0,35 µm to 0,12 µm and Rvk pass by 0,12 µm to 0,15 µm).

The formula of the reduced peaks height *Rpk* with lubrication is given by formula (3) and without lubrication is given by formula (4). The value of the coefficient of determination (R^2) of these formulas is equal to 98,5%, 98,5%, respectively.

$$Rpk_{\text{With lubrication}} = 0{,}009Gs - 0{,}055 \quad (R^2 = 0{,}985) \tag{3}$$

$$Rpk_{\text{Without lubrication}} = 0{,}011Gs - 0{,}04 \quad (R^2 = 0{,}985) \tag{4}$$

The linear regression equation of core roughness depth *Rk* with lubrication is given by formula (5) and without lubrication is given by formula (6). The coefficient of determination (R^2) is 97,8%, 99,1%, respectively.

$$Rk_{\text{With lubrication}} = 0{,}032Gs - 0{,}272 \quad (R^2 = 0{,}978) \tag{5}$$

$$Rk_{\text{Without lubrication}} = 0{,}035\ Gs - 0{,}22 \quad (R^2 = 0{,}991) \tag{6}$$

The linear equation of reduced valley depth *Rvk* with lubrication is given by formula (7) and without lubrication is given by formula (8). The coefficient of determination (R^2) of these formulas is equal to 97,2%, 97,8%, respectively.

$$R_{vk\ \text{With lubrication}} = 0{,}01Gs - 0{,}004 \quad (R^2 = 0{,}972) \tag{7}$$

$$R_{vk\ \text{Without lubrication}} = 0{,}011Gs - 0{,}024 \quad (R^2 = 0{,}978) \tag{8}$$

Table 2 gives a comparison between three parameters of the material ratio curve (*Rpk*, *Rk* and *Rvk*) in terms of percentages left by the belt grinding process with the minimum quantity lubrication (*MQL*).

Table 2. Percentage of three parameters (*Rpk*, *Rk* and *Rvk*) generated by the belt grinding process with *MQL*

Parameters	Percentage [%]	Remarks
Rpk	4	Low: Good to reduce running-in time and wear
Rk	4	Low: Good to reduce oil consumption
Rvk	7	Great: Good for feeding, circulation and storage of oil

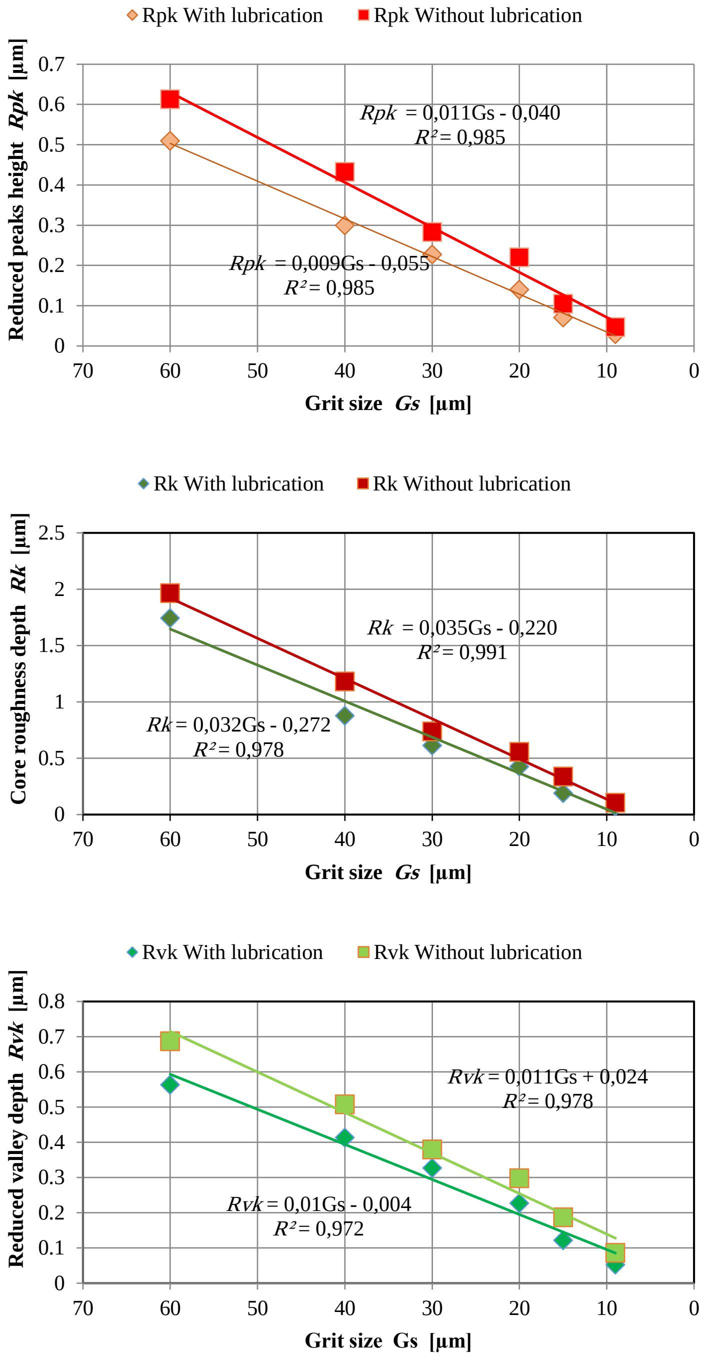

Figure 6. Settings the bearing area curve (*Rpk*, *Rk* and *Rvk*) of belt grinding according to grits size reduction.

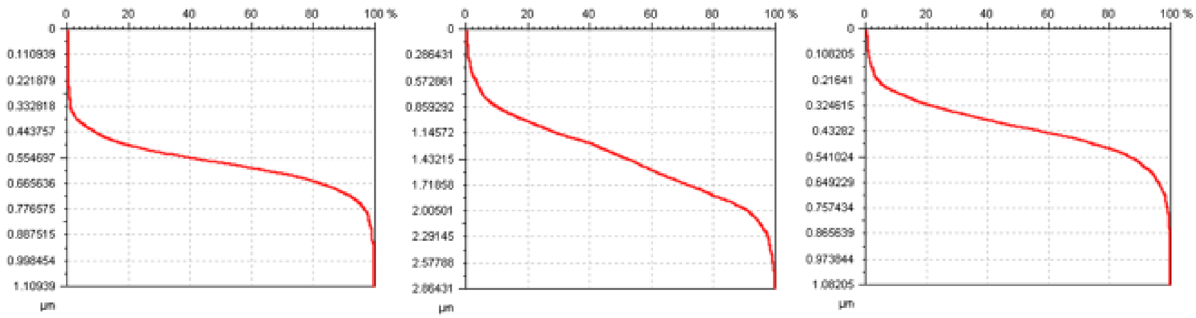

(b) After BG without lubrication. (a) After hard turning. (c) After BG with lubrication.

Figure 7. Material ratio curve (BAC) of successful belt grinding (BG) with and without lubrication: up to 9 µm.

About the equivalent straight line of the bearing ratio curve (Figure 7) is very significant because it is related to the wear rate of the surface, see that the equivalent slope of the two cases of successful belt grinding is lower than for hard turning (the curve obtained by hard turning falls rapidly: Figure 7.a) and successful belt grinding with minimum quantity lubrication is lower relative to the dry belt grinding (see that the curve is relatively a horizontal line in its intermediate part; Figure7.c), confirming that the belt ground surface obtained with lubrication having an almost perfect shape tray, so the engine runs long. In comparison with the work of Khellouki et al. [8], on bearing steel 100Cr6 (AISI 52100) tempered at 62 HRC as a function of the increase in applied force, they found that the slope of the bearing area curve reduced and the peaks are decreased. Thus, the belt finishing surface approaches the configuration which characterizes a 'plateau' surface. This kind of surface is required for its good bearing properties. Jourani et al. [34] presented a three-dimensional numerical model (3D) of belt grinding and showed that both processes (hard turning (HT) or belt grinding (BG)) improve the surface texture and more in particular, the bearing area curve (BAC).

4. Conclusion

In this work, the impact of the reduction in the abrasive grain size during belt grinding on the surface texture of 16MC4 casehardened steel is studied here. It can be inferred from the outcome of our research that the belt grinding process can be used in practice effectively and the reduction in the size of abrasive grains is proportional to the improvement of the surface texture. This process makes it possible to achieve a very low roughness on the surface of a workpiece and a "polished mirror" state in the range of several micrometers up to a few tens of nanometers. The roughness of the order has been found: Ra = 0,02 µm and Rz = 0,24 µm. So, the belt grinding enables a glossy surface to be obtained, the roughness to be reduced and the required precision to be formed. Finally, the belt grinding of the abrasive grains size reduction with minimum quantity lubrication (*MQL*) is a promising finishing process and increases its effectiveness. In some cases and according to the application, dry belt grinding is also feasible.

Acknowledgement

This research was supported by the Mechanical Engineering, Materials and Structures Laboratory approved in 2020 by Ministerial Order N° 05 on 18 February 2020, a laboratory of excellence at the University of Tissemsilt, General Directorate of Scientific Research and Technological Development (DGRSDT), Ministry of Higher Education and Scientific Research, ALGERIA.

Appendix

Symbols	Description
Ra	Arithmetic average of roughness profile
Rz	Maximum height of the profile
Rpk	Reduced peak height
Rk	Core roughness depth
Rvk	Reduced valley depth
Rsm	Mean spacing of the profile elements
$R\Delta q$	Root mean square (RMS) slopes
Sa	Arithmetic mean roughness of the surface
Sz	Maximum surface height
μ	Friction coefficient
f_{ab}	Wear rate
δ_i	Penetration depth
R_i	Curvature radius
α_i	Attack angle
Rp	Maximum profile peak height
Rv	Maximum profile valley depth
Rsk	Asymmetry factor (Skewness)
Rku	Sharpness factor (Kurtosis)
Mr1	Material portion corresponding to the upper limit position of the roughness core profile (material portion 1)
Mr2	Material portioncorresponding to the lower limit position of the roughness core profile (material portion 2)
Vc	Cutting speed
f	Feed rate
ap	Depth of cut
Ln	Evaluation length
R^2	Coefficient of determination

References

[1] C. Cheng, J. Li, Y. Liu, M. Nie and W. Wang, "An online belt wear monitoring method for abrasive belt grinding under varying grinding parameters,"*Journal of Manufacturing Processes 50*, pp.80–89, 2020.

[2] C. Cheng, J. Li, Y. Liu, M. Nie and W. Wang,"Deep convolutional neural network-based in-process tool condition monitoring in abrasive belt grinding,"*Computers in Industry 106*, pp.1–13, 2019.

[3] S. Mezghani and M. El Mansori,"Abrasiveness properties assessment of coated abrasives for precision belt grinding,"*Surface & Coatings Technology 203*, pp.786–789, 2008a.

[4] S. Mezghani, M. El Mansori, A. Massaq and P. Ghidossi,"Correlation between surface topography and tribological mechanisms of the belt-finishing process using multiscale finishing process signature,"*C. R. Mecanique 336*, pp.794–799, 2008b.

[5] S. Mezghani, E. Sura and M. El Mansori, "The effect of belt-finishing process variables on the topography of finished surfaces,"*Trib. Trans, 51(4)*, pp.1-9, 2008c.

[6] A. Khellouki, H. Maiz, J. Rech and H. Zahouani,"Application of the method of design of experiments to characterize the belt finishing process,"*–4th International Conference 'Integrated Design and production*, Casablanca, Morocco, 2005.

[7] A. Khellouki, H. Maiz, J. Rech and H. Zahouani,"The effect

of abrasive grain's wear and contact conditions on surface texture in belt finishing,"*Wear 263*, pp.81–87, 2007a.

[8] A. Khellouki, H. Maiz, J. Rech and H. Zahouani,"Influence of the belt-finishing process on the surface texture obtained by hard turning,"*Proceedings of the Institution of Mechanical Engineers Part B Journal of Engineering Manufacture 221 (7)*, pp.1129-1137, 2007b.

[9] W. Grzesik, J. Rech and T. Wanat,"Surface integrity on hardened steel parts produced by hybrid machining sequences,"*Journal of Achievements in Materials and Manufacturing Engineering*, Vol. 31, no. 2, pp.654–661, 2008.

[10] W. Grzesik, J. Rech and T. Wanat, "Surface finish on hardened bearing steel parts produced by superhard and abrasive tools,"*Int J Mach Tool Manu 47(2)*: pp.255–262, 2007.

[11] L. Zou, X. Liu, Y. Huang and Y. Fei,"A numerical approach to predict the machined surface topography of abrasive belt flexible grinding," *Int J Adv Manuf Technol 104*, pp. 2961–2970, 2019.

[12] W. Grzesik, J. Rech and K. Żak,"High-Precision Finishing Hard Steel Surfaces Using Cutting, Abrasive and Burnishing Operations,"*Procedia Manufacturing*, Vol. 1, pp.619–627, 2015a.

[13] M. M. Rahman and K. Kadirgama,"Material removal rate and surface roughness on grinding of ductile cast iron using minimum quantity lubrication,"*International Journal of Automotive and Mechanical Engineering (IJAME)*, Vol. 11, pp.2471-2483, 2015.

[14] W. Wang, F. Salvatore and J. Rech,"Characteristic assessment and analysis of residual stresses generated by dry belt finishing on hard turned AISI52100,"*Journal of Manufacturing Processes 59*, pp.11–18, 2020.

[15] W. Wang, F. Salvatore, J. Rech and J. Li,"Comprehensive investigation on mechanisms of dry belt grinding on AISI52100 hardened steel,"*Tribology International 121*, pp.310–320, 2018.

[16] A. Jourani, B. Hagège, S. Bouvier, M. Bigerelle and H. Zahouani,"Influence of abrasive grain geometry on friction coefficient and wear rate in belt finishing,"*Tribology International 59*, pp.30–37, 2013.

[17] A. Jourani, "Three dimensional modelling of temperature distribution during belt finishing,"*Int. J. Surface Science and Engineering*, Vol. 9, No. 2/3, pp.231–246, 2015.

[18] A. Hamdi, S.M. Merghache, B. Fernini and T. Aliouane, "Influence of polymer contacting rollers on surface texture finish in the belt grinding process,"*Int J Adv Manuf Technol 113*, pp.1377–1388, 2021.

[19] K. Serpin, S. Mezghani and M. El Mansori,"Multiscale assessment of structured coated abrasive grits in belt finishing process,"*Wear 332-333*, pp.780–787, 2015a.

[20] K. Serpin, S. Mezghani and M. El Mansori,"Wear study of structured coated belts in advanced abrasive belt finishing,"*Surface & Coatings Technology 284*, pp.365–376, 2015b.

[21] J. Rech, G. Kermouche, W. Grzesik, C. Garcia-Rosales, A. Khellouki and V. Garcia-Navas, "Characterization and modelling of the residual stresses induced by belt finishing on a AISI52100 hardened steel,"*Journal of materials processing technology 208*, pp.187-195, 2008.

[22] W. Wang, J. Li and W. Fan, "A numerical approach to analyze ground surface texture based on abrasive belt topography,"*Proceedings of Asia International Conference on Tribology*, pp.193–195, 2018.

[23] A. Hamdi, T. Aliouane and D. Bouzid,"Technological Parameters of belt grinding process of hard steel,"*Mechanics and Mechanical Engineering*, Vol. 21, no. 4, pp.843–853, 2017.

[24] W. Grzesik, K. Żak and P. Kiszka,"Comparison of surface textures generated in hard turning and grinding operations,"*Procedia CIRP 13*, pp.84–89, 2014.

[25] N. Belkhir, D. Bouzid and V. Herold,"Correlation between the surface quality and the abrasive grains wear in optical glass lapping,"*Tribology International 40*, pp.498–502, 2007.

[26] W. Grzesik, J. Rech and K. Żak,"Characterization of surface textures generated on hardened steel parts in high-precision machining operations,"*Int J Adv Manuf Technol 78*, pp.2049–2056, 2015b.

[27] J. Kenda, G. Kermouche, F. Dumont, J. Rech and J. Kopac,"Investigation of the surface integrity induced by abrasive flow machining on AISI D2 hardened steel,"*Int. J. Materials and Product Technology*, Vol. 46, no. 1, pp.19–31, 2013.

[28] A. Jourani, "Three dimensional modelling of temperature distribution during belt finishing,"*Int. J. Surface Science and Engineering*, Vol. 9, No. 2/3, pp.231–246, 2015.

[29] C. Courbon, C.F. Valiorgue, C. Claudin, M. Jacquier, F. Dumont and J. Rech, "Influence of some superfinishing processes on surface integrity in automotive industry,"*Procedia CIRP 45*, pp.99–102, 2016.

[30] V. Bhemuni and S. Rao Chalamalasetti, "Statistical Model for Surface Roughness in Hard Turning of AISI D3 Steel,"*Jordan Journal of Mechanical and Industrial Engineering*,Volume 8, Number 6, pp. 393–401,2014.

[31] A. Sureshchandra Maheshwari and R. Ratnakar Gawande, "Improving Surface Quality of AA 6351 by the Stiff Burnishing Technique,"*Jordan Journal of Mechanical and Industrial Engineering*, Volume 10, Number 4,pp. 245–251, 2016.

[32] A. Hamdi, S.M. Merghache and T. Aliouane,"Effect of cutting variables on bearing area curve parameters (BAC-P) during hard turning process,"*Archive of Mechanical Engineering*, 67(1): pp.73–95, 2020.

[33] W. Grzesik and K. Żak,"Modification of surface finish produced by hard turning using superfinishing and burnishing operations,"*Journal of Materials Processing Technology 212*, pp.315–322, 2012.

[34] A. Jourani, M. Dursapt, H. Hamdi,J. Rech and H. Zahouani,"Effect of the belt grinding on the surface texture: Modeling of the contact and abrasive wear,"*Wear 259*, pp.1137–1143, 2005.

JJMIE

Volume 15, Number 5, December. 2021
ISSN 1995-6665
Pages 451 – 460

Jordan Journal of Mechanical and Industrial Engineering

The Analysis of Particle Size Effect on Performance of WC/Cu P/M Compact Sintered Electrode in EDM Process

R.V.S.Subrahmanyam[*1], Koona Ramji[2], Pujari Srinivasa Rao[3], ChundruVenkata Rao[4]

[1, 2, 4] *Department of Mechanical Engineering, Andhra University, Visakhapatnam, India*

[3]*Department of Mechanical Engineering, GITAM, Visakhapatnam, India*

Received April 17 2021 *Accepted October 29 2021*

Abstract

The main aim of this study is to evaluate the influence of particle size variations on electric discharge machining (EDM) electrodes made with a combination of Tungsten carbide (WC) and Copper (Cu) powders using the powder metallurgy (P/M) method. The electrodes are in cylindrical shape of 15 mm diameter and are made with following sizes i.e., Nano Particles (NP), a mix of Nano and Micron Particles (NMP) and Micron Particles (MP). Electrodes, thus made in combinations were used to study the performance during surface modification of Inconel 718 alloy using EDM. The electrodes were made with wt% 40, 50& 60 of WC and the rest is Cu, whereas the compaction ranges 200-400Mpa. Among the unconventional machining processes, EDM is the most preferred surface modification process to machine very hard materials like Inconel 718 alloy. Machining was conducted by varying parameters viz., pulse on time, polarity, peak current, %WC in tool composition, Particle size, and compaction pressure. The performance indicators in the present investigation are material removal rate (MRR) and tool wear rate (TWR). The results were analyzed using MINITAB 14 software, and it was noted that the improvement in MRR was due to the influence of particle size and peak current. A highest MRR of 9.90 mg/min was attained with NP electrode and a peak current of 13A. The highest TWR of 20.70 mg/min was also observed at the machining condition where highest MRR was observed. The results of the MRR and TWR values show the significant influence of all the six process variables on EDM process.

Keywords: EDM, WC- Cu, P/M compact sintered electrode, MRR, TWR, Inconel 718;

1. Introduction

Inconel 718 is a super alloy of nickel, chromium and molybdenum combination. It is an excellent property of high yield tensile, creep rupture and oxidation resistance at high temperatures. It can resist the pitting and fracture corrosive environments strictly [1-2]. Application of Inconel 718 in industry is numerous. From the aviation to chemical industry, this alloy is widely used due to its superior properties vis-à-vis non-corrosive and fatigue-resistant nature, and creep resistance. Conventional machining process falls short at increased temperatures owning to high strength of Inconel 718, low elastic modulus and thermal conductivity. Thermoelectric process done by EDM due to the process a series of discrete sparks between work piece and tool, both submerged in a dielectric fluid with elimination of the mechanical stress, chatter, and vibration during machining as there is no direct contact between the electrode and the work piece [3]. In general, Copper and copper alloys, Tungsten, graphite, zinc and brass used in making these EDM electrodes have both plus, and minus advantages. Researchers had to spend a good time in producing a composite electrode with combinations of various materials using power metallurgy (P/M) technique. Alloys of most metals and nonmetals of intricate shapes can be manufactured by Powder Metallurgy method [4]. It is important to note that the tool electrodes produce through P/M technique are one among the least expensive. Because of the cited reasons, electrodes thus produced are useful for machining materials like Inconel 718, a difficult machinable alloy.

Genichi Taguchi, an expert and renowned quality engineer in Japan also considered, "father of quality engineering [5], categorized quality as quality control checked through off-line and on-line. Together are cost effective to their respective domains based on the decisions taken. The first one; is the quality control which is an off-line talk about the improvement in quality within the product and process development stages, whereas the second one is an On-line quality control that refers to monitoring of the running manufacturing processes for verification of the quality levels produced [6]. Although the Taguchi method has limitations, it has effectively solved single response problems [7].

The P/M electrode's particle size has a predominant effect among the electrode parameters on the performance of the EDM and properties of EDMed workpiece[8]. The particle size used (on an average) in the earlier research was Li et al., 23µm of W-Cu [9], Das and Misra 44µm of TiC-

* Corresponding author e-mail: rvss1961@gmail.com.

Cu [10], Cogun et al., 70 µm of Cu-B_4C [3], Bai and Koo 15 µm Al-Mo [11]. Venkata Rao et.al 20-40 nm & 30-50 µm of TiC and Cu [12].From the literature, most of the P/M electrodes were done by micron particle size with a small variation in microns. Liquid phase sintering is governed by the fine size of particle [7]. The surface roughness of the EDMed surface machined with composite electrode is higher when compared to distinct solid material [8] and the value of roughness was rising in proportion to the increase in the P/M electrode particle size. Corner wear can also be minimized by selecting small particle size that has high strength and density. In addition to that, the particle size of the composite electrode is another important factor that greatly affects the EDM's process stability [9]. Process stability is highly sensitive to changes in particle size. It is known that for improved machining efficiency, it is essential to enhance process stability. From the above discussion, it is evident that particle size has a major influence on both the attributes of EDMed surface and stability of the process, hence preferred particle size to be as small as possible.

The existing literature is concentrated on composite electrodes made with micron-size powders and none of the work is reported on electrodes made with nano size powders, as per the awareness of the author. In the present investigation, the performance of WC/Cu electrode made with nano-material is compared with the micron-sized composite electrode, and the material used for machining is Inconel 718 alloy.

2. Experimental Methods and Materials

The electrodes are fabricated by varying the WC powders in percentages by weight of 40, 50 and 60 and rest of with Cu powder. The high hardness of WC powder (about 9.0-9.5 Mohs) and its melting point of 2870°C were utilized in the present investigation. In addition, the high thermal and electrical conductivity of Cu and its binding ability throughout compaction were also the reasons for using the same. They were compacted from 200 to 400 MPa using a Carver model compaction machine. The P/M electrode was attached to a metallic copper with glue, while Inconel 718 alloy with Φ20 mm and 10 mm thick cylindrical-shaped was used as the workpiece. The workpiece composition and properties are presented in Table 1. The factors and their levels are shown in Table 2.

Mixed Orthogonal Array (OA) of size L18 (2^1 x 3^5) with six parameters was selected and experiments conducted where in 2-level parameter is one, and 3-level parameters are five. The parameters pertaining to tool and process namely polarity, peak current, pulse on-time, size of particle, %WC in WC/Cu tool and pressure of compaction were preferred for the study and details placed in the Table 2. Die Sinking EDM (Sparkonix S25) was used for experiments and the EDM Oil is the dielectric fluid. Lateral flushing with a pressure of 0.5 Pa was maintained during the experiments. Figure 1 shows the machining set up which consists of workpiece, work clamping set-up and electrode (tool). The tool tip of the EDM is the exact replica of the shape to be produced on the workpiece.

Scanning electron microscope (SEM) and X-ray diffraction (XRD) were utilized for extraction of Images from the samples of experiment. The received machined workpiece material is extracted from SEM images, whereas for identification of inter-metallic phases generated during machining, the X-pert pro Material Research Diffraction (MRD) was used. In this work, the material's loss in weight per time after machining was used to obtain each of MRR and TWR. After machining, the results were used to generate models, which identify the main effects. Using these models, the general behavior of the electrode in conjunction with the machining parameters is presented in the following sections.

Table 1. As received EDMed workpiece of Inconel 718alloy chemical composition

	Ni	Fe	Cr	C	Cu	Nb	O	Mo	Ti	Al
Elements	42.2	17.2	16.4	12.5	0.27	4.0	3.03	3.0	0.9	0.5

Table 2. Experimental parameters and their levels

Parameters		Symbol	Level1	Level 2	Level 3
A:	Polarity	POL	Positive (P)	Negative (N)	---
B:	Peak current (Amp)	IP	7	10	13
C:	Pulse on-time (µsec)	TON	4	8	12
D:	Particle size	PS	NP	NMP	MP
E:	% WC in WC/Cu tool	%WC	40	50	60
F:	Compaction Pressure(MPa)	CP	200	300	400

2.1. Electrodes (WC/Cu) Fabrication

Electrodes were made by mixing the powders (99.5%) of electrolytic copper (Cu) and titanium carbide (WC) in proportionate ratios of weight as per Table 3. Electrode particle sizes vary from 20-40nm and 30-50nm for nano and micron sizes referred to as Nano(NP) and Micro(MP) electrodes. The NMP electrode is made by blending of nano and micron powders in equal weight proportions. Powder and Liquid wax, which is the binder, are mixed by the Mortar and Pestle process. Liquid Wax comprises 1/100th of the weight of the mixture. Mixing is carried out for half an hour, after which compacting is carried out at pressures of 200, 300 and 400 MPa. For the current application, the dimensions of the die are Φ15mm and length 50mm. The entire operation was carried out on a 200 Ton Universal C.T. machine.

Sintering of the compacts is carried out in a vacuum furnace by varying the temperature linearly (@ 5^0C/min) up to 350^0 C and maintained at the temperature for a 60-minute duration. Subsequently the temperature is raised ramp of 10^0C/min to 950^0C and held for one hour in Argon filled environment as shown in Figure 2. Cracking is avoided by cooling the components for 4½ hrs at a constant rate of 5^0C/min. An adhesive with good electrical properties is utilized to join the Electrodes to brass rods of size ø12mm and length 50 mm.

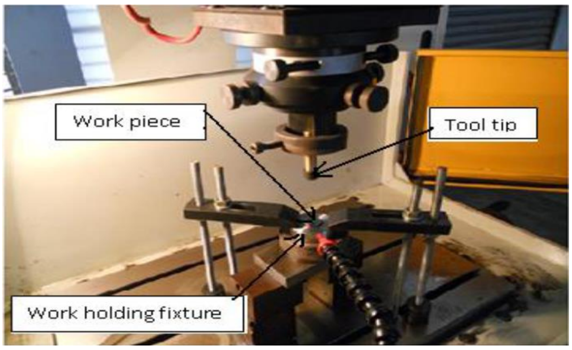

Figure 1. Sparkonix S25 Model Die sinking EDM Machine and experimental setup

Table 3. Tool electrodes and their composition in weight percentages

Electrode	NP (Both)	NMP (Each 50%)	MP (Both)
P/M processed sintered WC/Cu electrode - 1	WC40%Cu60%	WC(20+20)%Cu(30+30)%	WC40%Cu60%
P/M processed sintered WC/Cu electrode - 2	WC50%Cu50%	WC(25+25)%Cu(25+25)%	WC50%Cu50%
P/M processed sintered WC/Cu electrode - 3	WC60%Cu40%	WC(30+30)%Cu(20+20)%	WC60%Cu40%

3. Results and Discussion

Taguchi's method was used to optimize settings of parameter for MRR and TWR with the analysis of Signal to Noise (S/N) ratio. The logarithmic transformation of Loss function is evaluated. The parameters selected for MRR and TWR would be 'Higher' and 'Lower' respectively for better performance as mentioned in Equation 1 and 2.

The ratio of S to N for Material Removal Rate

$$\eta = -10 \log\left(\frac{1}{n}\sum_{i=1}^{n}\frac{1}{y_i^2}\right) \quad (1)$$

S/N ratio for Tool wear rate

$$\eta = -10 \log\left(\frac{1}{n}\sum_{i=1}^{n} y_i^2\right) \quad (2)$$

'y'is the responses measured individually
'n' is the measurement sample in numbers

The experimental results of MRR and TWR with varying values of S/N are indicated in Table 4. At each level of experimental data, taking all the six parameters into consideration Mean S/N ratio is evaluated for MRR and TWR and tabulated in Tables 5 & 6 respectively. The variation between the lowest and highest value of S/N is indicated by Delta. Better performance is said to have been achieved with higher value of S/N and is termed as optimal level. Each parameter with its optimal levels can be seen for both MRR and TWR in Figures 3 & 4 respectively. In order to arrive for better MRR and TWR, optimal combination of machining parameters is used. For peak current (IP), pulse on time (TON), compaction pressure (CP) and wt. % of WC level 3 means high, 2 means medium, and 1 means low. For polarity (POL), 1 means positive, and 2 means negative, and for particle size (PS) 1 means NP electrode, 2 means NMP electrode, and 3 means MP electrode. In case of MRR, positive polarity (A1) at high level of peak current (B3), high level of pulse on time (C3), using NP electrode (D1), low level of WC% (E1) and low level of compaction pressure (F1) gives better results. Whereas in case of TWR, positive polarity of tool electrode (A1), low level of peak current (B1), low level of pulse on time (C1), MP electrode (D3), lower level of WC% (E1) and higher level of CP (F3) gives optimum results. To sum up, the optimal combination for MRR and TWR is A1B3C3D1E1F1 and A1B1C1D3E1F3 respectively.

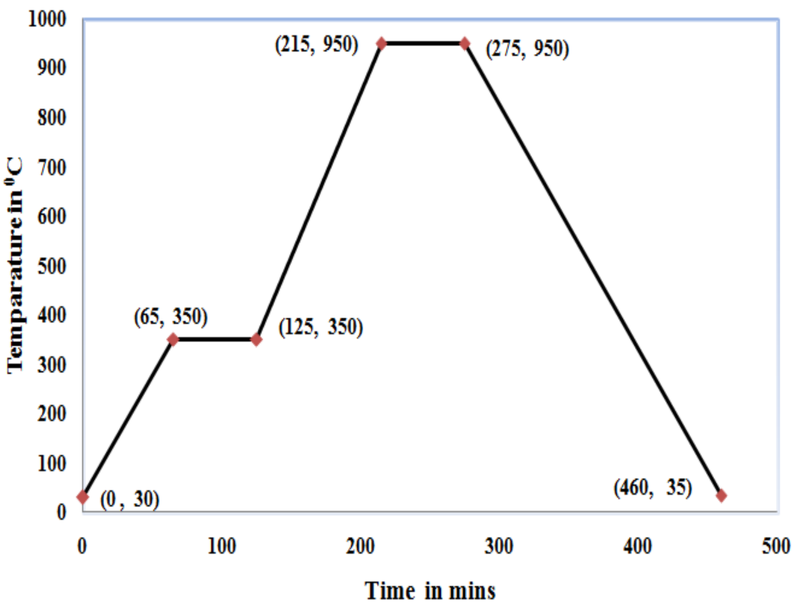

Figure 2. Sintering cycle for electrode perpetration

Table 4. Experimental layout using L18 (21x35) Orthogonal Array and Performance characteristics calculation

RUNS	POL	IP	TON	PS	%WC	CP	MRR		TWR	
							Mean MRR (mg/min)	S/N(dB)	MeanTWR (mg/min)	S/N(dB)
1	P	7	4	NP	40	200	9.10	19.1808	16.00	-24.082
2	P	7	8	NMP	50	300	7.80	17.8419	16.10	-24.137
3	P	7	12	MP	60	400	7.10	17.0252	15.25	-23.665
4	P	10	4	NP	50	300	9.00	19.0849	17.80	-25.008
5	P	10	8	NMP	60	400	7.85	17.8974	17.65	-24.935
6	P	10	12	MP	40	200	8.75	18.8402	16.45	-24.323
7	P	13	4	NMP	40	400	8.35	18.4337	16.00	-24.082
8	P	13	8	MP	50	200	9.15	19.2284	17.70	-24.96
9	P	13	12	NP	60	300	9.90	19.9127	20.70	-26.319
10	N	7	4	MP	60	300	6.80	16.6502	16.25	-24.217
11	N	7	8	NP	40	400	8.55	18.6393	16.95	-24.583
12	N	7	12	NMP	50	200	7.95	18.0073	18.45	-25.32
13	N	10	4	NMP	60	200	7.65	17.6732	18.30	-25.249
14	N	10	8	MP	40	300	7.75	17.786	16.40	-24.297
15	N	10	12	NP	50	400	8.70	18.7904	18.30	-25.249
16	N	13	4	MP	50	400	7.75	17.786	16.65	-24.428
17	N	13	8	NP	60	200	9.90	19.9127	20.35	-26.171
18	N	13	12	NMP	40	300	9.10	19.1808	18.20	-25.201

Table 5. S/N ratio Response table of MRR

Level	POL	IP	TON	PS	%WC	CP
1	18.61	17.89	18.13	19.25	18.68	18.81
2	18.27	18.35	18.55	18.17	18.46	18.41
3		19.08	18.63	17.89	18.18	18.10
Delta	0.34	1.18	0.49	1.37	0.50	0.71
Rank	6	2	5	1	4	3

Table 6. S/N ratio Response table of TWR

Level	**POL**	**IP**	**TON**	**PS**	**%WC**	**CP**
1	-24.61	-24.33	-24.51	-25.24	-24.43	-25.02
2	-24.97	-24.84	-24.85	-24.82	-24.85	-24.86
3		-25.19	-25.01	-24.32	-25.09	-24.49
Delta	0.36	0.86	0.50	0.92	0.66	0.53
Rank	6	2	5	1	3	4

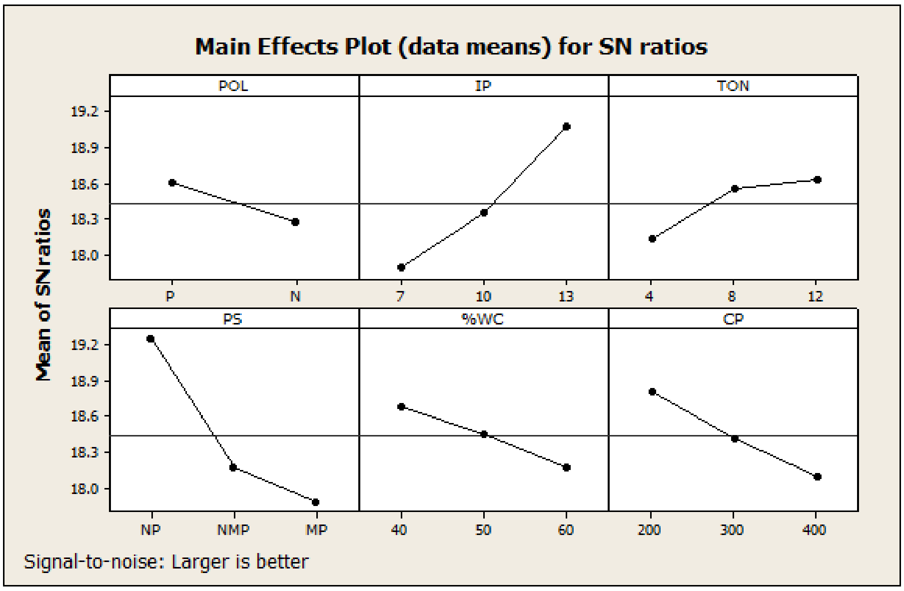

Figure 3. Main effect plots for MRR

3.1. Analysis of variance for MRR and TWR

ANOVA is a statistical method used to interpret experimental data to make the necessary decisions, concerning the parameters that affect the performance of the process. Based on this, parameters can be categorized into significant and insignificant machining parameters. Each parameter's influence on MRR and TWR are estimated and assessed in terms of percentage contribution (%P). ANOVA results were presented in Figure 5 for both MRR and TWR with 95% (α=0.05) confidence level. The contribution of individual parameters to the values of MRR and TWR are evaluated and shown in Tables 7 & 8 respectively. If p value is less than 0.05, it has significant effect on the performance measures. It is observed that all parameters are significant, but particle size and peak current are most significant (44.40% and 30.59%) for MRR. In case of TWR, all parameters are also significant, but particle size and peak current are most significant (28.92% and 25.52%). Both the MRR and TWR are significantly influenced by the parameters PS, IP, TON, %WC and CP. In continuation, experimental analysis viz. SEM studies for structural analysis at micro level, for Chemical analysis EDX is used, for phase analysis were carried out by XRD on the work surfaces made under optimum conditions and also on as received work pieces as presented below. The optimality of each parameter influencing the MRR and TWR are presented below.

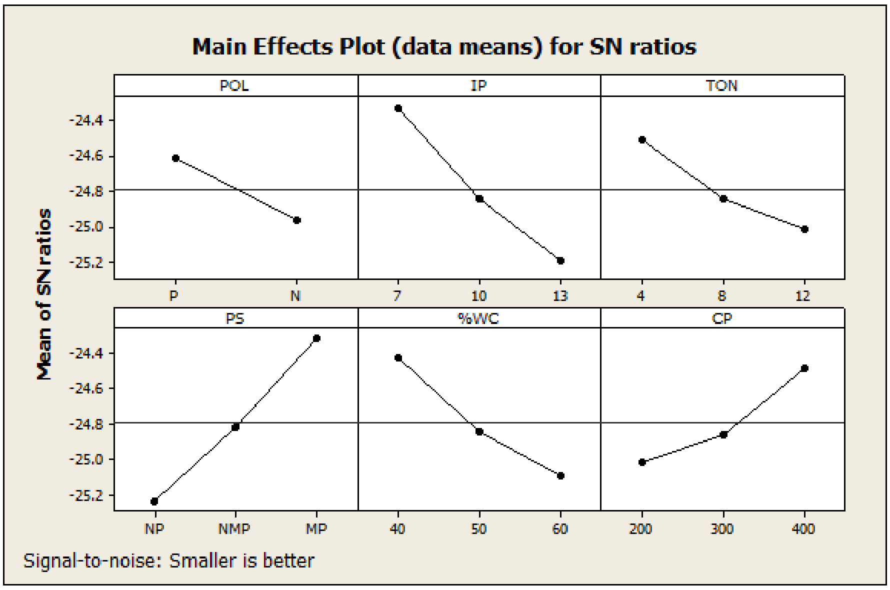

Figure 4. Main effect plots for TWR

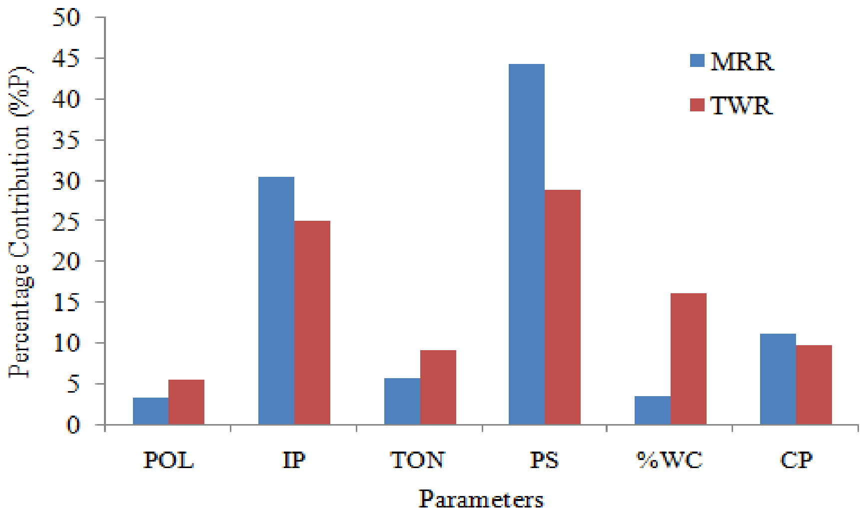

Figure 5. ANOVA for MRR and TWR

Table 7. ANOVA for MRR

Source	DF	Seq SS	Adj SS	Adj MS	F	Probability	% contribution
POL	1	0.4512	0.4512	0.4512	22.93	0.003	3.43
IP	2	4.0269	4.0269	2.0135	102.33	0.000	30.59
TON	2	0.7719	0.7719	0.3860	19.62	0.002	5.86
PS	2	5.8436	5.8436	2.9218	148.5	0.000	44.40
%WC	2	0.4803	0.4803	0.2401	12.20	0.008	3.65
CP	2	1.4703	1.4703	0.7351	37.36	0.000	11.17
Error	6	0.1181	0.1181	0.0197			
Total	17	13.1624					

Table 8. ANOVA for TWR

Source	DF	Seq SS	Adj SS	Adj MS	F	Probability	% contribution
POL	1	2.1356	2.1356	2.1356	6.87	0.040	5.70
IP	2	9.4033	9.4033	4.7017	15.13	0.005	**25.08**
TON	2	3.4658	3.4658	1.7329	5.58	0.043	9.25
PS	2	10.8400	10.8400	5.4200	17.44	0.003	**28.92**
%WC	2	6.0833	6.0833	3.0417	9.79	0.013	16.23
CP	2	3.6925	3.6925	1.8462	5.94	0.038	9.85
Error	6	1.8644	1.8644	0.3107			
Total	17	37.4850					

a) Polarity: It is noticed that positive polarity generates high MRR. Therefore, to exploit usage of positive polarity, Anode (discharge spot) and Cathode will be work piece and tool respectively. As a result, huge amount of particles of tool is transferred to work surface thereby resulting high MRR. In this case, the TWR is more than the MRR. The reason is being that WC has more density than copper, both of which emanate from the tool and WC is flushed out due to the flushing pressure of the die electric medium. It has been found that work material with low thermal conductivity would absorb less quantity of heat during machining, leading to low MRR. The low thermal conductivity coupled with high melting temperature of workpiece resulted in poor MRR, which led to increased TWR.

b) Peak Current: With the increase in the peak current, the MRR increases, and the thermal conductivity also increase. The reason is attributed to the availability of more energy when the current increases, thereby causing a stronger spark impact. Due to the increase in the thermal conductivity, there is a mild decrease in the MRR due to the decrease of availability of heat between the gap of electrode and work material. The result of availability of less heat leads to low MRR and high TWR.

c) Pulse on-Time: The current and pulse on-time have the direct relationship on the MRR and TWR. The outputs increase with increasing current and pulse on-time. The highest MRR obtained with the P/M electrode is 9.90 mg/min with the peak current of 13A and pulse duration of 12 μs. The rate of tool wear is higher compared to the material removal from the workpiece. The maximum value obtained for TWR is 20.70 mg/min which is also higher than the maximum MRR obtained under the same machining conditions because the following reasons/attributes are responsible for reducing MRR viz. (1) Reduction of WC and Cu particle size, (2) Thermal conductivity of WC increases, (3) surface to volume ratio changes and (4) shielding effect of nanoparticles [10]. Hence any of the attributes that makes such type of electrode is apt for work piece surface modification.

d) Particle Size: The NP electrode composite has resulted low values of MRR and TWR. In EDM process, with the increase in density of NP electrode, the amount of WC & Cu particles dropped from the electrode should increase. The smaller particles would be eroded first owing to their reactive surface area being much higher than that of the coarser ones. It is reported that EDM electrodes made with nano particles would have higher MRR and lower TWR than micro sized electrodes [12]. The use of sintered electrode increases the wear due to the fact that the thermal conductivity of composite material is greater than that of raw material [11]. It is observed in the present investigation on MRR and TWR increase and if nano particles are used, the reactive surface increases (over micron size particles [12] and [13]) leading to more erosion of material and increased MRR. The MRR is considerably low in case of nano-sized particles over micron sized particles.

e) Significance of %WC Composition: The density of WC is very high over Copper. The thermal conductivity of the composite tool electrode is improved in presence of low or high weight percentage of WC as it becomes denser. It is evident to observe that MRR is high, at 40% of WC due to the transfer of percentage of Copper particles from tool to work surface. Hence, the tool erosion rate at 60wt% of WC is low over the 40 & 50wt% compositions of WC.

f) Compaction Pressure: In general, low thermal conductivity, low melting temperature of Inconel 718 results in poor heat absorption due to this poor removal of work material in EDM [13]. Therefore, because the tool electrode has high thermal conductivity, more heat absorption capacity, and high melting point, it causes more material to transfer from tool to work surface. But it is observed that lower compaction pressures show high MRR and TWR. At lower value of CP, the particles bonded loosely on the tool do not withstand shock and higher temperature produces more heat absorption during machining causing more removal of material on the work surface.

3.2. Confirmation experiment

Based on the earlier evaluated combinations of specific factors and levels, an experiment for confirmation is performed. A new experiment is worked out finalizing the optimum conditions where in machining parameters of optimum level are considered. Finally, the prediction and verification of the improvement of performance characteristics is done. The improvements in the performance characteristics [14] are predicted by S/N ratio and optimum level of machining parameters and are given in Equation (3).

$$\eta_{opt} = \eta_m + \sum_{j=1}^{k} (\eta_j - \eta_m) \tag{3}$$

where

η_{opt}= predicted optimal S/N ratio

η_m= total mean of the S/N ratios

η_{j}= mean S/N ratio at the optimal levels and

k= number of main design parameters that affect the quality characteristics.

The confirmation test results are shown in Table 9 and it is observed that the experimental optimal mean value for MRR is 8.7843 mg and the estimated optimal mean value for TWR is 14.249 mg.

3.3. Significance of Particle Size effect on MRR

The experimental values of MRR are shown in Table 4 and the resultant signals to noise ratio values are in Table 5. ANOVA and F-test values are indicated in Table 7. In that, all considered factors are significant, but the most important factors are Particle size (44.9%) and Peak current (30.59%) when compared to other factors like CP (11.17%), TON (5.67%), %WC (3.65%) and POL (3.43%). The machining condition is A1B3C3D1E1F1 for best MRR. i.e.. Positive polarity, 13A peak current, 12µs pulse on-time, NP electrode, 40% of WC in tool electrode and 200MPa compaction pressure. Figure 6 shows the SEM image of workpiece at optimum MRR machining condition. The EDS spectrum of as received EDMed Inconel 718 and machined at optimum MRR conditions is shown in Figures 7 & 8 respectively. Formation of tungsten trioxide (WO_3) phase as shown in XRD image in Figure 9 indicates the small and less time of oxygen atoms diffused into the metal due to low discharge energies at optimum MRR optimum conditions.

Table 9. Confirmation test results and comparison with predicted results

Output Parameter	Best Parametric Experimental Conditions	Predicted	Actual	Error%
MRR (mg/min)	[A1B3C3D1E1F1] Polarity is Positive, 13A of peak current, 12µs of pulse on-time, NP electrode, 40% WC in tool electrode and 200MPa of compaction pressure.	9.4712	8.7843	7.82
TWR (mg/min)	[A1B1C1D3E1F3] Polarity is Positive, 7Aof peak current, 4µs of pulse on -time, MP electrode, 40% WC in tool electrode and 400MPa of compaction pressure.	13.2389	14.2490	7.09

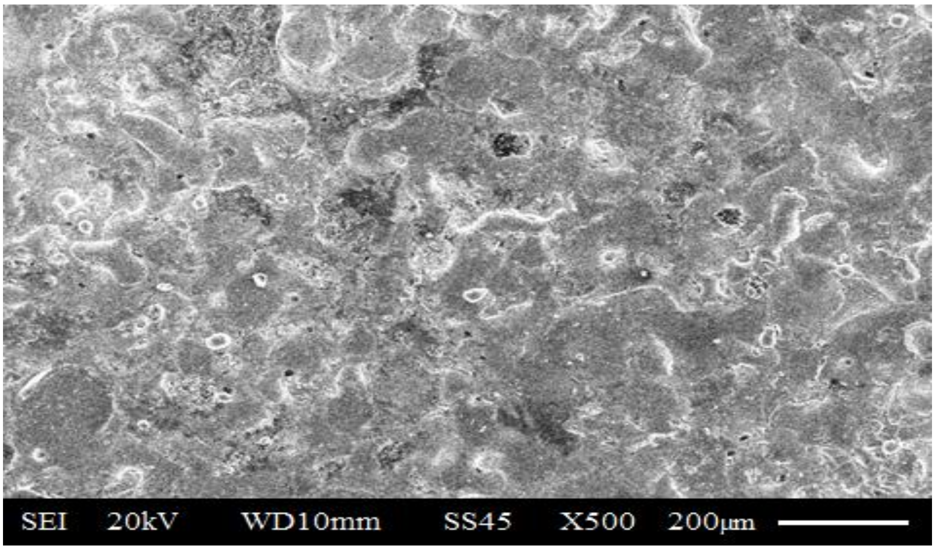

Figure 6. SEM image at optimal MRR machining condition

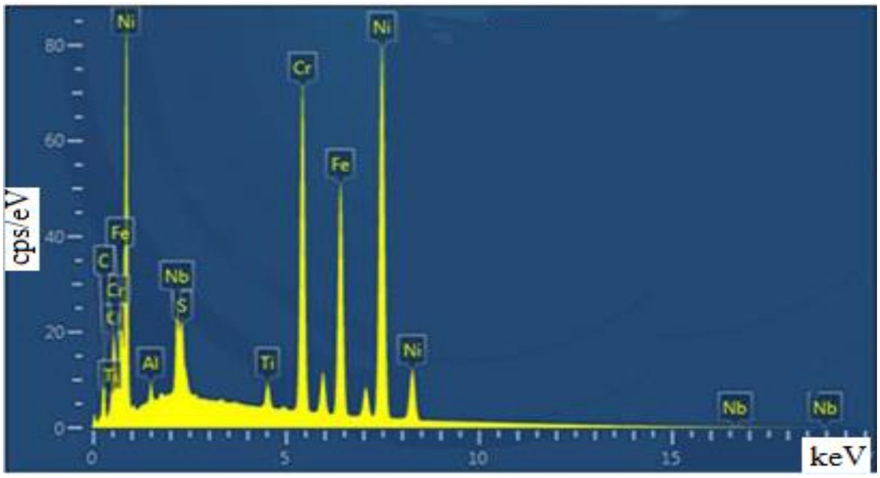

Figure 7. EDS plot for as received Inconel 718 alloy

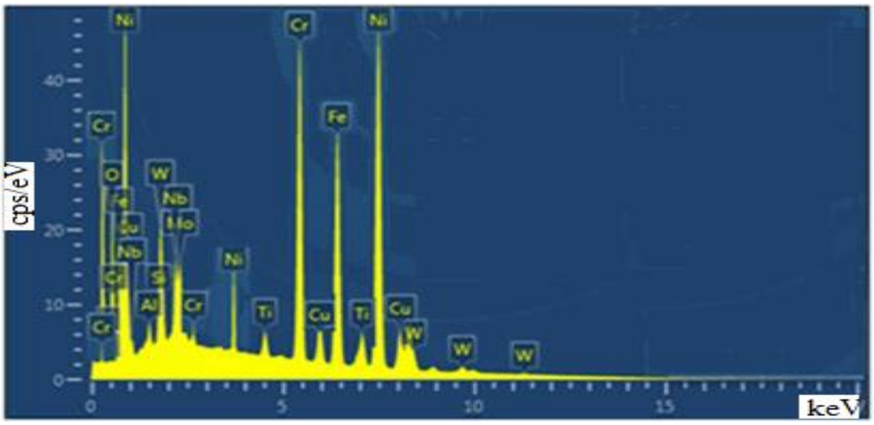

Figure 8. EDS plot of surface obtained at optimal MRR condition

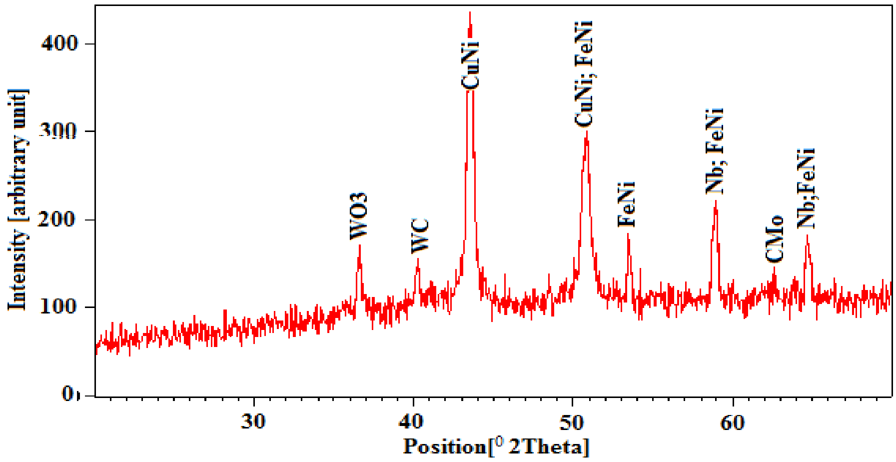

Figure 9. XRD pattern of machined surface at optimal MRR condition

3.4. Significance of Particle Size effect on TWR

Experimental results of TWR and its corresponding signal to noise ratio values are given in Table 4 and 6 respectively. ANOVA results are listed in Table 8. The ANOVA results and F-test values indicate that the most significant factors are Particle size (28.92%) and Peak current (25.08%). The machining condition A1B1C1D3E1F3 gives the best TWR. **i.e.** Positive polarity, 7A peak current, 4μs pulse on time, MP electrode, 40% of WC in tool electrode and 400 MPa compaction pressure. SEM image of TWR at optimum machining conditions can be seen in Figure10 and the spectrum obtained for surface machined at optimal TWR conditions is shown in Figure 11. It is reported that EDM electrodes made with micron particles would have higher TWR, because the density of WC is more when compared to Cu. The XRD image in Figure 12 shows the machined component at optimum TWR condition. The lower value of IP and TON at optimal tool wear conditions generates the lower temperature conditions. These lower temperatures are responsible for the formation of Hagg carbide (Fe_5C_2) and ferrous carbides (Fe_7C_3) which are usually forms at lower temperature in the ferrous carbide series [16].

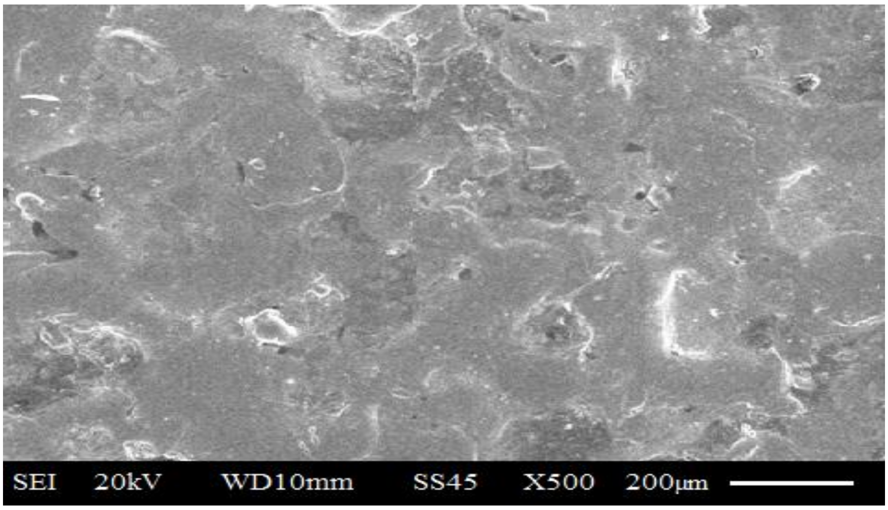

Figure 10. SEM image at optimal TWR machining condition

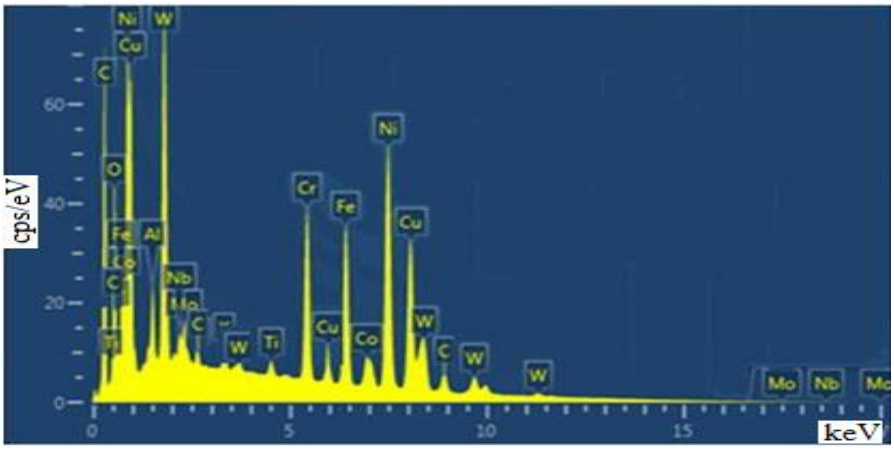

Figure 11. EDSplot of surface obtained At optimal TWR condition

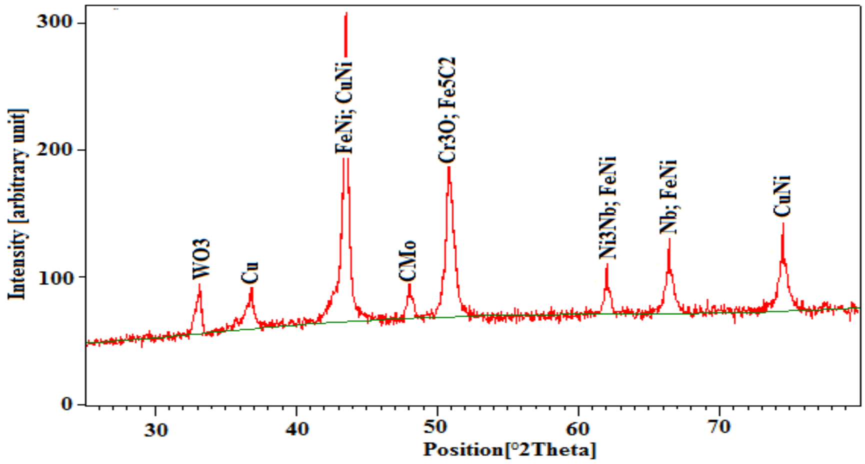

Figure12. XRD plot of the surface machined at optimal TWR condition

4. Conclusions

The influence of input parameters on the performance characteristics of EDM process with Cu-WC mixed ceramic compact sintered electrode was investigated using MRR and TWR as the basic criteria. The following conclusions are drawn from the results.

1. Material removal rate at most favorable condition (i.e. A1B3C3D1E1F1) is increased with increases of IP, TON and decreased with increase in the PS, %WC and CP. It is noticed that MRR is directly proportional to the IP and TON.
2. Tool wear rate at optimum condition (i.e. A1B1C1D3E1F3) was increased with decreases of IP, TON, %WC and increased with increase in the PS, and CP. It was noticed that TWR was inversely proportional to the IP, TON and %WC.
3. The experimental analysis shows that POL, IP, TON, PS, %WC and CP have significantly influenced MRR and TWR. The parameters, Particle size and peak current would be more contribution to MRR and TWR, when compared to other input parameters.
4. At optimal combinations of parameters, the MRR and TWR values obtained are 9.90mg/min and 13.23 mg/min respectively. The use of NP electrodes in the present study has considerably reduced the MRR values when compared to TWR. i.e., the surface modification was done by the small particle sizes.

REFERENCES

[1]B.K.Sahu, SauravDatta, S.S.Mahapatra, "On Electro-Discharge Machining of Inconel718 Super Alloys:An Experimental Investigation". Materials Today: Proceedings, Vol.5, 2018, 4861–4869.

[2] FarshidJafarian, "Electro discharge machining of Inconel 718 alloy and process optimization". Materials and Manufacturing Processes, Vol.35, No.1, 2020, 95-103.

[3] C.Cogun, Z. Esen, A.Genc, F.Cogun, N. Akturk, "Effect of powder metallurgy Cu-B_4C electrodes on work piece surface characteristics and machining performance of electric discharge machining". Proceedings of the Institution of Mechanical Engineers, Part B: Journal of Engineering Manufacture, Vol. 230, 2016, 2190-2203. 69

[4] S. Rajesh, A.k. Sharma, Pradeep Kumar. "On Electro Discharge Machining of Inconel 718 with Hollow Tool". Journal of Materials Engineering and Performance, Vol. 21, 2012, 882-891.

[5] V. Srikanth, G.S. Upadhyaya, "Effect of tungsten particle size on the sintered properties of heavy alloys". Powder Technology, Vol.39, 1984, 61-67.

[6] A.K.Khanra, B.R.Sarkar, B.Bhattacharya, L.C.Pathak, M.M. Godkhindi, "Performance of ZrB2-Cu composite as an EDM electrode". Journal of Materials Processing Technology, Vol.183, 2007,122-126.7

[7] V.RamakoteswaraRao, N.Ramanaiah, M.M.M.Sarcar, "Optimization of Volumetric Wear Rate of AA7075-TiC Metal Matrix Composite by Using Taguchi Technique". Jordan Journal of Mechanical and Industrial Engineering, Vol. 10, No.3, 189-198.

[8] Abhishek Das, Joy Prakash Misra, "Experimental investigation on surface modification of aluminum by electric discharge coating process using TiC/Cu green compact tool electrode". Machining Science And Technology,Vol.16, No.4, 2012, 601-623.57

[9] Li L., Y.S. Wong, J.Y.H. Fuh, L. Lu, "Effect of TiC in copper-tungsten electrodes on EDM performance". Journal of Materials Processing Technology, Vol.113, 2001, 563-567.113

[10] Shubhajit Das. "Surface alloying of aluminium by W-Cu-Cr powder metallurgy tool electrode in EDM". International journal of advance research in engineering and system, Vol.2, No.4, 2016, 1-10,.

[11] C.Y. Bai, C.H. Koo, "Effects of kerosene or distilled water as dielectric on electrical discharge alloying of superalloy Haynes 230 with Al-Mo composite electrode". Surface coatings and technology, Vol.200, 2006, 4127-4135. 118

[12] Ch.Venkata Rao, K.Ramji, P.Srinivasa Rao, "Surface Modification of Ti6Al4V Alloy Using EDMed Electrode Made with Nano- and Micron-Sized TiC/Cu Powder Particles". Arabian Journal for Science and Engineering, Vol.44, 2019, 1425–1436.

[13] A.S. Gill, S. Kumar, "Surface alloying of H11 die steel by tungsten using EDM Process". The international journal of advanced manufacturing technology, Vol.78, 2015, 1585-1593,182

[14] M.P.Samuel, P.K.Philip, "Powder metallurgy tool electrodes for electric discharge Machining". International journal of machine tools and manufacture, Vol.37, 1997, 1625-1633.41

[15] A.A. Khan, "Electrode wear and material removal rate during EDM of aluminum and mild steel using copper and brass electrodes". International Journal Advanced Manufacturing Technology,Vol. 39, 2008, 482–487.

[16] P. S. Rao, N.S. Purnima, D. S. Prasad, "Surface alloying of D2 steel using EDM with WC/Co P/M electrodes made of Nano and Micron sized particles", Materials Research Express, Vol. 6, 2019, 036511(1-15).

JJMIE

Volume 15, Number 5, December. 2021
ISSN 1995-6665
Pages 461 – 474

Jordan Journal of Mechanical and Industrial Engineering

On the Use of Rigid-Body-Translations for Determining Surface Tilt Angles in Two-dimensional Digital Image Correlation Experiments: A Generalized Approach

Ala Hijazi

Department of Mechanical Engineering, German Jordanian University, Amman, Jordan

Received July 26 2021 *Accepted October 20 2021*

Abstract

The two-dimensional digital image correlation (2D-DIC) technique is used for making full-field in-plane deformation/strain measurements on planar surfaces. One of the basic requirements for making measurements using 2D-DIC is to observe the target surface perpendicularly by the camera. Ensuring camera perpendicularity before starting to make measurements using 2D-DIC is important because errors will be induced in the measured displacements/strains if the camera is not oriented properly. During the initial setting of an experimental setup, small camera misalignment angles of one or two degrees can easily go undetected. This paper reports a simple and reliable approach for verifying the camera perpendicularity in 2D-DIC experiments, and for measuring the tilt angle(s) if the camera is not perpendicular to the surface. The approach uses in-plane rigid-body-translation where the strain error(s) obtained from DIC measurements are used to calculate the tilt angle(s). The translation can be either parallel to the target plane (done by moving the target) or parallel to the camera plane (done by moving the camera) where a different set of equations is used for calculating the tilt angles in each scenario. A translation of a known magnitude in any in-plane direction (parallel to the *x* or *y* axes of the image, or at any angle in between) is all what is required to calculate the tilt angle(s). The approach is also capable to determine the tilt angles if the target is tilted about any of the two in-plane axes (*x* or *y*) or about the two axes simultaneously. Several rigid-body-translation experiments are performed under different conditions to evaluate the validity and accuracy of this approach at tilt angles between 1° and 4°. The results show that tilt angles as small as 1° can be calculated accurately, and that rigid-body-translation as small as 2% of the field-of-view width can be used for making measurements with good accuracy.

Keywords: Digital image correlation; 2D-DIC; normal strain error; shear strain error; strain bias; camera non-perpendicularity; camera misalignment; tilt angle; rigid-body-translation.

1. Introduction

Digital image correlation (DIC) is a non-contact technique that provides full-field measurements of surface movements (both deformation and rigid-body motion) using digital images. Such measurements are performed by monitoring the relative movements of unique features on the surface of a body or a structure under load. Since most surfaces do not have unique features for cameras to trace, random speckle patterns are usually painted on the surface. The DIC technique was first introduces in the early 1980s, and over the years, it underwent continuous improvements [1]. With the improved resolution and performance of digital cameras, the DIC technique has rapidly evolved, and it has found its way in more and more applications. Today, DIC has been successfully utilized in a very wide variety of applications ranging from mechanical, aerospace, structural, civil, electronics, materials, and manufacturing engineering, to non-destructive testing and evaluation, to biomedical and life sciences [1-16]. Also, DIC can be performed using images ranging in scale from microscopic (even scanning electron microscopy) images all the way up to images of full-scale structures, and ranging in capture speed from few frames per second (fps) all the way to more than one million fps [1-6, 17-20]. Furthermore, DIC has also found use in high temperature applications using images captured in the ultraviolet spectrum [21]. Besides the good measurement accuracy of the DIC technique, it also offers some of attractive features such as; relatively low cost equipment, relatively simple experimental setup, simple or no specimen preparation and not so strict requirements for the measurement environment. Due to its capabilities and advantages, DIC has now become the most widely used technique for non-contact full-field surface motion and deformation measurements.

The DIC technique has two variations; 2D-DIC and 3D-DIC. The 2D-DIC is the simplest version of the technique where images are recorded using one camera, and these images are used for making in-plane motion and deformation measurements of planar surfaces. On the other hand, the 3D-DIC uses two (or more) cameras in stereo configuration that capture simultaneous image sequences, and it is capable of making three-dimensional measurements on surfaces of any shape. Both the 2D-DIC and 3D-DIC are increasingly being used in a wide variety

* Corresponding author e-mail: Ala.Hijazi@gju.edu.jo.

of research and industrial applications [1-6]. In general, the 3D-DIC is more robust, and it offers more capabilities than 2D-DIC.But nevertheless, the 2D-DIC offers some advantages that make it more appropriate for use in some situations, and in general, it is more suitable for testing done in the field. The advantages of 2D-DICare; lower initial cost for both the equipment and software, lower computational cost, ease of use, and the relatively less stringent requirements for the experimental setup (e.g., calibration is generally not required). Practically, three conditions/assumptions need to be satisfied in order to make accurate deformations/strains measurements using 2D-DIC. These conditions are: i) the specimen should have a planar surface, ii) the specimen should undergo pure in-plane motion/deformation (i.e., no out-of-plane component of the motion), and iii) the camera should be oriented perpendicularly relative to the surface of the specimen. In addition, there are several other factors, or sources of error, that can affect the accuracy of 2D-DIC measurements, and there are numerous research studies addressing the error assessment in 2D-DIC and DIC in general [1, 22-26]. These factors include: I) the speckle pattern (density, contrast, size distribution, etc.), ii) the imaging system (lens optical distortions, sensor type, noise, resolution, camera and lens settings etc.), and iii) the selection of the correlation algorithm and parameters (subset and step sizes, correlation and shape functions, sub-pixel interpolation algorithm, etc.). One of the simplest and most widely accepted approaches for assessing the level of baseline error in DIC measurements is the use of rigid-body-translation experiments, which was first introduced by Chu et al. [27]. For 2D-DIC, when the target surface undergoes an in-plane rigid-body-translation, the strains measured by the DIC software should theoretically be zero. Therefore, any strains obtained by DIC during such translation, simply reflects an error in the strain measurements. In experiments where 2D-DIC is to be used, before running the actual experiments, it is usually recommended to perform an in-plane rigid-body-translation experiment (under the same settings and conditions to be used in the actual experiments) in order to estimate the overall level of strain error (both the bias and random error) in the DIC measurements.

For 2D-DIC measurements, as stated earlier, the specimen is assumed to undergo in-plane motion/deformation only (i.e., no out-of-plane motion) and to be perpendicular to the camera viewing axis. The satisfaction these two conditions are essential to the accuracy of the measurements. In general, out-of-plane translations and/or rotations may occur during the loading of the specimen, and several studies have investigated errors associated with such cases. Haddadi et al. [23] estimated the strain errors resulting from out-of-plane translations using rigid-body-translation experiments. Sutton et al. [28] studied the effects of out-of-plane translations/rotations both theoretically and experimentally and showed that such error can be significant, and that it is inversely proportional to the distance between the camera and the surface. Siddiqui [29] proposed a method for eliminating the displacement bias caused by out-of-plane motion through including the possible modes of global rigid-body motion of the specimen surface within the calculation of in-plane displacements. Pan et al. [30] used rigid-body-translation experiments to study the strain error resulting from out-of-plane translations, and they proposed a method to compensate for the effect of out-of-plane translation using a non-deformable reference sample. Badaloni et al. [31] examined the error caused by out-of-plane movement during cyclic loading and proposed a method to compensate for such error using non-deformable plates fixed on the surface of the specimen. Halding et al. [32] proposed a method for the correction of strain measurements for the effect of out-of-plane motion (including rotation) of the surface. They applied their method for measuring strains in bridges using wide-angle lens camera during load testing.

Besides the out-of-plane translation and/or rotation that might occur during the experiments, it is also possible to have an inappropriate alignment of the camera such that it is not observing the surface perpendicularly. Such camera non-perpendicularity can exist before loading starts, and it remains throughout the experiment. Some researchers have investigated the measurement errors associated with the cases where the camera axis is not perpendicular to the target surface. Meng et al. [33] studied the effect of the non-perpendicular camera alignment on the measurement accuracy of in-plane displacements. Based on theoretical analysis, they reported that measurement sensitivity of 0.01 pixels could be attained under misalignment angles up to 5° (for the parameters used in their investigation). Lava et al. [34] studied the strain errors induced by non-perpendicular camera alignment using numerically tilted images having an imposed finite element displacement field. They proposed an image rectification method for eliminating the image distortion caused camera non-perpendicularity (such that the images will be suitable for 2D-DIC), and they compared the strain error for a sample subjected to large plastic strain using 2D-DIC and 3D-DIC. Such image rectification approach can be useful when there are physical/experimental constrains that prevent the camera from being oriented perpendicularly, given that the surface tilt angle is known. Wang et al. [35] proposed a method of compensation for both out-of-plane motion (including out-of-plane translation and out-of-plane rotation) and non-perpendicular alignment, in order to improve the accuracy of 2D-DIC measurements. Their method is based on projecting a cross-shaped structured light pattern on the surface of the specimen and using triangulation to calculate the out-of-plane translation/rotation from the deformation of the structured light. The obtained out-of-plane motion information is then used to compensate the strains measured by DIC. They conducted experiments with controlled out-of-the-plane motions to verify their proposed approach and reported that the mean error after compensation can be as small as 50 μ-strains. Hijazi et al. [36] investigated the errors in strain measurements caused by non-perpendicular camera alignment both theoretically and experimentally. They developed analytical equations for determining the magnitude of the strain error (bias) resulting from camera non-perpendicularity. They showed that camera non-perpendicularity cause errors to be induced in both the normal and shear strains, and that a strain error greater than 10^3 μ-strains can result from misalignment angles as small as 2°. In general, a translation perpendicular to the tilt axis causes apparent normal strains while a translation parallel to the tilt axis causes apparent shear strain. These non-zero strains (i.e., strain errors) can be observed when performing DIC on images of tilted specimens undergoing in-plane rigid-body-translations. Furthermore, a non-perpendicular alignment will cause bias in the strain readings when performing DIC on images of a specimen undergoing actual deformation. In-plane rigid-body-translation experiments were used to validate the analytical equations, and the results were found to be in a very close agreement. Later, Hijazi [37] introduced a novel approach for verifying camera perpendicularity and calculating the camera tilt angle (if the camera is not perpendicular to the target surface). This approach is intended to be used as a verification/calibration step during the initial setting of 2D-DIC experiments (i.e., before starting to use the experimental setup for actual measurements). The approach is based on the strain error equations developed previously by Hijazi et al. [36]. These equations were simplified and solved to obtain the tilt angle(s) of the target surface based on the strain error(s) caused by camera non-perpendicularity. The essence of the approach is to do a simple in-plane rigid-body-translation experiment, then to use the developed equation(s) to calculate the tilt angle(s) base on the strain error(s) obtained from DIC analysis. The approach involves doing the rigid-body-translation using the same specimen to be tested (before running the actual experiment) where the translation can be in either of the two in-plane directions (x or y). The approach was validated experimentally and it was shown that it has accuracy better than 0.3°, and that it can be used to measure tilt angles as small as 1° about any of the two in-plane axes.

During the initial setting of an experimental setup where 2D-DIC is being used, care is usually taken to align the camera perpendicular to the target surface. The camera alignment is usually done using mounting hardware and simple measuring tools (translating stages, right angle triangles, tape measures, inclinometers, etc.). When the distance between the camera and the target is relatively small, ensuring camera perpendicularity can be somewhat easy. However, as the working distance between the camera and target becomes larger, ensuring camera perpendicularity becomes more difficult, and small camera misalignment angles of one or two degrees can easily go undetected. Up to the knowledge of the author, there are no methods for ensuring camera perpendicularity in such cases reported in literature. The novel method for determining the tilt angles proposed by Hijazi [37] was the first and still the only method reported in literature for ensuring camera perpendicularity and estimating the tilt angles in 2D-DIC experiments (where only one camera is used). In this paper, a more generalized approach for determining the surface tilt angle(s) using rigid-body-translation experiments is presented. The approach initially proposed by Hijazi [37] is extended in this paper to address some cases that were not considered previously, and some of the practical issues related to the use of this approach are also addressed. The case where the translation is parallel to the plane of the camera (rather than the target) is investigated here and new equations for the strain error and for calculating the tilt angle are developed for this case. The translation parallel to the camera can be done by moving the camera itself, and such approach can be useful when it is not possible to do the rigid-body-translation using the target. Additionally, while the work presented in Hijazi [37] only considers translations that are either parallel or perpendicular to the tilt axis, the case where the translation is in some arbitrary in-plane direction (i.e., it has both x and y components) is considered here. Furthermore, the case where the target is tilted about both the x and y axes, simultaneously, is also investigated. Moreover, in some practical cases, it might not be possible to do large translations. Thus, the feasibility of using very small translations (as small as 1% of the field-of-view width) for performing measurements is investigated. Finally, the effect of the distance between the camera and the target on the measurement accuracy is demonstrated. All the above-mentioned cases are investigated experimentally, and the results of these validation experiments are presented in this paper.

2. Theory

Perpendicularity of the camera's optical axis with respect to the surface being observed is one of the conditions for the validity of 2D-DIC measurements. If there is a misalignment between the camera plane and the target surface, in-plane translations of the surface will not be accurately depicted at the camera's imaging sensor. Accordingly, when DIC analysis is performed using such images, even if the surface is undergoing a pure in-plane rigid-body-translation, it will appear as if it is being deformed (i.e., there will be nonzero strains). Previous investigations have shown that non-perpendicular camera alignment causes strain errors (in the form of bias) where the type and magnitude of these strain errors depend on the direction of the in-plane translation relative to the tilt axis of the camera (or target) [36, 37]. When the target surface translates perpendicular to the tilt axis, normal strain error will be induced. On the other hand, when the surface translates parallel to the tilt axis, shear strain error will be induced. Based on the pinhole camera model along with the small-strains theory (Cauchy strain), Hijazi et al. [36] developed theoretical equations for determining the normal and shear strain errors resulting from camera non-perpendicularity. These equations show that the strain errors are proportional to the misalignment (or tilt) angle, and they are also function of the direction and magnitude of the rigid-body-translation, as well as the stand-off-distance between the camera and the surface. Later, Hijazi [37] further developed these strain error equations and introduced a novel approach for calculating the surface tilt angle(s) based on the apparent DIC strain(s) error. This approach utilizes simple in-plane rigid-body-translation (in the direction parallel or perpendicular to the tilt axis) to measure the normal and shear strain errors caused by camera non-perpendicularity using DIC analysis. It then calculates the tilt angle(s) using simple analytical equations based on the measured strain error. This simple approach is meant to be used as a verification/calibration step during the initial setup of 2D-DIC experiments (i.e., before starting to use the setup for actual measurements). By translating the target in any of the two in-plane directions (horizontal or vertical), the tilt angles about the axis parallel and the axis perpendicular to the direction of translation (if any exists) can be calculated. Three simple equations were developed for calculating the surface tilt angle, which are [37]:

$$\theta_{\perp} \cong \sin^{-1}\left[\frac{\varepsilon_{xx}S}{2\Delta x+\varepsilon_{xx}(\Delta x - x_A)}\right] \qquad (1)$$

$$\theta_{\perp} = \sin^{-1}\left[\frac{\varepsilon_{yy}S}{\Delta x+\varepsilon_{yy}(\Delta x - x_A)}\right] \qquad (2)$$

$$\theta_{/\!/} = \tan^{-1}\left(\frac{2\varepsilon_{xy}S}{\Delta y}\right) \qquad (3)$$

where ε_{xx}, ε_{yy} and ε_{xy} are the strain errors resulting from rigid-body-translation (obtained from DIC analysis), S is the target stand-off-distance, x_A is the *x* coordinate of a point on the surface (usually $x_A = 0$ is used), Δx & Δy are the magnitudes of rigid-body-translation in the x and y directions. In fact, all the three equations theoretically give the same tilt angle. The first two equations are used (any one of them can be used) to find the tilt angle (denoted as $\theta_{\perp}$) based on the DIC normal strain errors (ε_{xx} or ε_{yy}) resulting from rigid-body-translation perpendicular to the tilt axis. The third equation, on the other hand, is used to find the tilt angle (denoted as $\theta_{/\!/}$) based on the DIC shear strain (ε_{xy}) error resulting from rigid-body-translation parallel to the tilt axis. It is probably worth mentioning here that equation 1 is based on an approximate solution for the normal strain (ε_{xx}) error, yet it was shown to be fairly accurate [37]. It is also important to note that this approach is capable of determining not only the magnitude of the tilt angle, but also the direction of rotation (or sense). The direction of rotation can be determined based on the sign of the strain error where the tilt angle will have the same sign as the strain error obtained from the DIC analysis. For non-perpendicular camera orientation, the sign of the strain error in DIC analysis depends on the direction of translation (flipping the reference and deformed images in DIC analysis will flip the sign). Hence, the direction of rotation can be identified relative to the direction of translation. In addition, it should be noted here that, though DIC software packages use the large strains theory (Green-Lagrange strain) for calculating strains, small strains theory was used for deriving the theoretical strain error equations where that is justified based on the fact that the strains resulting from camera non-perpendicularity are relatively small (given that the tilt angles are small). The resulting strain error obtained by these equations was also validated experimentally by comparing with DIC results [36].

The equations developed previously by Hijazi [37] (equations 1 to 3) assume that the rigid-body-translation is parallel to the plane of the target. To further generalize the approach, in the work presented herein, the case where the rigid-body-translation is parallel to the camera plane (rather than the target plane) is also considered. To illustrate the difference between the two cases, Figure 1 shows a schematic representation of a non-perpendicular camera setup. In the figure, the coordinate system is defined relative to the target surface where the$z$axis is normal to the surface and the target is tilted by angle θ about the y axis (x and y are the in-plane axes of the target). If the surface is not tilted (i.e., camera perpendicular to the target surface) the axes of the coordinate systems of the camera and the target will be all parallel. The figure also illustrates that the translation of the target along the x direction (i.e., the direction perpendicular to the tilt axis) can be either parallel to the target plane (Δx) or parallel to the camera plane (Δx_c). The strain errors resulting from translations parallel to the target plane and how they can be used to determine the surface tilt angle were illustrated in a previous investigation [37]. The effect of translations parallel to the camera plane and how to use the resulting DIC strain error(s) to determine the tilt angle are presented in this investigation. It should be stressed here that in actual DIC experiments, a translation parallel to the camera plane would most likely be performed by translating the camera itself. However, theoretically it does not make a difference whether the camera or the target are translated as long as the translation is parallel to the camera plane.

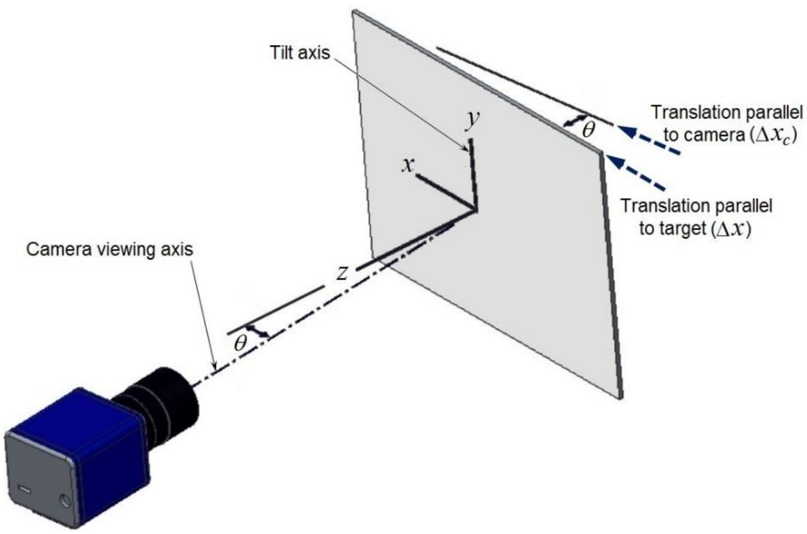

Figure 1. Schematic illustration of the orientation of a non-perpendicular camera setup.

A schematic illustration of the pinhole camera model and how it resembles a real camera is shown in figure 2. In the figure, the image plane identifies the location of the camera's imaging sensor or focal plane array (FPA) while the location of the pinhole plane represents the mid-thickness of the lens. The distance f in the figure (i.e., the distance between the pinhole plane and the image plane) represents the focal length of the lens. It might be worth mentioning here that for multi-element lenses typically used in imaging, the physical distance from the lens mid-thickness to the FPA is slightly different from the focal length of the lens; yet still, this geometric model holds true. The distance S between the pinhole plane and the object is referred to as the stand-off-distance. This stand-off-distance is slightly larger than the actual distance from the front end of the lens body to the target surface (usually referred to as the working distance) as will be further discussed later. According to the pinhole model, an object of length $l$will have a projected length of l^i at the image plane (assuming that the object is parallel to the image plane) where:

$$l^i = \frac{l}{S} f \tag{4}$$

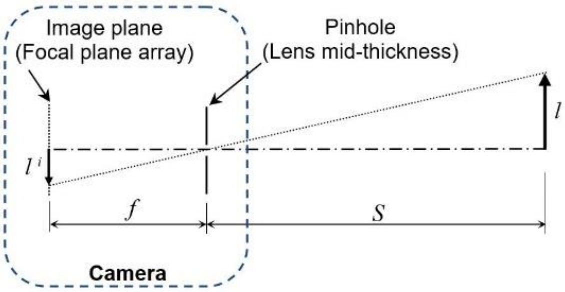

Figure 2. Schematic illustration of the pinhole camera model.

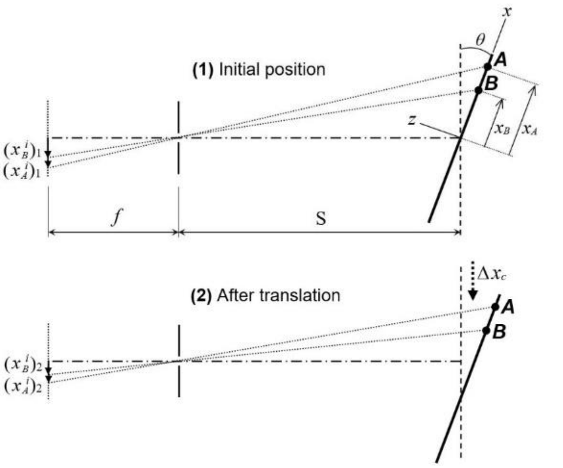

Figure 3. Pinhole camera schematic of a tilted surface translating perpendicular to tilt axis (the translation is parallel to the camera plane).

Figure 3 shows a schematic planar representation of a pinhole camera imaging a target surface tilted by angle θ (about the y axis). This figure actually represents a top projection view of the setup seen in figure 1, and the same notations are used in both figures. The surface is considered to rigidly translate by a distance Δx_c (in the direction parallel to the camera plane). For clarity, the positions of the surface before and after the translation are shown in two separate sketches as seen in the figure. A line segment is defined on the target surface (along the x direction) between points **A** and **W**here the line segment has a length of l_x. When the surface is at position (**1**), the x coordinates "at the image plane" for points **A** and **B** are found as:

$$\left(x_A^i\right)_1 = \frac{x_A \cos\theta}{S + x_A \sin\theta} f \tag{5}$$

$$\left(x_B^i\right)_1 = \frac{x_B \cos\theta}{S + x_B \sin\theta} f = \frac{(x_A - l_x)\cos\theta}{S + (x_A - l_x)\sin\theta} f \tag{6}$$

where x_A & x_B are the coordinates of the two points at position (**1**). Using the coordinates "at the image plane", the projected length of line **AB** "at the image plane "can simply be found as:

$$\begin{aligned}\left(l_{AB}^i\right)_1 &= \left(x_A^i\right)_1 - \left(x_B^i\right)_1 \\ &= \left[\left(\frac{x_A}{S + x_A \sin\theta}\right) - \left(\frac{x_A - l_x}{S + (x_A - l_x)\sin\theta}\right)\right]\cos\theta\, f\end{aligned} \tag{7}$$

When the surface moves to position (**2**) after translating a distance Δx_c, the new x coordinates of the two points "at the image plane" become:

$$\left(x_A^i\right)_2 = \frac{x_A \cos\theta - \Delta x_c}{S + x_A \sin\theta} f \tag{8}$$

$$\left(x_B^i\right)_2 = \frac{x_B \cos\theta - \Delta x_c}{S + x_B \sin\theta} f = \frac{(x_A - l_x)\cos\theta - \Delta x_c}{S + (x_A - l_x)\sin\theta} f \tag{9}$$

and therefore the projected length of line **AB** "at the image plane" becomes:

$$\begin{aligned}\left(l_{AB}^i\right)_2 &= \left(x_A^i\right)_2 - \left(x_B^i\right)_2 \\ &= \left[\left(\frac{x_A \cos\theta - \Delta x_c}{S + x_A \sin\theta}\right) - \left(\frac{(x_A - l_x)\cos\theta - \Delta x_c}{S + (x_A - l_x)\sin\theta}\right)\right] f\end{aligned} \tag{10}$$

The average (Cauchy) normal strain for the line segment in the x direction can be calculated as:

$$\varepsilon_{xx} = \frac{\left(l_{AB}^i\right)_2 - \left(l_{AB}^i\right)_1}{\left(l_{AB}^i\right)_1} \tag{11}$$

Substituting equations (7) and (10) into equation (11) and simplifying the resulting expression, both the focal distance f and the line segment length l_x cancel out, and the strain error equation becomes:

$$\varepsilon_{xx} = \frac{\Delta x_c}{S} \tan\theta \tag{12}$$

Equation (12) can be solved to obtain the surface tilt angle based on the normal strain error ε_{xx} obtained from DIC analysis. As used previously in equations (1) and (2), the calculated tilt angle is denoted as $\theta_\perp$ to indicate that this is a tilt angle that is calculated based on a translation in the direction perpendicular to the tilt axis, and it is found as:

$$\theta_\perp = \tan^{-1}\left[\frac{\varepsilon_{xx} S}{\Delta x_c}\right] \tag{13}$$

Similarly, it is necessary to determine whether the translation Δx_c will also induce an “apparent " normal strain in the y direction. Considering a line of length l_y(oriented along the y direction) that is defined at an arbitrary distance along the x axis (assumes for instance a line oriented in the y direction and located at point **A**). By referring to Figure 3 again, it can be seen that the "horizontal" distance from point **A** to the pinhole plane does not change as a result of the translation Δx_c. Since the horizontal distance remains unchanged after the "vertical" translation (Δx_c), any line segment defined in the y direction will still have the same projected length at "the image plane" after the translation Δx_c. Thus, there will be no apparent normal strain in the y

direction as a result of the translation Δx_c (i.e., $\varepsilon_{yy} = 0$). Also, the inspection of the coordinates of the line segments defined along the x and y directions shows that the orientation of these lines will not be affected due to the translation Δx_c. Therefore, it is also concluded that there will be no apparent shear strain error resulting from camera non-perpendicularity when the translation is perpendicular to the tilt axis (i.e., $\varepsilon_{xy} = 0$). For comparison purposes, and to avoid confusion, the strain errors resulting from translations perpendicular to the tilt axis for both cases, parallel to the target plane and parallel to the camera plane, are summarized in Table 1 (equations for translation parallel to camera plane are obtained from Hijazi [37]). A quick comparison of the magnitude of the strain error in the direction of translation (ε_{xx}) shows that when the translation is parallel to the camera plane, the strain error is approximately half of that when the translation is parallel to the target plane (assuming $x_A = 0$, $\Delta x \ll S$, and small angles: $\sin\theta \cong \tan\theta$).

3. Experiments

3.1. Setup

The camera used in this investigation is a 5.5 megapixel monochrome scientific imaging camera (PCO Edge 5.5). This camera has a scientific-Complementary Metal Oxide Sensor (sCMOS) chip with 2560×2160 pixels resolution, 18.8 mm sensor size, and 16 bit dynamic range. The lens used with the camera is a premium quality 50mm focal length lens (ZEISS Milvus 2/50M). During the experiments, the lens aperture is set at f/8 to ensure that the entire target surface is in good focus even when the target is tilted at the maximum tilt angle. The camera is fixed on a sturdy adjustable multi-axis camera-mount to enable the adjustment of the camera orientation. The camera-mount is fixed on an optical rail such that the camera can be moved to any desired working distance without interrupting the camera alignment. The target plate is mounted on a multi-axis high-precision translating/rotating stage such that the desired translations/rotations can be performed. An overall view of the experimental setup is shown in Figure 4. To ensure that the camera is perfectly perpendicular to the target surface before the experiments are started, the camera is first brought into contact with the target surface and its orientation is adjusted; then, the camera is retracted back to the desired working distance. The multi-axis stage used for mounting the target plate allows the target to be translated in the *x* and *y* directions and to be rotated about the *y* axis. As can be seen in the figure, two translating stages are allocated for the translation along the *x* direction where one of them is mounted on top of the rotating stage while the other is below. With such setup, the translating stage on top is used to translate the target parallel to its plane, while the bottom stage is used to translate the target parallel to the camera plane. A printed random speckle pattern (black dots on white background) is affixed to the surface of the target plate. The speckle pattern is generated using a software called "Speckle Generator" with the following parameters; 0.4 mm dot diameter, 60% density, and 80% variation. The working distance between the camera and the target is set such that the field-of-view observed by the camera is 100mm wide (this makes the scale factor to be about 26 pixels/mm and the average dot size is about 10 pixels).The magnification level being used here (i.e., 100 mm field-of-view width) is achieved when the working distance is about 307 mm. It should be kept in mind that the working distance being reported here (i.e., the distance from the front end of the lens body to the target surface) is smaller than the stand-off-distance used in the equations for calculating the tilt angle, as will be discussed later.

3.2. Procedure

Different groups of experiments are carried out in order to validate the proposed approach and evaluate its accuracy in determining the tilt angles. In all the different scenarios being investigated here, the first set of experiments is always performed while the camera is being perfectly perpendicular to the target surface. This done to evaluate the baseline strain error level associated with the imaging system (camera/lens combination) and the DIC setting/parameters [24]. In each of the different groups of experiments, a reference position image is captured, and then other images are captured after the target is translated to different positions. In general, the translations are done in two directions, the *x* direction (i.e., perpendicular to the tilt axis) and the *y* direction (i.e., parallel to the tilt axis). The translation step size for each of the two directions is set to be 5% of the field-of-view width (i.e., 5 mm at the magnification level being used here).

3.2.1. Translations parallel to camera plane

After performing the initial translation experiments while the camera is perpendicular to the target surface, the same translation experiments are repeated after tilting the target at different angles around the *y*-axis starting from 1° up to 4° in 1° steps. In each group of experiments that corresponds to a certain tilt angle, the translation in the *x* direction is made such that it is parallel to the plane of the camera (not the target) where this is achieved by using the top translating stage (see figure 4). As for the translation in the *y* direction, it is done as usual since the *y*-axis is parallel to both the camera plane and the target plane (since it is the tilt axis). In each of the two directions (*x* and *y*), the target is translated in two steps (5mm each); thus, images are recorded for the target at five different positions; a reference position, two positions with translation in the *x* direction, and two positions with translation in the *y* direction.

3.2.2. Translation in two directions simultaneously

In this group of experiments, instead of translating the target along the *x* or *y* directions, the translation is bi-directional such that the translation direction makes an angle with the *x* and *y* axes. As such, the translation will have both an *x* and *y* components at the same time (i.e., the translation is neither parallel nor perpendicular to the *x* or *y* axis, it has an angle with both). Three different angles (measured from the positive *x* axis) are used for the translation which are: 36.9°, 45° and 53.1°. These angular translations are achieved by performing simultaneous translations in the *x* and *y* directions as follows: Δx= 4 mm & Δy= 3 mm (36.9°), Δx= 3 mm & Δy= 3 mm (45°), and Δx= 3 mm & Δy= 4 mm (53.1°). These bi-directional translation experiments are done using translations parallel to the target while the target surface is tilted at 3°.

Table 1. Strain error induced by translation perpendicular to the tilt axis.

Translation direction	Normal strain error in the direction of translation	Normal strain error in the direction perpendicular to translation	Shear strain error
Translation parallel to target plane	$\varepsilon_{xx} \cong \dfrac{2\Delta x \sin\theta}{S+(x_A-\Delta x)\sin\theta}$	$\varepsilon_{yy} = \dfrac{\Delta x \sin\theta}{S+(x_A-\Delta x)\sin\theta}$	$\varepsilon_{xy} = 0$
Translation paralell to camera plane	$\varepsilon_{xx} = \dfrac{\Delta x_c}{S}\tan\theta$	$\varepsilon_{yy} = 0$	$\varepsilon_{xy} = 0$

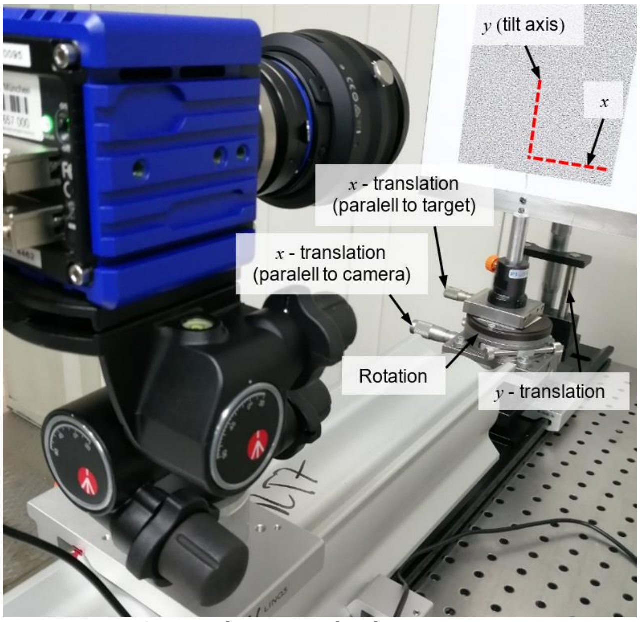

Figure 4. The setup used in the experiments.

3.2.3. Two axes tilting

In this group of experiments, instead of tilting around the vertical axis alone, the target plane is tilted with respect to the camera plane around both the x and *y*-axes. This is done by performing the rotation around the *y* (vertical) axis as usual, while the other rotation is done by tilting the camera about the *x* (horizontal) axis. It should be noted here that performing the rotation about the *x* (horizontal) axis using the camera rather than the target gives basically the same result (it is done this way since the camera is already mounted on a 3-axis rotating stage). The experiment is done at two simultaneous tilt angles of 2° about the y-axis and 1° about the *x* axis. The translations are done (5 mm step as usual) once along the *x* direction and once along they direction.

3.2.4. Small translations

In the previous groups of experiments, the translation step size is set to be 5 mm (i.e., 5% of the field-of-view width); however, a smaller step size is used in this group. Translations are done here starting with a 1 mm step size (1, 2, 3, 5 mm) in the *x* and *y* directions. The experiments are done while the target surface is tilted at 2°.

3.2.5. Different working distance

All the previously mentioned groups of experiments are performed while the working distance is set at 307 mm (from the front end of the lens to the target). To investigate the effect of the working distance on the accuracy of the tilt angles calculated using this approach, two additional groups of experiments are performed at two other values of the working distance. The other two groups of experiments are performed at 197 mm and 417 mm working distance. At 197 mm working distance, the field-of-view width is about 63 mm; while for the 417 mm working distance it is about 137 mm. In order to be comparable with the experiments performed at 307 mm working distance, the steps for the x and y translations are also set to be 5% of the field-of-view width where that gives 3.15 mm and 6.85 mm, for the 197 mm and 417 mm working distances, respectively. The experiments in this group are done while the target surface is tilted at 2°.

3.3. DIC Analysis

For the different groups of rigid-body-translation experiments that are performed here, the reference position image is correlated with the images corresponding to each of the different translated positions. In all experiments, a square region of interest (size of 1600×1600 pixels) located near the center of the image is used in the DIC analysis such that the same number of data points is used in the x and y directions, and thus the same reliability is achieved for the results in both directions. The DIC analysis is performed using the "MatchID-2D" software [38] with the following correlation parameters: normalized cross-correlation algorithm, no image pre-filtering, subset size of 51×51 pixels, step size of 25 pixels, and the "Green-Lagrange" strains are calculated using 7×7 points strain window size.

For the experiments done at different working distance (section 3.2.5), the DIC analysis is performed using different subset size and step size for each case. For the 197 mm working distance, 81×81 pixels subset size and 40 pixels step size are used; while for the 417 mm working distance, 37×37 pixels subset size and 18 pixels step size are used. This is done to maintain the same physical size for the subset and step sizes, since the same speckle pattern is used in all cases while the images have different magnification levels. It might be worth mentioning here that the speckle dot size at the 417 mm working distance is about 7 pixels which is still large enough to avoid any effect of the camera fill-factor on the accuracy of DIC results [26].

4. Results and Discussion

4.1. Translation Parallel to Camera

The approach developed previously by Hijazi [37] uses rigid-body-translations to verify the perpendicularity of the camera's viewing axis with respect to the target surface; and if the camera is not perpendicular, the resulting strain errors are used to determine the surface tilt angle. In this approach, the direction of translation is considered to be parallel to the plane of the target surface, and the translation can be either parallel or perpendicular to the tilt axis. In fact, performing translations that are parallel to the target surface is feasible in most experimental setups and it can be done by translating the target itself using the same actuator that is used for performing the actual experiments. Nevertheless, in some experimental setups it might be more convenient to do the rigid-body-translation to verify the camera perpendicularity by moving the camera itself rather than the target. In such cases, the camera can be mounted directly on a small one-axis translating stage that allows the camera to move in the horizontal or vertical directions, and the camera can be simply aligned with the translating stage. Consequently, the translation of the camera in this case will be parallel to the camera plane. In this study, it is shown that the strain errors resulting from camera non-perpendicularity are quite different when the translation direction is parallel to the target plane or the camera plane (see Table 1). This difference which is observed from the theoretical strain error equations is further verified experimentally and the results are shown in Figure 5. It is probably worth to mention here that the strain values shown in the figure are the mean values, which are calculated over the entire region of interest used in the DIC analysis. In Figure 5 (a) it can be seen that for a translation perpendicular to the tilt axis and parallel to the target plane, when the camera is not perpendicular to the target, error will be induced in both normal strain components (ε_{xx} and ε_{yy}) while the shear strain (ε_{xy}) is practically not affected. However, as can be seen in Figure 5 (b), when the translation is parallel to the camera plane, error will be induced only in the normal strain component along the direction of translation (ε_{xx}) while the other strain components (ε_{yy} and ε_{xy}) are practically not affected. The theoretical values of the strain error (represented by the solid line) are also shown in the figure for each case, and it can be seen that the experimental results are generally in good agreement with the theoretical values. When the translation is parallel to the target plane, the tilt angle can be calculated based on either ε_{xx} orε_{yy} using equation (1) or (2). It is generally preferable to use equation (1) and calculate the tilt angles based on theε_{xx} error since the ε_{xx} value is larger, thus it is expected to yield results that are more accurate. On the other hand, when the translation is parallel to the camera plane, error will only be induced in ε_{xx} and the tilt angle can be calculated using equation (13). It is important here to notice the big difference in the resulting ε_{xx} error between the two cases where ε_{xx} for the translation parallel to the camera is basically equal to half of that when the translation is parallel to the target. As a matter of fact, this observation calls for caution when using the proposed approach to determine the tilt angles where the experimental setup has to be carefully set to produce translations that are either parallel to the target plane or the camera plane. If the experimental setup is not set correctly and the translation is neither parallel to the target nor the camera, then both equations (1) and (13) will give incorrect tilt angle values. However, it is worth mentioning that even though the equations cannot give the correct value of the tilt angle, the proposed approach can still be used to check whither the camera is perpendicular to the target surface or not by comparing the values of the mean strain error $((1/N)\sum\varepsilon)$ and the mean of the absolute values of strain $((1/N)\sum|\varepsilon|)$. When these two strain error measures have similar magnitudes, this indicates that the camera is not perpendicular to the target surface [36].

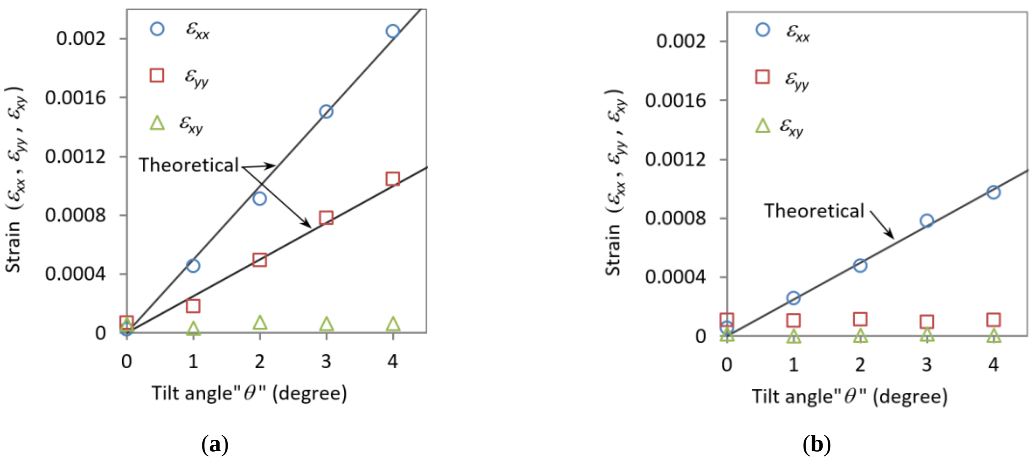

Figure 5. Comparison of the effect of translation direction on strain error (for translations perpendicular to tilt axis): (**a**) Translation parallel to target (Δx = 5 mm), (**b**) Translation parallel to camera (Δx_c = 5 mm).

A graphical comparison of the tilt angles calculated based on translation parallel to the camera plane (using equation 13) with the actual tilt angles is shown in Figure 6. The dashed 45° line shown in the figure represents the equality of the calculated and the actual tilt angle values. In this type of figure, a point above the dashed 45° line indicates that the calculated value is larger than the actual value, while a point below the dashed 45° line indicates that the calculated value is smaller than the actual value. The figure shows the predicted tilt angle values obtained using 5 mm and 10 mm translations, and it can be seen that the calculated tilt angle values are generally in good agreement with the actual tilt angle values. By closely inspecting the results shown in the figure, it can be observed that there is no advantage in terms of accuracy when using larger translation (10 mm). On the contrary, the calculated tilt angle values obtained using 5 mm translation seems to be slightly more accurate. In fact, this observation is actually in agreement with the results presented previously by Hijazi [37], and this is most likely to be attributed to the use of small strains theory in developing the theoretical strain error equations, while the strains measured by DIC become relatively large as the magnitude of translation increases.

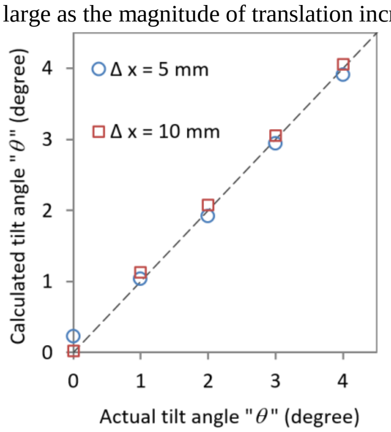

Figure 6. Tilt angles calculated based on normal strain ε_{xx} resulting from translation parallel to the camera plane compared with the actual tilt angles.

4.2. In-plane Translations at an Angle

When performing measurements using any 2D-DIC software, the *x* and *y* directions are typically defined relative to the reference image. By default, the *x* axis is defined in the horizontal direction of the image, and the *y* axis is defined in the vertical direction of the image. It is usually a good experimental practice to align the camera such that the direction of translation of the test specimen is along either the vertical or the horizontal directions of the image (usually the horizontal, since it is larger). As such, it will be possible to translate the specimen along the *x* or *y* directions to verify the camera perpendicularity using the proposed approach before running the actual experiments. However, in some cases it might not be possible to perform a translation along either the *x* or *y* directions, and the translation has to be in some arbitrary (in-plane) direction such that it includes both *x* and *y* components.

The approach presented by Hijazi [37] suggests the use of rigid-body-translations that are in either the *x* or *y* directions. The case where the translation is performed in some arbitrary (in-plane) direction such that it has both *x* and *y* components is considered in this investigation. It should be noted here that such translation in an arbitrary direction is basically a combination of simultaneous Δx and Δy translations. When the camera is not perpendicular to the surface, normal strain error will be induced due to translation in the *x* direction; and when the translation is in the *y* direction, shear strain error will be induced. Thus, both normal and shear strain errors will be induced as a result of a translation having both *x* and *y* components. However, the fact that the strain error equations for *x* and *y* translations are uncoupled (since the *x* translation does not result in shear strain error, and the *y* translation does not result in normal strain error) makes it theoretically possible to use the same existing equations to determine the tilt angle when the translation has both *x* and *y* components. In such case, the tilt angle can be calculated using equation 1 (or equation 2) based on the Δx component of the translation, or it can be calculated using equation 3based on the Δy component of the translation. As mentioned in *section 3.2.2,* the experiments included translations at three different in-plane angles where these angular translations are achieved using simultaneous *x* and *y* translations. It might be worth noting here that the total translation for the 45° case is 4.24 mm (Δx= 3 mm & Δy= 3 mm) while the total translation for the 36.9° and 53.1°cases is 5 mm (Δx= 4 mm & Δy= 3 mm or Δx= 3 mm & Δy= 4 mm). Figure 7 shows the calculated tilt angles for the three cases where the angle for each case is calculated twice, once using equation 1 (based on Δx) and once using equation 3 (based on Δy). For each of these cases, the two equations should theoretically give the same value of the tilt angle. However, as can be seen in the figure, the tilt angles calculated based on the Δx component of the translation are consistently lower than those calculated based on the Δy component. It can also be noted from the figure that the tilt angles calculated based on the Δy component (using ε_{xy}) are fairly close to the actual tilt angle value where the error is about 0.1°, while the error increases to about 0.4° for the tilt angles calculated based on the Δx component (using ε_{xx}). While an error of about 0.4° is not considered to be very high and it might still be acceptable, the fact that it is almost consistent for the three cases might suggest that the simultaneous Δy component of the translation might be somehow slightly affecting the normal strain ε_{xx} error (though the simple theoretical equations being used here do not capture such effect). It might also be likely that this effect is due to the optical aberrations, which generally have more effect on normal stains error than the shear strain error. Regardless of the reason, why such difference between the angles calculated based on normal strain or shear strain is observed; based on the results presented in Figure 7, it is suggested to rely on the shear strain error for calculating the tilt angle for cases of simultaneous *x* and *y* translations.

In real life, scenarios where the direction of translation of the test specimen is not aligned with the image axis, the magnitude of the *x* and *y* components of the translation are not directly known. In such case, the total translation is usually known, and the angle of the translation (with respect to the reference image *x*-axis) can be obtained by comparing the reference and translated images. Based on that, the *x* and *y* components of the translation can be obtained and thus used to calculate the tilt angle.

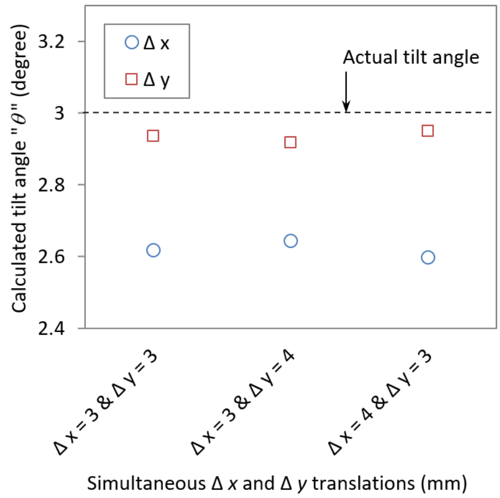

Figure 7. Tilt angles calculated based on the Δx component (using ε_{xx}) and the Δy component (using ε_{xy}) for simultaneous *x* and *y* translation (translation at an angle).

4.3. Two-Axes Tilting (Arbitrarily Oriented Tilt Axis)

The proposed approach assumes that the tilt axis is aligned with the *y* axis (the vertical axis), see Figure 1. In fact, in most cases where 2D-DIC is used, the test specimen (the target surface) will be oriented vertically upwards while the camera is oriented horizontally in order to observe the surface of the specimen perpendicularly. Theoretically, a misalignment might also exist in the vertical or horizontal placement of the specimen or the camera, and thus the target surface can be tilted about the *x* axis. However, from a practical perspective, such misalignment is not of a big concern since it can easily be avoided by using a level-meter (or inclinometer) for checking the horizontal and vertical alignment of the camera and the specimen (nowadays inclinometers are even available as apps for smart phones). Thus, the most concern remains to be about the misalignment (or tilting) about the *y* axis since there is no direct and easy way for detecting such misalignment, and this is where the proposed approach is most useful. Though the proposed approach is mainly focused on the detection of tilt angels about the *y* axis; however, it still can be used for cases where the target surface is tilted about both the *x* and *y* axis. While such case is not very common in experimental mechanics; however, it is worth to be addressed. From a geometric viewpoint, if a surface it rotated about both the *x* and *y* axes, these two rotations can be represented as a single rotation about a new in-plane axis that is neither parallel to *x* nor *y*. While the orientation of this arbitrarily oriented axis, and its tilt angle can be calculated, this is not of concern in our case. Representing any rotation about an arbitrarily oriented in-plane tilt axis through its *x* and *y* rotation components is more useful from the practical point of view, since the *x* and *y* axes represent unique directions that are defined with reference to the camera images. The essence of using the proposed approach for calculating the tilt angles about both the *x* and *y* axes originates from the fact that the strain errors resulting from translation in the *x* and *y* directions are uncoupled (meaning that a translation in the direction perpendicular to the tilt axis causes normal strain error only while a translation in the direction parallel to the tilt axis causes shear strain error only). Therefore, if a translation is performed in the *x* direction while the surface is tilted about both the *x* and *y* axes, this will result in both normal and shear strain errors. The normal strain error ε_{xx} can be used to calculate the tilt angle about the *y* axis (i.e., the axis perpendicular to the translation), while the shear strain error ε_{xy} can be used to calculate the tilt angle about the *x* axis (i.e., the axis parallel to the translation). The tilt angle about the *y* axis is directly calculated using equation 1. However, the tilt angle about the *x* axis is calculated using equation 3 but the Δy in the equation is replaced with Δx (i.e., $\theta_{/\!/} = \tan^{-1}[2\varepsilon_{xy}S/\Delta x]$) since Δx now represents the translation in the direction parallel to the tilt axis. Similarly, if a translation is performed in the *y* direction (instead of the *x* direction), the normal strain error ε_{xx} can be used to calculate the tilt angle about the *x* axis (using equation 1 after replacing Δx with Δy), while the shear strain ε_{xy} error can be used to calculate the tilt angle about the *y* axis (using equation 3). Figure 8 shows the calculated tilt angles about *x* and *y* axes based on *x* direction translation and *y* direction translation. It can be seen from the figure that both the *x* and *y* axes' tilt angles can be calculated with reasonable accuracy (error of less than 0.3°) using a translation in either the *x* or *y* directions. Closer inspection of the calculated tilt angle values shows that for the Δx translation, the *x* axis tilt angle is obtained with higher accuracy than the *y* axis tilt angle. The opposite is also true for the Δy translation where the *y* axis tilt angel has higher accuracy than the *x* axis tilt angle. It should be noted here that the cases where the tilt angles have higher accuracy are those where the shear strain ε_{xy} is used for calculating the tilt angles. This observation is actually consistent with that seen in section 4.2 where this again suggests that the shear strain ε_{xy} is indeed not affected by the translation in the direction perpendicular to the tilt axis. On the other hand, the translation in the direction parallel to the tilt axis apparently has a small effect on the normal strain ε_{xx}, and this causes the slightly higher error for the tilt angles calculated based on the normal strain. While this observation might suggest that the proposed approach is not very accurate when dealing with cases where there is tilting about two axes, this issue can be easily overcome. In order to overcome this issue and to obtain more accurate estimates for both the *x* and *y* axes tilt angles, instead of doing one translation (in the *x* or *y* directions), two translations need to be done once in the *x* direction and once in the *y* direction. As such, the shear strain obtained from the Δx translation can be used for calculating the *x* axis tilt angle accurately, and the shear strain obtained from the Δy translation can be used for calculating the *y* axis tilt angle accurately.

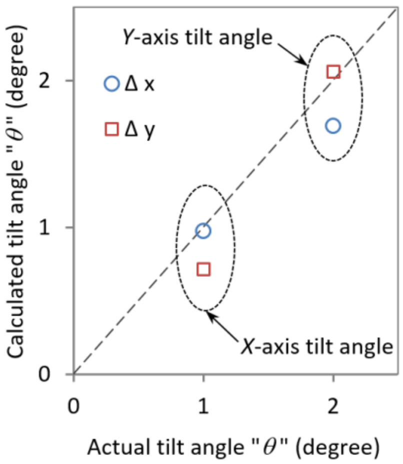

Figure 8. Tilt angles about the *x* and *y* axes calculated using Δx translation and Δy translation.

4.4. Small Translations

The normal and shear strain bias resulting from camera non-perpendicularity are proportional to the magnitude of the rigid-body-translation [37]. In the proposed approach, the strain errors obtained from DIC analysis are used to calculate the tilt angle(s). From theoretical point of view, when the magnitude of strain bias is higher it becomes less affected by the random strain error. Thus, it is expected that a larger magnitude of rigid-body-translation results in more accurate tilt angles. However, it was previously shown that a 5 mm translation (5% of the field-of-view width) results in more accurate tilt angle predictions than larger (10 mm and 15 mm) translations [37]. In this study, the use of rigid-body-translations smaller than 5 mm is investigated to determine if smaller translations can be used for determining the tilt angle with reasonable accuracy. Figure 9shows the tilt angles calculated using small translations in the *x* or *y* directions. Form the figure it can be seen that translations as small as 2 mm (2% of the field-of-view width) can still be used for obtaining the tilt angles with reasonable accuracy. As the magnitude of the translation increases, the accuracy of the calculated tilt angles seems to show a slight improvement. The results shown in the figure suggests that 5 mm translation is probably the most suitable, though translations smaller than 5 mm can be used if necessary.

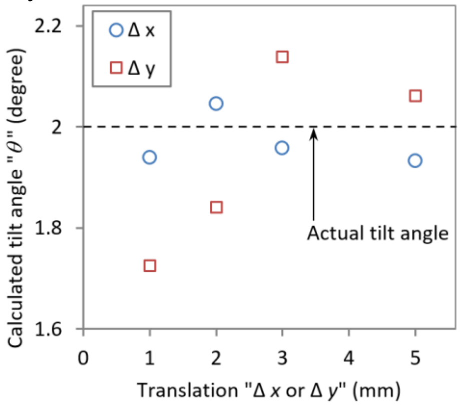

Figure 9. Tilt angles calculated using small Δx and Δy translations.

4.5. Stand-off-distance

The equations being used here to determine the tilt angle(s) are developed based on the pinhole camera model. In a real imaging system, the stand-off-distance (*S*), see Figure 2, represents the distance from the pinhole plane (or the lens mid-thickness if a lens is used) to the target surface. The working distance for a lens is measured from the front end of the lens body to the surface being observed. Multi-element lenses, which are typically used in imaging systems, could be relatively thick sometimes. Determining the exact "optical" mid-thickness plane for a multi-element lens requires the use of some specialized setup. However, the location of the mid-thickness plane for a multi-element lens can be roughly estimated based on physical measurement of the overall thickness of the lens elements. Such approximation of the mid-thickness plane based on physical measurements should be sufficiently accurate for the purpose of estimating the tilt angles using the proposed approach. When determining the tilt angles using any of the equations presented here, the lens working distance has to be augmented by the distance from the lens front end to its mid-thickness. In previous studies [36, 37], 10 mm was added to the lens working distance in order to obtain the stand-off-distance used in the calculations. For the lens used in this investigation, based on the physical measurements, the lens mid-thickness is estimated to be at distance of about53 mm from the front end of the lens body. Therefore, for the experiments performed at 307 mm working distance, the stand-off-distance used in the calculations is 307 + 53 = 360 mm. Similarly, for the other two groups of experiments performed at 197 mm and 417 mm working distance, the stand-off-distance used in the calculations are 250 mm and 470 mm, respectively. Figure 10 shows the calculated tilt angles for three groups of experiments performed at different working distances while the target is tilted at 2°. The figure shows the tilt angles calculated using translations in the *x* direction and the *y* direction where in each case the magnitude of the translation is 5% of the field-of-view width (see *Section 3.2.5*). For each of the calculated tilt angle values shown in the figure, the error bars are also shown. These error bars show the upper and lower limit of the calculated tilt angle values. These upper and lower limit values are obtained by varying the value of the stand-off-distance (*S*) used in the calculations by ±10 mm. From the figure it can be seen that the proposed approach is able to predict the tilt angle with comparable accuracy for the three groups of experiments corresponding to the different stand-off-distance values. The shown error bars for *S* ±10 mm demonstrate that the calculation of the tilt angle is actually sensitive to the value of the stand-off-distance used in the calculation, and it even becomes more sensitive when the stand-off-distance is smaller (e.g., compare the error bars for the 250 mm and 470 mm cases). Therefore, for a lens such as the one that is being used in this investigation, if the working distance is not augmented by the 53 mm, a large error will be introduced in the calculated tilt angles.

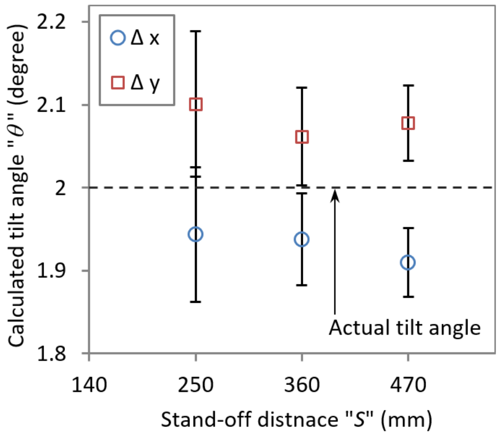

Figure 10. Tilt angles calculated using Δx and Δy translations for experiments performed at different distance from the target (error bars corresponding to S ±10 mm are shown).

5. Concluding remarks

When using the 2D-DIC technique, the camera needs to observe the target surface perpendicularly. If the camera is not perpendicular to the surface, errors will be introduced in both the displacements and strains measured by DIC analysis. Therefore, in experiments where 2D-DIC is to be used, it is imperative to ensure that the camera is properly oriented before starting to make measurements using 2D-DIC. This paper reports on the development of a novel generalized approach for verifying the camera perpendicularity; and if the camera is not perpendicular to the surface, the tilt angle(s) are calculated using this approach. This approach is designed to be performed as an initial setup/calibration procedure before starting to use 2D-DIC in the actual experiments. The tilt angle(s) obtained using this approach may be either used for correcting the camera alignment or, if the alignment cannot be corrected due to some physical limitations, for rectifying the images before they are used for DIC in the actual experiments. The approach is based on performing a simple rigid-body-translation experiment and running DIC analysis to find the strain error(s) caused by camera non-perpendicularity; from that, the tilt angle(s) are calculate using simple analytical equations. Several validations experiments representing different practical scenarios are carried out and the results show that the proposed approach is capable of obtaining the tilt angle(s) with good accuracy. The major conclusions of this study are summarized in the following points:

- When the camera is not perpendicular to the surface, in general, a translation in the direction perpendicular to the tilt axis causes normal strain error (bias), while a translation in the direction parallel to the tilt axis causes shear strain error (bias). The sense of the resulting strain bias depends on the direction of the translation (reversing the direction of translation will reverse the sign of the strain error). As for the magnitude of the resulting strain bias, it mainly depends on three factors: i) the tilt angle, ii) the magnitude of translation, and iii) the distance between the camera and the surface.
- The rigid-body-translation needs to be either parallel to the target plane or parallel to the camera plane. Translation parallel to the target plane can be done by moving the target (this is generally recommended), while the translation parallel to the camera plane can be done by moving the camera itself. Different strain errors are observed in each of the two cases and thus different equations are used for calculating the tilt angle(s) in each case. A translation perpendicular to the tilt axis and parallel to the target plane will cause bias in the two normal stress components (ε_{xx} and ε_{yy}), while it will cause bias only in ε_{xx} (i.e., the normal strain in the direction of translation) when it is parallel to the camera plane.
- A single rigid-body-translation in any in-plane direction is all what is needed to determine the tilt angle(s) using this approach. It is preferred to do the translation along the horizontal or vertical directions of the camera image (i.e., the x or y directions). If necessary, it is also possible to do the translation at an arbitrary in-plane direction (neither parallel nor perpendicular to x and y). In this case, errors will be introduced in both the normal and shear strains, and the angle of translation can be obtained from the images (the angle is used to calculate the x and y components of the translation). Though, theoretically, the tilt angle can be calculated using the normal or shear strain bias, the experiments show that using ε_{xy} gives more accurate results.
- This approach is mainly concerned with cases where the camera/target is tilted about the vertical axis (since alignment with respect to the horizontal axis can easily be verified using simple instruments such as an inclinometer). However, it can also be used for cases where there is tilting about both the x and y axes. In such case, theoretically, a single translation in one direction (x or y) is sufficient for calculating the two tilt angles. But experimental results show that the tilt angles calculated based on the shear strain are more accurate than those calculated based on the normal strain. Thus, it is recommended to do translations in both the x and y direction and use ε_{xy} to calculate the two tilt angles.
- The experiments show that using large magnitude of rigid-body-translation is not necessary for attaining results with good accuracy. A translation equal to 5% of the field-of-view width is found to give good results for all the scenarios that were investigated. If necessary, smaller translations down to 2% of the field-of-view width can be used while maintaining good accuracy for the approach.
- Accurate measurement of the distance between the camera and the target is essential for obtaining good results using this approach. The strain bias resulting from camera non-perpendicularity is inversely related to the stand-off-distance (S). Thus, the smaller the distance between the camera and the target becomes, the more sensitive the results become to small variations in the value of S. The stand-off-distance used in the tilt angle calculation equations is slightly larger than the measured distance between the front end of the lens body and the target surface (i.e., the working distance). For typical small size machine-vision lenses, adding 10 mm to the working distance gives a good approximation for the stand-off-distance. However, for some lenses such as the high-end lens used in this study, larger numbers has to be added to the working distance (based on physical measurements, 53 mm is used for this lens).

Acknowledgements

The author would like to acknowledge the financial support provided by the German research foundation (DFG) for his research visit to Munich Bundeswehr University. The experiments were done in the facilities of the institute of fluid mechanics and aerodynamics at UniBW.

References

[1] Sutton, M. A., Orteu, J. J., & Schreier, H. (2009). Image correlation for shape, motion and deformation measurements: basic concepts, theory and applications. Springer: New York.

[2] Hild, F., & Roux, S. (2006). Digital image correlation: from displacement measurement to identification of elastic properties–a review. Strain, 42(2), 69-80.

[3] Pan, B., Qian, K., Xie, H., & Asundi, A. (2009). Two-dimensional digital image correlation for in-plane displacement and strain measurement: a review. Measurement science and technology, 20(6), 062001.

[4] Orteu, J. J. (2009). 3-D computer vision in experimental mechanics. Optics and lasers in engineering, 47(3-4), 282-291.

[5] Baqersad, J., Poozesh, P., Niezrecki, C., & Avitabile, P. (2017). Photogrammetry and optical methods in structural dynamics–a review. Mechanical Systems and Signal Processing, 86, 17-34.

[6] Hassan, G. M. (2021). Deformation measurement in the presence of discontinuities with digital image correlation: A review. Optics and Lasers in Engineering, 137, 106394.

[7] Niu, Y., Wang, J., Shao, S., Wang, H., Lee, H., & Park, S. B. (2018). A comprehensive solution for electronic packages' reliability assessment with digital image correlation (DIC) method. Microelectronics Reliability, 87, 81-88.

[8] Liljenhjerte, J., Upadhyaya, P., & Kumar, S. (2016). Hyperelastic strain measurements and constitutive parameters identification of 3d printed soft polymers by image processing. Additive Manufacturing, 11, 40-48.

[9] Hijazi, A., Yardi, N., & Madhavan, V. (2004). Determination of forming limit curves using 3D digital image correlation and in-situ observation. Proceedings of the International SAMPE Symposium and Exhibition, Long Beach, CA, 16-20.

[10] Caminero, M. A., Lopez-Pedrosa, M., Pinna, C., & Soutis, C. (2013). Damage monitoring and analysis of composite laminates with an open hole and adhesively bonded repairs using digital image correlation. Composites Part B: Engineering, 53, 76-91.

[11] Feng, D., & Feng, M. Q. (2016). Vision-based multipoint displacement measurement for structural health monitoring. Structural Control and Health Monitoring, 23(5), 876-890.

[12] Cuadra, J., Vanniamparambil, P. A., Hazeli, K., Bartoli, I., & Kontsos, A. (2013). Damage quantification in polymer composites using a hybrid NDT approach. Composites Science and Technology, 83, 11-21.

[13] Eshtayeh, M., Hijazi, A., & Hrairi, M. (2015). Nondestructive evaluation of welded joints using digital image correlation. Journal of Nondestructive Evaluation, 34(4), 1-12.

[14] Pan, B., Tian, L., & Song, X. (2016). Real-time, non-contact and targetless measurement of vertical deflection of bridges using off-axis digital image correlation. Ndt & E International, 79, 73-80.

[15] Libertiaux, V., Pascon, F., & Cescotto, S. (2011). Experimental verification of brain tissue incompressibility using digital image correlation. Journal of the mechanical behavior of biomedical materials, 4(7), 1177-1185.

[16] Soltani, A., Curtze, S., Lahti, J., Järvelä, K., Laurikka, J., Hokka, M., & Kuokkala, V. T. (2018). Digital image correlation study of the deformation and functioning of the human heart during open-heart surgery. In Mechanics of Biological Systems, Materials and other topics in Experimental and Applied Mechanics, Volume 4 (pp. 19-27). Springer, Cham.

[17] Sutton, M. A., Li, N., Joy, D. C., Reynolds, A. P., & Li, X. (2007). Scanning electron microscopy for quantitative small and large deformation measurements part I: SEM imaging at magnifications from 200 to 10,000. Experimental mechanics, 47(6), 775-787.

[18] Rahman, F., Ngaile, G., & Hassan, T. (2021). Optimized stereo digital image correlation setup for miniature round specimen: framework development and implementation. Optics and Lasers in Engineering, 144, 106555.

[19] Kirugulige, M. S., Tippur, H. V., & Denney, T. S. (2007). Measurement of transient deformations using digital image correlation method and high-speed photography: application to dynamic fracture. Applied optics, 46(22), 5083-5096.

[20] Hijazi, A., & Madhavan, V. (2008). A novel ultra-high speed camera for digital image processing applications. Measurement Science and Technology, 19(8), 085503.

[21] Berke, R. B., & Lambros, J. (2014). Ultraviolet digital image correlation (UV-DIC) for high temperature applications. Review of Scientific Instruments, 85(4), 045121.

[22] Bornert, M., Brémand, F., Doumalin, P., Dupré, J. C., Fazzini, M., Grédiac, M., ... & Wattrisse, B. (2009). Assessment of digital image correlation measurement errors: methodology and results. Experimental mechanics, 49(3), 353-370.

[23] Haddadi, H., & Belhabib, S. (2008). Use of rigid-body motion for the investigation and estimation of the measurement errors related to digital image correlation technique. Optics and Lasers in Engineering, 46(2), 185-196.

[24] Hijazi, A., & Kähler, C. J. (2017). Contribution of the imaging system components in the overall error of the two-dimensional digital image correlation technique. Journal of Testing and Evaluation, 45(2), 369-384.

[25] Zhu, H., Liu, X., Chen, L., Ma, Q., & Ma, S. (2018). Influence of imaging configurations on the accuracy of digital image correlation measurement. Measurement Science and Technology, 29(3), 035205.

[26] Hijazi, A., Rawashdeh, N. & Kähler, C. J. (2019). Effect of Camera's Focal Plane Array Fill Factor on Digital Image Correlation Measurement Accuracy. Proceedings of the 5th International Conference on Advances in Mechanical Engineering, Istanbul-Turkey, 537-545.

[27] Chu, T. C., Ranson, W. F., & Sutton, M. A. (1985). Applications of digital-image-correlation techniques to experimental mechanics. Experimental mechanics, 25(3), 232-244.

[28] Sutton, M. A., Yan, J. H., Tiwari, V., Schreier, H. W., & Orteu, J. J. (2008). The effect of out-of-plane motion on 2D and 3D digital image correlation measurements. Optics and Lasers in Engineering, 46(10), 746-757.

[29] Siddiqui, M. Z. (2015). Towards Eliminating the Displacement Bias Due to Out-Of-Plane Motion in 2D Inverse Problems: A Case of General Rigid-Body Motion. Strain, 51(1), 55-70.

[30] Pan, B., Yu, L., & Wu, D. (2013). High-accuracy 2D digital image correlation measurements using low-cost imaging lenses: implementation of a generalized compensation method. Measurement Science and Technology, 25(2), 025001.

[31] Badaloni, M., Lava, P., Rossi, M., Chiappini, G., & Debruyne, D. (2016). Out-of-plane motion evaluation and correction in

2D DIC. In Advancement of Optical Methods in Experimental Mechanics, Volume 3 (pp. 181-187). Springer, Cham.

[32] Halding, P. S., Christensen, C. O., & Schmidt, J. W. (2019). Surface rotation correction and strain precision of wide-angle 2D DIC for field use. Journal of Bridge Engineering, 24(4), 04019008.

[33] Meng, L., Jin, G., & Yao, X. (2006). Errors caused by misalignment of the optical camera axis and the object surface in the DSCM. Journal of Tsinghua University, 46(11), 1930.

[34] Lava, P., Coppieters, S., Wang, Y., Van Houtte, P., & Debruyne, D. (2011). Error estimation in measuring strain fields with DIC on planar sheet metal specimens with a non-perpendicular camera alignment. Optics and Lasers in Engineering, 49(1), 57-65.

[35] Wang, L., Chen, Y., Li, H., Kemao, Q., Gu, Y., & Zhai, C. (2020). Out-of-plane motion and non-perpendicular alignment compensation for 2D-DIC based on cross-shaped structured light. Optics and Lasers in Engineering, 134, 106148.

[36] Hijazi, A., Friedl, A., & Kähler, C. J. (2011). Influence of camera's optical axis non-perpendicularity on measurement accuracy of two-dimensional digital image correlation. Jordan Journal of Mechanical and Industrial Engineering, 5(4), 373-382.

[37] Hijazi, A. (2020). A Novel Approach for the Determination of Surface Tilt Angles in Two-Dimensional Digital Image Correlation Experiments. Experimental Mechanics, 60(3), 267-282.

[38] MatchID-2D manual: <www.MatchID.org>

JJMIE

Volume 15, Number 5, December. 2021
ISSN 1995-6665
Pages 475 – 482

Jordan Journal of Mechanical and Industrial Engineering

A Machine Learning Approach for Fire-Fighting Detection in the Power Industry

Firas Basim Ismail[1*], Ammar Al-Bazi[2], Rami Hikmat Al-Hadeethi[3], Mathew Victor[1]

[1]*Power Generation Unit, Institute of Power Engineering (IPE), Universiti Tenaga Nasional (UNITEN), 43000 Kajang, Selangor, Malaysia.*
[2]*School of Mechanical, Aerospace and Automotive Engineering, Coventry University, Coventry, CV1 5FB, UK*
[3]*University of Victoria, London, UK*

Received May 21 2021 *Accepted October 31 2021*

Abstract

Coal kept in the coal storage yard spontaneously catches on fire, which results in wastage and can even cause a massive fire to break out. This phenomenon is known as the spontaneous combustion of coal. It is a complex process that has non-linear relationships between its causing variables. Preventive measures to prevent the fire from spreading to other coal piles in the vicinity have already been implemented. However, the predictive aspect before the fire occurs is of great necessity for the power generation sector. This research investigates various prediction models for spontaneous coal combustion, explicitly selecting input and output parameters to identify a proper clinker formation prediction model. Feed-Forward Neural Network (FFNN) is proposed as a proper prediction model. Two Hidden Layers (2HL) network is found to be the best with 5 minutes prediction capability. A sensitivity analysis study is also conducted to determine the influence of random input variables on their respective response variables.

Keywords: Spontaneous combustion of coal, Artificial Neural Network, Clinker Formation Prediction Models, Coal-fired power plant;

1. Introduction

Fire hazard is a real problem in the power industry. Countless lives have been lost in generating electricity and providing energy for everyone. Almost every aspect of the power industry has a fire involved in its processes. Fire cannot be escaped as it is essential for a fully functioning plant that deals with energy daily. The danger is present if steps are not taken and procedures are not followed. It has been a common occurrence for spontaneous combustions of coal in coal mines which is also detrimental to the environment [1-4]. The oil and gas industry has also been plagued with catastrophic events like the Deep water horizon and Piper Alpha. However, it is always important to have counter measures ready in emergencies.

Traditional systems are already in place and have been modernized to the extent that detection systems have been invented to detect minor changes in the parameters created to sense. Countless regulations have been passed, including OSHA to increase safety measures and hold companies accountable for events such as this. However, detection systems are only there for real-time data processing. So, in a fire, the response time for safety teams to react is limited. Sufficient preparation is not present in combating fires occurrences. Depending solely on the second line of defence will not prevent such events from reoccurring. A system needs to be in place at the first line of defence to collect data and analyze it using the detection system.

There is a solution; however, Information Technology has come a long way in overcoming this. Therefore, this study aims to develop a fire predictive intelligent model that uses Artificial Neural Networks to forecast and predict fire occurrences. This model can self-learn and find relationships between different variables.

2. REVIEW ON FIRE PREDICTION MODELING

The spontaneous combustion of coal and gas has been a serious issue that has plagued the industry. This issue needed a way to predict the outcome if such an incident was bound to happen. To achieve a high accuracy prediction, gas samples were studied using statistical analysis, such as rescales range analysis and The Hurst index. The COSMOL Multiphysics software was chosen to simulate the gas concentrations in a 3D model. The numerical software and the 3D image display on MATLABould predict the zone at which spontaneous combustion of coal can occur, the oxidation zone in the mine [1]. Fire destruction in Lebanon's forests has damaged the forests over a very long period. Weather data from the year 2012 was used from a weather station on the northern side of Lebanon. The artificial neural network was used to predict possible fire occurrences [5]. For fire detection in the household, a fuzzy system was employed to predict fire occurrences using smoke, gas, temperature and humidity [6].

Similarly, for fire occurrence in the wildlife of South Africa, a new model was created according to previous

* Corresponding author e-mail: Firas@uniten.edu.my.

models already established, like the McArthur model. Fire rating was chosen based on specific vegetation present in South Africa. Compared to the current Lowveld fire danger rating, it was found that this fire rating model was more accurate in its prediction at 97%, while the Lowveld model was at 93% [7]. For Portugal, periodic data spanning 3 years was chosen to be fed into the neural network. Five neurons were present in the hidden layers, and this particular model obtains a prediction rating of 88.12% [8]. ANN was deployed to forecast the level of methane in the mining industry [9]. Sensors of coal mines were studied to determine the best location for installation and detection. It was concluded that flame and smoke sensors were necessary for greater detection purposes [10]. Fire detection efficiency was studied for subway trains in China. Levels of CO and CO2 needed to be significantly reduced to suppress the fire while measuring the drop in O2 levels [11]. A random forest approach was deployed to study the oxidation of coal and other methods such as the backpropagation method and multiple linear regression. The random forest method was the most accurate, followed by the backpropagation method in predicting the spontaneous combustion of coal [12]. In the pursuit of studying the phenomenon of spontaneous combustion of coal, a new variable was introduced to increase the prediction's reliability further. HLC indicator was used along with new algorithms such as metabolic and artificial bee colony[13]. An intelligent monitoring system to predict boiler tube leak trips at their early stage was developed by authors in [14]. This system was compared with a pure artificial neural network system and hybrid intelligent system for best lead prediction.[15] proposed two Intelligent Early Warning Systems (IEWSs) to detect early warning for steam turbine trips.[16] investigated implementation of ANN for a predictive fault tool for a CFB to facilitate plant operators. The purpose was to identify and narrow down the operational boiler parameters that cause the fault quickly.[17] developed an ANN model with an Adaptive Backpropagation Algorithm (ABPA) for best practice in forecasting long-term load demand of electricity.

The ABPA includes proposing new forecasting formulations that adjust/adapt forecast values, considering the deviation between different behaviours of trained and future input datasets.[18] presented an overview of recent development and research in the power plant sector using intelligent computational tools, including its applications.

However, the above studies did not consider variables, such as the absorbance of carbon dioxide, carbon monoxide and water in the coal and the exact time the spontaneous combustion of coal occurs. Various configurations of the networks, such as different training functions, number of hidden layers, number of neurons in the hidden layer, and different activation functions, were not explored.

This study focuses on the phenomenon occurring in the coal storage yards. Artificial Neural Networks is used to develop a fire predictive intelligent model to forecast and predict fire occurrences. The best configuration of the network is then identified.

3. METHODOLOGY

To develop an intelligent system to predict the spontaneous combustion of coal in the coal storage yard. Three phases are needed to be done step by step. The first phase is to present the design of the coal storage yard, and the second phase includes collecting the relevant data for developing the appropriate ANN. In the last phase, the ANN model will be developed along with the best parameters for the ANN modelling.

3.1. Design Overview of System

The research target of this study is to solve an important issue that plagues the power industry in particular. This issue is to mitigate fire occurrences in the power industry by predicting it accurately using artificial neural networks. The main target of the power industry that this study focuses on is the coal storage yard situated in the heart of the coal-fired power plant. See Figure 1 for the processes involved in a coal-fired power plant.

Figure 2 shows the coal storage yard of a coal power plant. The coal placed here are segregated based on coal type; among the coal types are Pipit, Jambayan, Envirocoal, Melawan and Malinau.

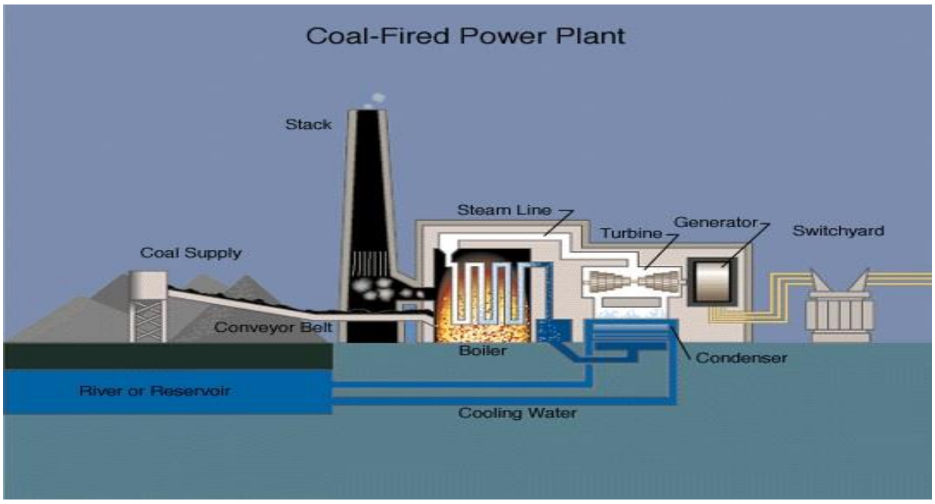

Figure 1. The processes involved in a coal-fired power plant with the input as coal and the output as electricity

They are also separated according to vessel numbers. The total stock accumulated is around 524,555 metric tons of coal. The coal types are separated into three zones: pile E, pile F, and pile G. rejected coins are kept in pile E and pile G, respectively. This specific coal yard resorts to hoses as deterrents to the fire in spontaneous combustion. The hoses are placed every 50 meters as marked by the ruler at the top and bottom of the image. There are no sensors of any type to record fluctuations of either temperature or gas that could cause the coal to comb spontaneously. Therefore, this particular coal power plant will benefit from the prediction tool of the artificial neural network once sensors have been placed at each zones E(top row), F(middle row) and G(bottom row). It is recommended to use gas concentration sensors to record the fluctuations of gasses such as carbon dioxide, carbon monoxide, nitrogen, oxygen, and methane. Temperature and humidity sensors are also required, with the gas sensors placed in each zone of the coal yard storage. This sensor placement helps monitor and feed the data to the network for prediction.

3.2. Data Preparation

Data collection of the gas concentrations is conducted to develop the prediction model for spontaneous combustion of coal formation conditions. All the necessary data obtained is from two separate studies on the spontaneous combustion of coal. The majority of the data is obtained from a study based on the temperature inversion during spontaneous combustion of coal [19].

This study focused on the phenomenon occurring in the coal mines where methane is present. Therefore, those three gasses, mainly ethane, methane, and ethylene, are removed. The second data setconsisting of absorption data of carbon dioxide, carbon monoxide and water were from an article about the characteristics of mass, heat and gaseous products during spontaneous combustion of coal using TG/DSC-FTIR technology [20]. These 3 datasets were chosen to replace the coal content during storage and diversify the input data as an increased amount of data would prevent redundancy for the ANN. See Table 1 for the types and units of the collected data variables.

No	Description	Units
1	Carbon Dioxide	PPM
2	Carbon Monoxide	PPM
3	Nitrogen	%
4	Oxygen	%
5	Absorbance of CO	-
6	Absorbance of CO_2	-
7	Absorbance of H_2O	-
8	Methane	PPM
9	Temperature	ºC
10	Ethane	PPM
11	Ethylene	PPM

Table 1. Data variables collected from previous studies

Data for the artificial neural network was collected from [19,20]. The data collected were then combined to form the inputs of the artificial neural networks. Experimental data to monitor gas concentrations were collected from [19]. A temperature programmed test system for spontaneous combustion of coal in an air bath is used in the experiment. The structure of the system is shown in Figure 3.

The coal samples are loaded into a special cylindrical steel coal sample tank with a bottom diameter of 10 cm and a height of 25 cm using an experimental device. As shown in Figure 3, the experiment begins after sealing. The air is supplied to a coal sample tank at 120 ml/min airflow using an air pump or gas cylinder as a gas source.

The air supplied flows after being preheated by the heating box through a glass rotor flowmeter and gas conveying copper pipe. It then flows to the coal sample via the bottom of the coal sample tank. The gas samples are then retrieved and analyzed by a gas chromatograph, SP-2120, after ½ an hour at a rate of 0.3°C/min. The gas products are finally obtained at different temperature points.

The second tests were carried out using a TG/DSC–FTIR experimental system [20] illustrated in Figure 4.

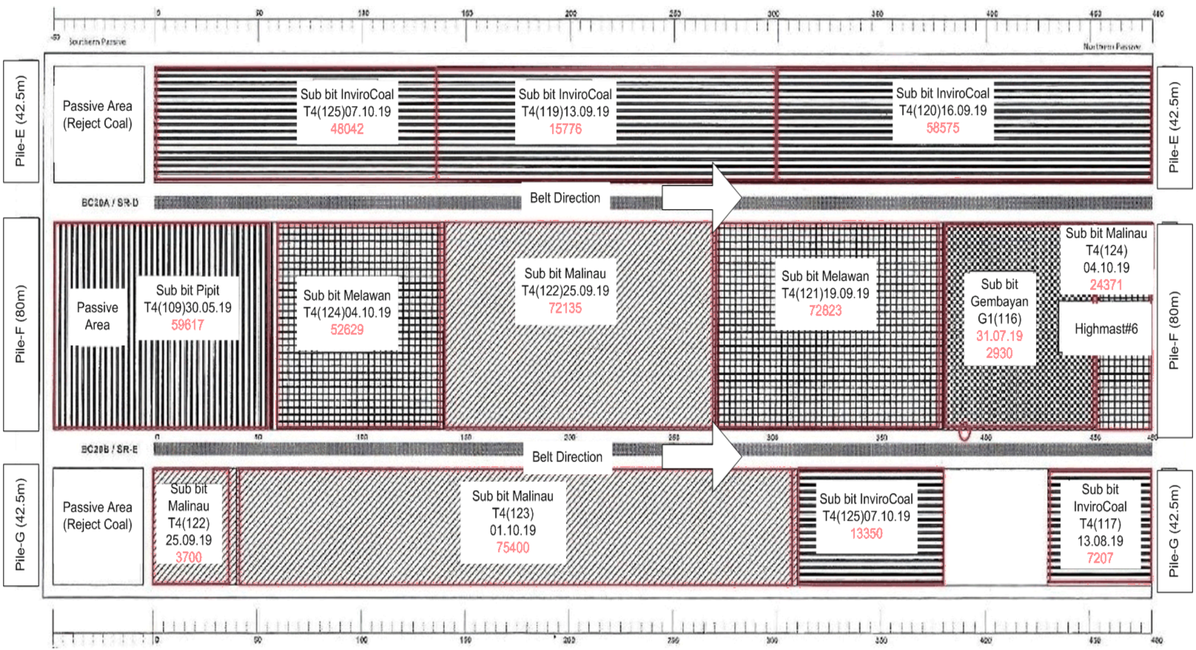

Figure 2. Coal storage yard

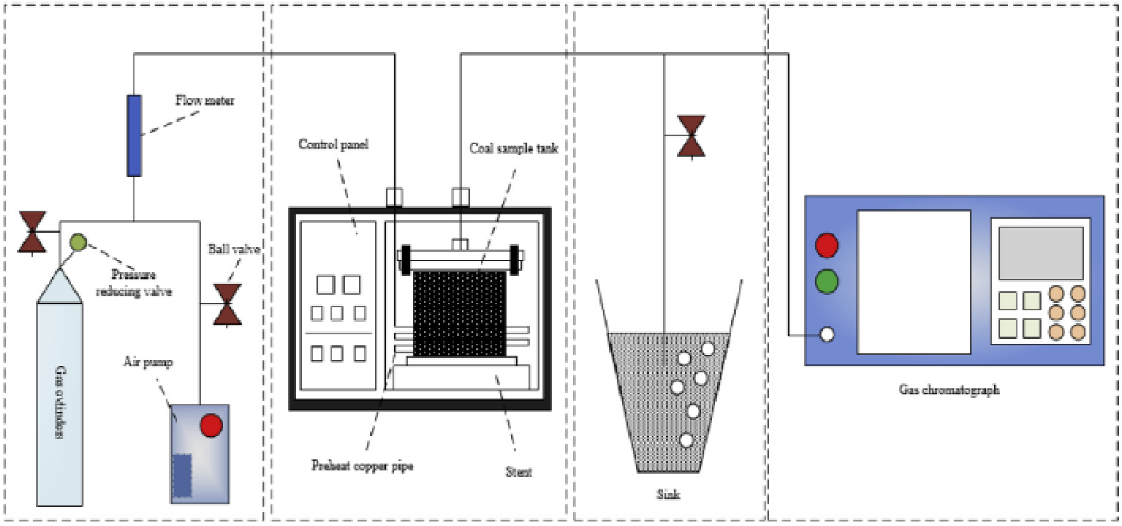

Figure 3. Experiment apparatus used to collect gas concentrations and temperature data [19]

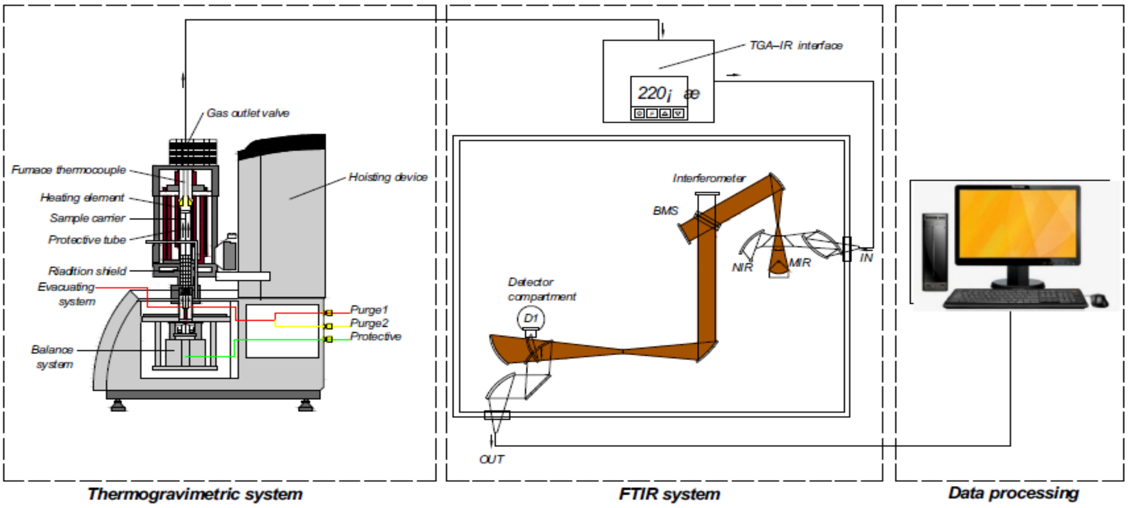

Figure 4. Apparatus used to obtain absorbance data during heating of coal [20, 21]

This experimental system comprises an STA 449 F3 series simultaneous TG/DSC thermal analyzer manufactured by Netzsch Incorporation and a VERTEX70v series Fourier-transform infrared spectrometer (FTIR) manufactured by Brucker Incorporation. A specially designed interface connected these two instruments. The temperature of the interface and the temperature of the transmission lines were kept to be around 220℃ to prevent condensation and structural transformation of oxidation products.

A coal sample of 15-mg was used for each experimental run in the thermal analyzer. The functional groups were measured by delivering the gaseous oxidation in real-time to FTIR during spontaneous combustion. Two factors were changed during the experiments: oxygen concentration and heating rate. The Protection gas used in this experiment was nitrogen, while the carrier gas was a mixture of oxygen and nitrogen with different mixing ratios. The protection and carrier gases' overall flow rate was continuously at 100 mL/min. The parameters set constant for the FTIR were the wavenumber between 400 and 4000cm-1 with a resolution of 4 cm-1.

The data for absorbance was obtained only at 170 ℃ [20]. Various input data like this is much needed for the neural network to learn the non-linear relationships between these variables that contribute to the spontaneous combustion of gas.

3.3. Artificial Neural Network Parameters

The ANN model was developed using MATLAB coding. There are 360 network combinations for the One Hidden Layer (1HL) network and 10,800 network combinations for Two Hidden Layers (2 HL). This combination includes varying the number of neurons, different combinations of activation function and types of the training algorithm. Root Mean Square Error (RMSE) values are compared, and the lowest values are obtained from 1HL and 2HL, respectively.

3.4. Root-Mean Square Error (RMSE)

Root mean square error was used to calculate the difference in the predicted data from the neural network and the actual data from the study itself. This form of error calculation is readily available in MATLAB software and can be easily integrated into the networks coding. The error calculated will be used to determine the reliability of the training system used. This error calculation will be used to identify the accuracy of the network, which can later be rectified by tweaking specific parameters such as hidden layers or even changing the training algorithm. The smaller the error found, the higher the prediction capability of the ANN.

$$RMSE = \sqrt{\sum_{i=1}^{n} \frac{(y_i - y_i)^2}{n}} \quad (1)$$

4. RESULT ANDANALYSIS

In this section, the ANN results will be analyzed and explained further to shed light on this work in particular. The data that has been simulated and the RMSE values using Equation (1)and performance graphs of the best performing networks will be present. The simulated data will be shown in predicted values versus the actual values in a graph. After proceeding with the simulations for the ANN models, the results were tabulated, and a table summary of the best performing combination for each training algorithm in each ANN architecture was made for easier comparison. The best performing ANN prediction model for the 1HL feedforward network is summarized in Table 2 below for the 4 different training algorithms used. The best performing combination of four different training algorithms is highlighted.

4.1. Performance indicators for 1HL Feed-Forward

The best performing ANN prediction model for the 1HL feedforward network is summarized in Table 2 below for the 4 different training algorithms used. The best performing combination among four different training algorithms is highlighted in Table 2.

Table 2. Result summary for 1HL Feed-Forward Neural Network

Training algorithm	1HL Neurons	Activation function	RMSE value
Trainlm	8	T+P	0.1009
Trainbfg	8	P+T	0.1021
Trainscg	9	L+T	0.1053
Trainrp	8	P+T	0.1080

Based on Table 2, the best performing prediction model for the 1HL feedforward network has the training algorithm trainlm at 8 Neurons using the activation function of T+P and producing a value of 0.1009 RMSE. Figure 5 shows the best performance graph for the 1HL feedforward network.

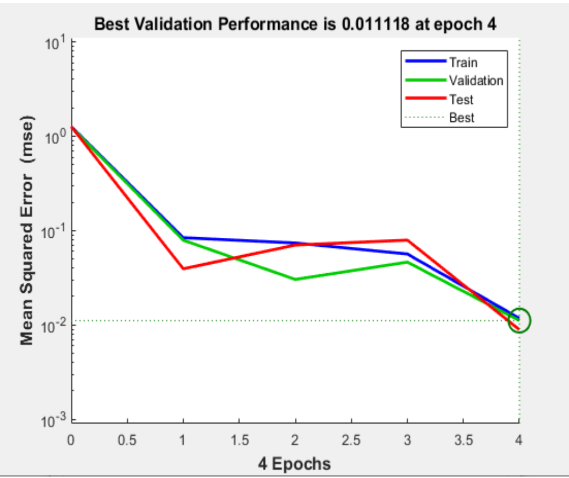

Figure 5. Performance diagram for the best network with 1HL

4.2. Performance indicators for 2HL Feed-Forward

Similarly to 1HL, the results were tabulated, and a table summary of the best performing combination for each training algorithm in each ANN architecture was made for easier comparison. The best performing ANN prediction model for the 2HL feedforward network is summarized in Table 3 below for the 4 different training algorithms used. The best performing combination of four different training algorithms is highlighted.

Table 3. Result summary for 2HL Feed-Forward Neural Network

Training algorithm	1HL neurons	2HL Neurons	Activation function	RMSE value
Trainlm	4	1	L+P+T	0.10000
Trainbfg	10	7	L+P+T	0.10010
Trainrp	7	6	T+P+T	0.10019
Trainscg	4	6	T+P+T	0.10064

Based on Table 3, the best performing prediction model for the 2HL feedforward network has the training algorithm trainlm at four 1st Hidden Layer Neurons, one 2nd Hidden Layer Neurons using the activation function T+T+T and producing a value of 0.1000 RMSE. Figure 6 shows the best performance graph for the 2HL feedforward network.

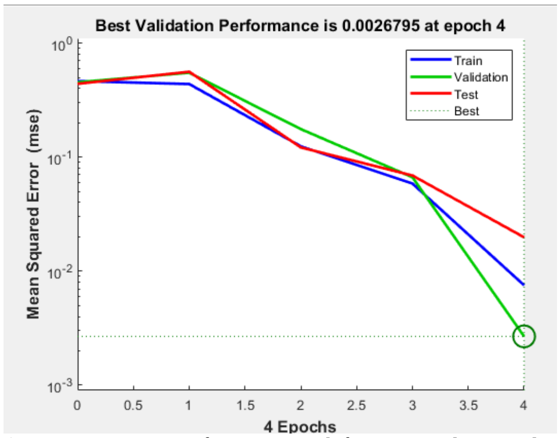

Figure 6. Best MSE performance graph for 2HL Feed-Forward

4.3. Summary of Best ANN Models

This section aims to summarize and analyze the performance of ANN models based on RMSE values. Table 4 below shows the summary for the best RMSE ANN models.

Table Error! No text of specified style in document.**.** Best RMSE ANN models

Type of ANN	Transfer function	1HL neurons	2HL neurons	Activation function	RMSE value
1HL Feed-Forward	Trainlm	8	-	T+P	0.1009
2HL Feed-Forward	Trainlm	4	1	L+P+T	0.1000

Based on Table 4, the 2HL ANN has the lowest RMSE value among 6 different types on the ANN model, although there are minor differences in RMSE value between each model from the 2HL ANN.

4.4. Outcome Analysis

The best performing ANN model has been identified in section 4.3. However, determining the RMSE value for ANN models is only one aspect for determining the performance of an ANN model; it is not sufficient to justify it as the absolute best ANN model for this work. Detailed outcome analysis of the actual and predicted output is essential to justify and supplement the best ANN model for fire prediction.

The graph of actual output versus predicted output is plotted using MATLAB R2019aB version software for the graph of fire occurrence

4.4.1. The First Fire Occurrence Analysis

In this section, the occurrence of fire is investigated. The graphs are highlighted to show the behaviour of the ANN model to produce the required prediction and are provided in Figures 7-8.

Figure 7. The predicted output of 1HL feedforward net

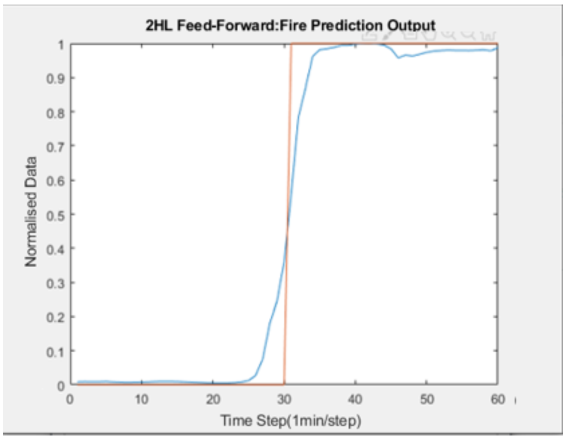

Figure 8. The predicted output of 2HL feedforward net

The points on the graph have been identified by analyzing the actual and predicted output graphs. For easier comparison, each critical point's time step and normalized valuearetabulated in Table 5 below.

Table 5. Comparison of critical points for fire occurrence

Architecture	Normalized Value
1HL feedforward	-0.2 to 1.2
2HL feedforward	0 to 1

Based on Table 5, the normalized value for both models is slightly different. The actual output of the model is either 1 or 0. The model with the closest output to the actual output is the 2 hidden layer feedforward network. The red line represents the actual output when the fire occurs. The time interval is per minute; therefore,a fire occurs at the 30th minute. Although the fire in real life occurs gradually, given the experimental data obtained from the study of the heating coal sample, the fire occurs at the 30th minute when the oxygen levels drop.

When observing the predicted output of the 1 HL feedforward network shown in Figure 7, it can be observed that the overall trend of the output is similar to the actual output. However, slight spikes and dips in the data lead up to the fire when the output becomes 1. This trend is still acceptable; however, the range of normalized values is still far from the actual output of the fire. Ranging from -0.1 to 1.2, this is far from the actual range, either 0 or 1. This network predicts that fire is about to occur at the 28th minute. This prediction shows that this network is not ideal in predicting fire occurrences during the spontaneous combustion of coal.

Figure 8, the 2 hidden layer feedforward network output, is much smoother because it closely follows the actual output value. Although there are dips when the normalized data reaches 1, the changes in the data are minute and will not interfere with the predicted output of the fire. The steady rising of the blue line (predicted output) can also indicate when the fire slowly starts to occur beforehand. The fire can be predicted at the 25th minute from this network, which is very useful for the coal yard personnel to hose down the coal to cool it down before it abruptly catches on fire.

Hence the 2 hidden layer feedforward net is the best network in predicting the outcome of a fire that occurs due to the spontaneous combustion of coal. The value of RMSE alone cannot show whether the network is suitable for a specific problem. The network output should also be analyzed carefully to see how closely it relates to the actual output of the data present.

4.4.2. The Second Fire Occurrence Analysis

A new dataset is sent to the best ANN model for the last test to check its performance. This new data is obtained from the first study as well. Figure 9 shows the predictive output for the second set of data. The type of coal is different, as well as fire occurrence. The fire occurs at the 45th minute based on the sudden spike in carbon dioxide conditions and a sudden decrease in oxygen gas concentrations.

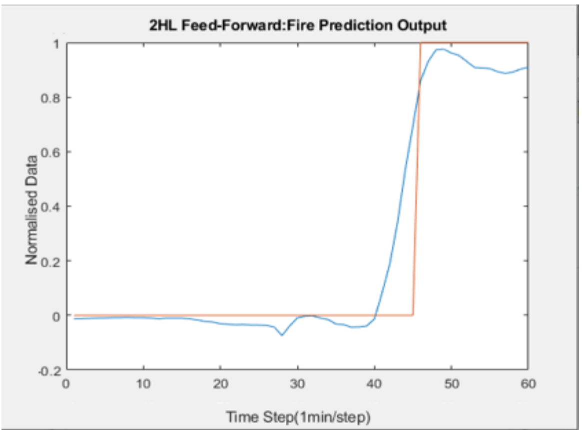

Figure 9. Predictive output for the second set of data

For this second set of data,the fire occurs at the 45th minute, as shown by the sudden increase and decrease of the target concentration of gases, carbon dioxide and oxygen gasses. This network could predict the fire will occur at the 40th minute, again 5 minutes before the actual occurrence. The RMSE value of this data is 0.133, which is very accurate. The acceptable range of RMSE values varies from 0.1 to 0.5. This neural network is suitable for this prediction problem. The blue line may not be smooth; however, the trend line is still present and can still be analyzed.

5. CONCLUSION

Careful research led to the intelligent prediction of spontaneous combustion of coal, and it was evident that ANN plays an essential role in guaranteeing that the objectives are achieved. The objectives of this study were accomplished by determining the best ANN models to predict fire occurrence due to the spontaneous combustion of coal. Also, the input-output relationship of the ANN model has to be identified.

This work focused on examining the output patterns of the model and coming up with the best ANN model to benefit the power plant station. Firstly, the primary input and output parameters were identified, and this parameter identification allowed trial and error progress to determine the best RMSE ANN model. After conducting the simulations, the 2HL feedforward network has the lowest RMSE value out of all the other 4 types of Neural Networks.

Proceeding onward to the outcome analysis, it appeared that the 2HL feedforward network could be used to represent the forecast model for fire best. It is imperative to comprehend the relationship between them so that the input parameters can be modified accordingly to forecast the phenomena of coal spontaneously combusting in the stockpiling yard.

Thus, in utilizing the 2HL feedforward network model, an intelligent prediction system has been built to monitor the coal yard storage and forecast fire occurrences. This model will help the power generation sector achieve a more sustainable and practical business solution, creating a safer working environment.

6. FUTURE WORK

Further study can be carried out to improve the current results using different prediction tools such as Machine Learning or Fuzzy Logic. Other types of artificial intelligence modeling could lead to better performance in prediction than the current ANN models utilized in this study. There are also newer activation functions that can be used instead of the traditional logsin, purelin and tansig functions, and these newer functions may be able to predict at a higher accuracy.

Precise data acquisition on the input and output parameters with a larger variable pool can also be implemented to create a better and accurate model. Increased input that corresponds to the combustion process of the coal should also be included in future work, such as smoke and humidity in the air.

ACKNOWLEDGEMENT

This research was financially supported by Universiti Tenaga Nasional, Malaysia through BOLD refresh publication fund 2021(J510050002-BOLDRefresh2025-Centre of Excellence).

REFERENCE

[1] Y. S. H. X. S. W. S. N. C. J. X. Q. Song Y, "Prediction of gas and coal spontaneous combustion coexisting disaster through the chaotic characteristic analysis of gas indexes in goaf gas extraction" *Process Safety and Enviromental Protection* (2019), p. 29, 12 June 2019.

[2] T. P. T. Glenn B Stracher, "Coal fires burning out of control around the world: thermodynamic recipe for environmental catastrophe," *International Journal of Coal Geology,* vol. 59, pp. 7-17, 2004.

[3] S. J. D. A. S. D. J. W. John N Carras, "Greenhouse gas emissions from low-temperature oxidation at open-cut coal mines in Australia," *International journal of coal geology,* vol. 78, no. 2, pp. 161-168, 2009.

[4] F. O. J. S. Taku Ide, "Comparison of methods to estimate the rate of CO2 emissions and coal consumption from a coal fire near Durango, CO," *International journal of coal geology,* vol. 86, no. 1, pp. 95-107, 2011.

[5] A. H. B. D. a. P. C. N. Hamadeh, "Studying the factors affecting the risk of forest fire occurrence and applying neural networks for prediction," *2015 SAI Intelligent Systems Conference (IntelliSys),* pp. pp. 522-526, 2015.

[6] O. G. a. R. Sarno, "Prototype of fire symptom detection system," *2018 International Conference on Information and Communications Technology (ICOIACT),* pp. pp. 489-494, 2018.

[7] S. L. a. B. Mathibela, "The application of artificial neural networks for wildfire risk prediction," *2016 International Conference on Robotics and Automation for Humanitarian Applications (RAHA),* pp. 1-6, 2016.

[8] M. Sahu, "Integrating Artificial Neural Network," *al. International Journal of Recent Research Aspects,* vol. 2, no. 2, pp. pp. 8-11, June 2015.

[9] T. a. Brodny, "Predicting Methane Concentration in Longwall Regions Using Artificial Neural Networks," *International Journal of Environmental Research and Public Health,* vol. 16, no. 8, p. 1406, April 2019.

[10] R. A. T. J. H. R. a. L. Z. L. Yuan, "Early fire detection for underground diesel fuel storage areas," *Process Safety and Environmental Protection,* vol. 119, p. pp. 69–74, 2018.

[11] X. Z. a. Z.-F. W. W. Zhang, "Experiment Study of Performances of Fire Detection and Fire Extinguishing Systems in a Subway Train," *Procedia Engineering,* vol. 135, p. pp. 393–402, 2016.

[12] J. D. K. C. L. M. Y. X. L. R. Changkui Leia, "A random forest approach for predicting coal spontaneous combustion," *Fuel,* pp. 63-73, 2018.

[13] X. M. C. Y. Shoujun Lia, "Prediction of spontaneous combustion in the coal stockpile based on an improved metabolic grey model," *Process Safety and Environmental Protection,* 2018.

[14] FB Ismail, D Singh, MS Nasif, "Adoption of Intelligent Computational Techniques for SteamBoilers Tube Leak Trip", *Malaysian Journal of Computer Science* 33 (2), 133-151, 2020.

[15] FB Ismail, RIB Ismail, PJ Ker, and SKB Wahidin, "Development of Intelligent Early Warning System for Steam Turbine, *Journal of Engineering Science and Technology (JESTEC)* 14(2), 844 – 858, 2019.

[16] NNM Nistah, KH Lim, L Gopal, FBI Alnaimi, "Coal-Fired Boiler Fault Prediction Using Artificial Neural Networks", *International Journal of Electrical and Computer Engineering (IJECE)* 8 (4), 2018.

[17] NA Mohammed, A Al-Bazi A. "An adaptive backpropagation algorithm for long-term electricity load forecasting". *Neural Computng and Applications* (2021).

[18] FB Ismail, A Al-Bazi, RAL Hadeethi, D Singh, "Application of Intelligent Computational Techniques in Power Plants: A Review", *Advances In Industrial Engineering And Management (AIEM),* 10 (1) (2021), 10-21.

[19] H. W. Y. f. J. Jun Guo, "Data on analysis of temperature inversion during spontaneous combustion of coal," *Data, in brief,* vol. 25, 2019.

[20] H. W. Z. L. C. Jun Guo, "A method for evaluating the spontaneous combustion of coal by monitoring various gases," *Process Safety and environmental protection,* vol. 126, pp. 223-231, 2019.

[21] J. Z. Z. H. L. Z. W. Jun Deng, "Thermal analysis of spontaneous combustion behaviour of partially oxidized coal," *Process Safety and environmental protection,* Vols. 104, Part A, pp. 218-224, 2016.

JJMIE

Volume 15, Number 5, December. 2021
ISSN 1995-6665
Pages 483 – 490

Jordan Journal of Mechanical and Industrial Engineering

Characterization of Al-SiCP Functionally Graded Metal Matrix Composites Developed through Centrifuge Casting Technique

Kiran Aithal S*, Ramesh Babu N, Manjunath HN, Chethan KS

Department of Mechanical Engineering, Nitte Meenakshi Institute of Technology, Karnataka, INDIA, 560064

Received August 31 2020 *Accepted October 29 2021*

Abstract

Centrifuge casting is a new technique wherein a mold assembly is made to rotate at a certain speed that will induce higher 'G' force to the molten metal.The existing higher rotational force creates a compositional gradient that segregate phases with different densities. In this work, an attempt has been made to develop Al alloy/ SiCP FGMs. It has been observed that due to the higher density of SiC compared to Aluminum, the bottom part of the casting is rich in SiC particles with good resistance to wear, and the top of the casting results in high toughness as it is more of Al alloy. In the present work FG Composites are produced using hypereutectic (17%Si) Al-Si alloy using centrifuge casting technique with SiC particulate(SiCP) as reinforcement using stir casting followed by centrifuge casting. The samples were characterized for microstructure, hardness, and wear. It was found that there is a gradation in the sample for all the above said properties from top to bottom of the sample. It was found that Al-17wt% Si matrix alloy reinforced with 2% SiCP yielded a maximum hardness of about 66BHN at 400rpm while for 4% and 6% the hardness was found to be 82 and 94BHN.The results revealed that the wear resistance was high at both the ends of the specimen due to segregation of Si at one end and SiCp at the other end.

Keywords: FG composite, Centrifuge casting, Microstructure, Hardness, Wear;

1. Introduction

High strength, thermal stability, and wear resistance of Aluminum based Metal Matrix Composites (MMCs) in general and particle-reinforced composites are used extensively in the automotive industry. It is well known that increasing the percentage of the SiC_Preinforcement in Metal Matrix Composites (MMCs) increases the overall performance [1-3]. These MMCs, however, do not show improved performance for load bearing applications. Functionally Graded MMCs (FGMMCs) are new class materials intended to eliminate the drawback of the MMCs in which the surface of one side provides higher hardness, but the interior region will have higher resistance towards the crack growth [4]. Because of low dissipation of energy due to the high segregation of reinforced particles at the boundary, the fracture toughness is low for small crack lengths in case of composite system [5-6].

In this study, SiC particle-reinforced Al-Si alloy based FGMMCs have been produced by centrifuge casting process. The developed in-house centrifuge-casting machine operates on vertical axis and pouring of the molten metal is carried while the mold is stationary. The centrifuge casting machine used in the current research work has an arm with metal mold attached at one end which can swing, and counterweight is placed at the other end. The arm is mounted centrally on the output vertical shaft of a0.5HP motor.

The castings were produced at 200, 300 and 400rpm of the mold. The alloy Al-17wt%Si has been used as matrix material with 2, 4 and 6 weight % of SiC_P added as reinforcement to the matrix. The samples were cast at 900°C teeming temperature and mold temperature of 180°C. The graded composites sample were tested for volume fraction and hardness along the length. The wear tests were conducted on the both end surfaces of the casting, which reveals the gradation in the properties [7-9].

2. Methodology

In Aluminum alloys, Silicon is the most common and least expensive alloying element used. Silicon plays an important role in making the alloy suitable for the aerospace and automotive industry. It mainly increases cast ability and fluidity. In addition to lowering of aluminum alloy density to 2.34 g/cm^3 silicon increases strength to weight ratio and wear resistance of aluminum alloy [10-11].

Fenfe Metallurgical, Bangalore, India supplied the commercially available Al alloy. Table 1 represents the composition of the Al alloy used.

Table 1. Composition of Al-Si alloy

Alloy	Composition (wt.%)					
	Si	Fe	Sr	Ti	B	Al
Al-17Si	17	0.1	-	-	-	Balance

* Corresponding author e-mail: kiranaithal_s@yahoo.co.in.

Table 2. Characteristics of Silicon Carbide

Mechanical characteristics	Units	Values
Density	gm/cc	3.18
Poisson's Ratio	—	0.13
Hardness	Kg/mm^2	2700
Purity	%	99
Thermal Conductivity	W/m•°K	120
Coefficient of Thermal Expansion	10^{-6}/°C	4.0

Several researchers have worked on the SiC_P reinforcement in different Aluminum alloys. In this study we have considered SiC_P supplied by M/s Fenfe Metallurgical, Bangalore and we have used volume fractions of 2%, 4%, and 6%. The average size of the SiC_P is 60 microns.

Functionally Graded Metal Matrix Composites (FGMMCs) are produced using centrifuge technique. Due to the difference in density of the materials (ρ_{Al}=2700 kg/m^3, ρ_{Si}=2320 kg/m^3, ρ_{SiC}=3210 kg/m^3) and the rotating speed which implies high centrifugal force on the molten metal, within the liquid Al matrix, volume fraction of the Si and SiC_P reinforcement is gradually increased along the length of the casting. The centrifuge machine is shown in Fig. 3.2. This machine operates on vertical axis and pouring of the molten metal is carried while the mold is stationary. Thus, centrifugal forces are not applied immediately as in the traditional casting methods since the mold takes some time to reach its casting speed. The principal advantage of this is good mold filling combined with micro structural control, which usually results in improved mechanical properties. Author has successfully used this technique to produce Al-Si FGMs [12-13].

The experimental setup for processing of alloy/MMC FGM is fabricated in house. Fig. 1 shows the details of centrifuge casting machine and the solidified casting in the mold.

Optical microscope is used for microstructure characterization and an inverted microscope of Dewinter make interfaced with Metalife image analyzer software is used to capture and analyze the image. The image captured is analyzed for phase/volume fraction analysis (ASTM-E562 1995), (ASTM-E1245 1995), Si and SiCP distribution [14].

In the present work for Brinell Hardness testing the specimen is cleansed to remove dirt and oil on the surface prior to the testing. The tests are conducted as per ASTM E-10, the testing machine to IS-Specification 1754. As per ASTM standards, in this test a ball indenter of diameter 5mm and a load of 15.625 Kgs are selected.

In this study wear tests were conducted as per ASTM standards (ASTMG-99 1995) using Pin-on-Disc type wear testing machine (model TR-20LE, Ducom make). The maximum load capacity of the system is 200N. The rpm and the sliding speed of the disc were 0-2000rpm and 0-10m/s respectively. The disc is made of En-32 steel, having hardness value of HRC65 with dimensions of 160mm diameter and 8mm thickness is used [15].

3. Result and Discussion

3.1. Microstructure

The microstructure of the FGMMC with 2% SiC_P cast at 200, 300 and 400rpm is shown in Fig. 2.

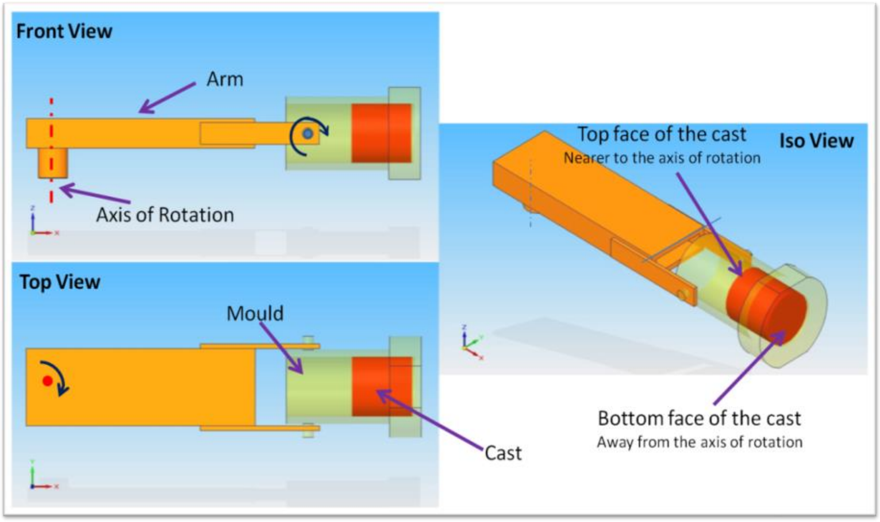

Figure 1. Centrifuge machine with its parts

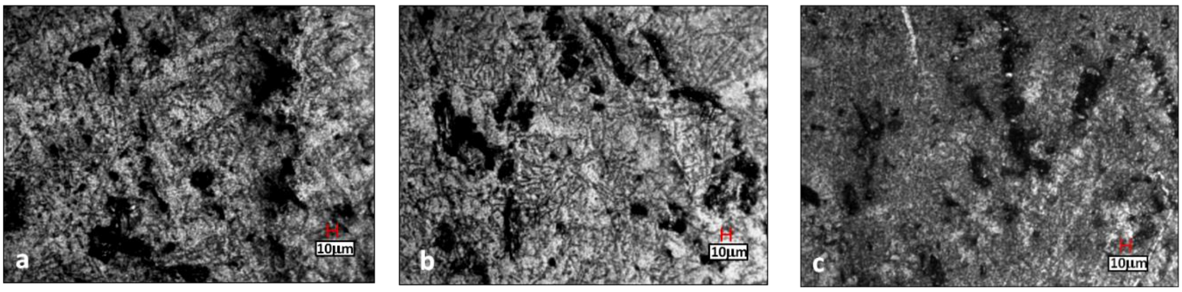

Figure 2. Microstructure of Al-17wt%Si-2% SiC_P system at 200, 300 and 400rpm

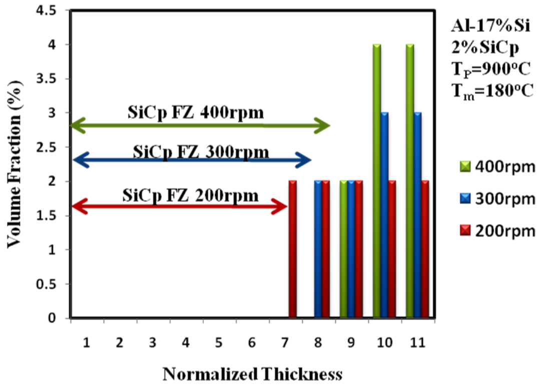

Figure 3. Distribution of SiCPalong the length of the sample for 2wt% reinforcement.

The segregation of SiC$_P$ is more at 400rpm when compared to the other two rpms. For 2% SiC$_P$reinforcement the amounts of enrichment at the lower surface of casting are 2%, 3% and 4% respectively at 200, 300 and 400rpm. The rim thicknesses of the SiC$_P$ rich zone from the bottom of the casting are 16mm, 12mm and 8mm respectively. The volume fraction of SiC$_P$ and SiC$_P$ free zone with respect to the bottom end are shown in Fig. 3.

With increase in volume fraction of SiC$_P$ from 2% to 4% the segregation of SiC$_P$ at the bottom end of the casting increased to 5, 7 and 8% at 200, 300 and 400rpm respectively, while the rim thickness remained same as in the case of 2% and further similar trend was observed at 6% SiC$_P$ with the amount of segregation increasing to 6%, 8% and 10% as shown in Fig. 4.

The distribution of SiC particles in the Al-17% Si castings is better when it is cast centrifugally casting method compared to other methods (Fig. 5). This is due to the fact that alloy solidification develops in a very constricted zone at the interfaces between particles; this helps in getting homogeneous nucleation of matrix because of rapid movement of particles in molten metal. During this time, the primary α-Al, which is developed in this zone, attracts SiC particles between thin primary α-Al phases. In the free particle zone, coarse primary α-Al are developed due to low under cooling. Therefore, coarse primary α-Al and thin granular eutectic Si phase are observed.

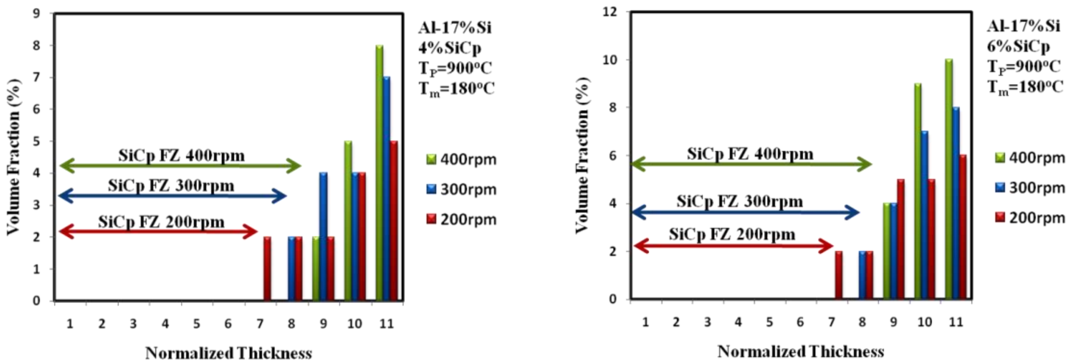

Figure 4. Distribution of SiC$_P$along the length of the sample for 4wt% and 6wt% reinforcement.

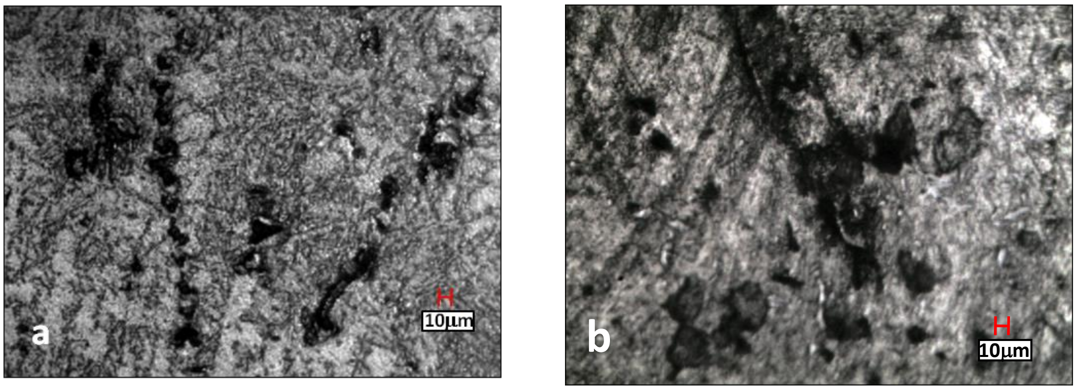

Figure 5. Microstructure of FGMMC by Centrifuge technique

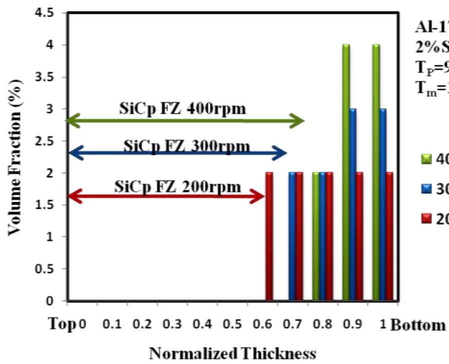

Figure 6. Distribution of SiC$_P$along the length of the sample for 2wt% reinforcement.

With increase in percentage (volume fraction) of SiCP to 4%, the segregation of SiCP at the bottom of the casting FGMMC measured was 7%, 7% and 5%, for 400, 300, 200rpm and the rim thickness changed to 8mm, 12mm and 16mm respectively. Similarly, at 6% SiCP the corresponding values were 8%, 7% and 6% and 8mm, 12mm and 20mm respectively as shown in Fig. 7.

3.1.1. Effect of rotational speed

During the centrifuge casting, segregation of particles takes place in the melt due to the 'G' force implied upon and the difference in densities between the particles and the melt, which in turn increase the movement of the particles. The solid particles are subjected to radial buoyancy (F_c) and radial moving velocity (V_c) as given by equations 4.1 and 4.2.

$$F_c = \frac{\pi d^3 (\rho_p - \rho_l)\omega^2 r}{6} \quad 4.1$$

$$V_c = \frac{d^2 (\rho_p - \rho_l)\omega^2 r}{18\eta_c} \quad 4.2$$

Where d is the diameter of the reinforced particle (m), $\rho_p$is the density of the particle and $\rho_l$is the density of the liquid (kg/m^3). The distance of the particles from the axis of rotation (m) is given by 'r', angular velocity of the mold ω in (rad/s).η_c is the viscosity of the liquid with solid particles (Pa.s). The particles move toward the top part of the casting, if $\rho_p<\rho_l$, then $V_c<0$.the particles move away from the axis of rotation (bottom of the casting), if $\rho_p>\rho_l$, then $V_c>0$. In this Al-Si- SiC_P system, as the SiC_P is denser than that of the liquid metal, the particles are forced tp move towards the bottom surface of the casting[16].

From the Figs. 6 and 7 it can be observed that the thickness SiC_P segregated zone decreases with the increase in centrifugal force of the rotating mold.

This can be further explained as the effect of chilling. At lower rotational speeds, the velocity of the solidification front is more than the particle velocity. This results in melt solidifying firstly and no new particles can reach this region. The time required to solidify increases as the solidification front moves to the core of the casting, which in turn gives the particles more time to settle in the casting, which induces a segregated zone. As the centrifugal force on the particles increases, the solidification front leads to a shortened section. It has been observed that the heat transfer coefficient for Al at the metal/mold interface increases with an increase in the centrifugal force and at a higher forces, a induced high pressures of liquid metal on the solidified layer, results better heat transfer coefficient between the mold wall and solidified layer interface [17].

3.1.2. Effect of Temperature

Increase teeming temperature, decreases thickness of the SIC_P rich zone. To start the solidification a large quantity of heat must be extracted from the melt of Al-Si-SiC_P when the temperature is increased. Hence, this extra time gives more time to solidify forFGMMCs, the reinforcement particles get more time to segregate, forming a rich segregation zone. In addition, at higher mold temperature, the rate of heat extraction from the melt to the mold is reduced due to negative thermal gradient. This increases the solidification time, giving more time for particulates to segregate and pack into rich thinner zones.

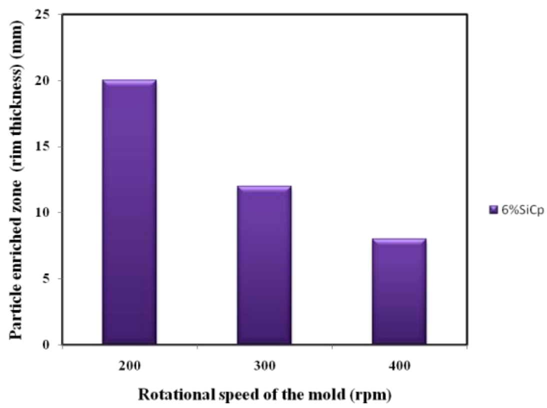

Figure 8. Effect of speed on rim thickness

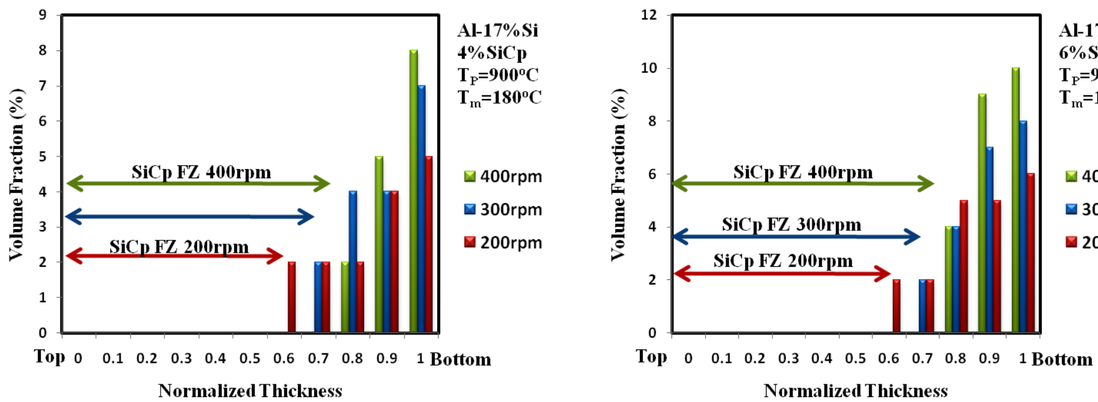

Figure 7. Distribution of SiC_Palong the length of the sample for 4wt% and 6wt% reinforcement.

3.1.3. Effect of Matrix and Reinforcement

At 2% and 4% reinforcement, the segregation of the SiC particles towards the bottom is almost increased by 100% whereas for 6% reinforcement it is 66% in Al-17wt%Si. This may be attributed to the fact that the increase in % of the SiC has decreased the fluidity of the system which in turn decreased segregation. Moreover, it has been observed that cooling rate is enhanced with increasing mold rotation speed because of better heat transfer; i.e high centrifugal forces produce a tight contact between the mold wall and the melt. Due to the presence of thermally insulating SiC particles, higher SiC particulate contents reduce the amount of heat to be removed and this initiates an increase in the solidification rate. High cooling rate gives rise to a much finer cast microstructure [18].

The distribution pattern of centrifuge cast silicon carbide particles reinforced Al-17wt%Si alloy show that there is a more SiC enriched zone. This is obviously due to solidification range being larger in 17% alloy i.ethe difference in freezing range and viscosity of the alloy. The SiC particle distribution graphs show that the gradient of SiC is more for Al-17wt%.At 200rpm the SiC particles are spread for 16mm from the bottom.

It has been noted that the segregation for SiC particles towards the bottom end of the casting depends not only on the speed of rotation of the mold but also on the matrix. The ‘G’ factor forces the SiC particle towards the bottom end along its direction due to the density difference it has got with melt. The content of the Si in the matrix affects the fluidity, which reduces the temperature range solidification which in turn increases the rate of phase transformation allowing very less time for particle movement.

3.2. Hardness

As evident from the Figures 9 to 4.80 in case of FGMMCs there is a substantial increase of hardness at the bottom portion of the specimen. Best results were obtained for 6% SiC_p reinforcement for both the matrix materials. At the top region, leading to segregation of Si, hardness. Thus, a middle region of comparatively lower hardness is sandwiched between harder top and bottom.

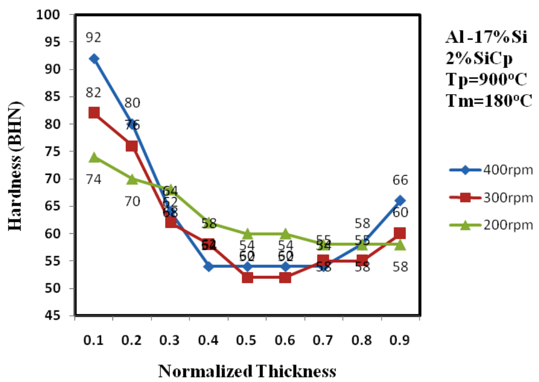

Figure 9. Hardness values along the length of the casting for Al-17wt%Si-2wt% SiC_P FGMMC.

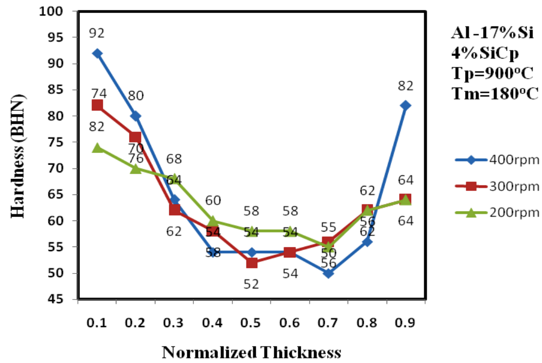

Figure 10. Hardness values along the length of the casting for Al-17wt%Si-4% SiC_P FGMMC.

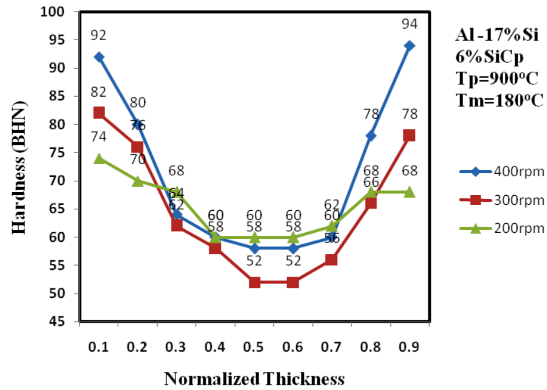

Figure 11. Hardness values along the length of the casting for Al-17wt%Si-6% SiC_P FGMMC.

For Al-17wt% Si matrix alloy a reinforcement of 2% SiC_P yielded a maximum hardness of about 66BHN at 400rpm while for 4% and 6% the hardness was found to be 82 and 94BHN.

In centrifugal castings solidification progresses radially inwards from the outside surface. This is because that the outside and bottom surfaces are in contact with the mold surface and the top surface is free. The liquid melt undergoes shear during solidification, and this prevents the formation of a crust on the top. High pressures developed due to the ‘G’ force, makes the air gap smaller and the formation of air gap is delayed. This in turn increases the heat transfer rate at the outer surface. High rates of heat transfer, and therefore solidification, leads to refined structure. We can see that by reducing the heat transfer rate, the rate of solidification can be reduced. This reduced solidification rate gives more time for the SiC_P to segregate towards the bottom. The segregation can be enhanced by increasing the pouring temperature and mold temperature.

When the mold temperature is low (room temperature) and the liquid melt temperature is high, a sharp gradient of the temperature is noted at the mold. This difference in temperature causes faster heat transfer resulting higher solidification rate at the mold-liquid interface. As the mold temperature is increased, the temperature gradient gets reduced resulting in lower solidification rate. More time is available for SiC particles to segregate better under G forces, and this results in higher hardness compared to molds which have not been subjected to higher mold temperatures at a slower solidification rate [19-21].

3.3. Wear

The top and bottom regions of the specimens were subjected to wear test at ambient temperature under dry sliding condition. The aim of this study is to find the volume loss, coefficient of friction variation under different loads.The loss of the material due to several wear regimes for the FGMMCs castings with 2, 4 and 6% SiC_P reinforcement in Al-17%Si are studied. The dry sliding nature of the Al-Si/ SiC_P FGM under different loads of 40, 60 and 80N at 1.446 m/s sliding speed is evaluated.

Volume loss of Al-17wt%Si-SiC_P FGM composite at both top end and bottom end of the casting is determined with respect to the applied load at a sliding speed of 1.466 m/s. The weight loss of both the ends having SiC_P and Si respectively increases with the addition of the load. The bottom end (having segregated SiC_P) showed lower volume loss. The top end of the casting has segregated Si and thus shows lower volume loss compared to the middle region which has neither the SiC_P nor the primary Si segregation [22-25].

From Figs. 12 to 14 at different test loads, for 2 volume percent of SiC_P reinforcement in Al-17%Si alloy/MMC, SWR decreased by about 11.3%, 8% and 10.34% at 40, 60 and 80N respectively at sliding speeds of 1.446m/s for castings produced at 400 rpm compared to 200rpm. For 4% of SiC_P reinforcement produced at 400rpm it has been noted that the SWR decreased by 15.8, 14.46 and 13.8% for 40, 60 and 80N test loads in comparison with 2% of SiC_P reinforcement FGMMC. But there is a significant improvement in case of 6% SiC_P reinforcement wherein the SWR decreased by 36.9%, 30.8% and 23.2% for 40, 60 and 80N test loads in comparison with 4% of SiC_P reinforcement FGMMC. This clearly shows that the additions of SiC_P to Al-Si alloys enhance the strength of matrix, reducing contact area at any given load leading to reduction in SWR. From these results, it is clear that the effect of increase of test load in improving the wear resistance is higher in MMCs with harder reinforcement particles embedded in softer matrix and vice versa [26-28]. The decrease of SWR with increase in test load can be attributed to higher strain hardening of matrix.

The variation of Coefficient of Friction (COF) is shown in Figs. 15 to 17. The COF increased to a maximum as the rotating disc, reached its set speed on starting and then smoothly decreased to a constant value. At the start of the test, due to changes in pin and disc surfaces, the COF rises with time in the beginning and remains constant. The Al-Si eutectic with 23% free Si at the top end apparently shows lower COF. Whereas the lower end shows higher COF. The reinforcement of the 2% SiC_P led to no significant improvement in terms of wear and its properties. Comparison of COF at the bottom end of both FG alloy and SiC_P 2% reinforced FGMMC has shown a very little difference at all test loads.

With further increase in volume percent of SiC_P the coefficient of friction was found to decrease at the bottom end for different normal loads. On an average at different loads and at 1.446m/s, for an increment of 2 volume percent of SiC_P reinforcement, the coefficient of friction decreased by about 4% and COF decreased by 7% [29-32].

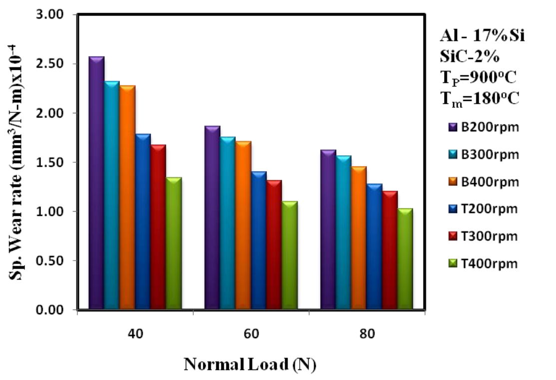

Figure 12. Specific Wear rate of Al-17wt%Si-2% SiC_P FGMMC.

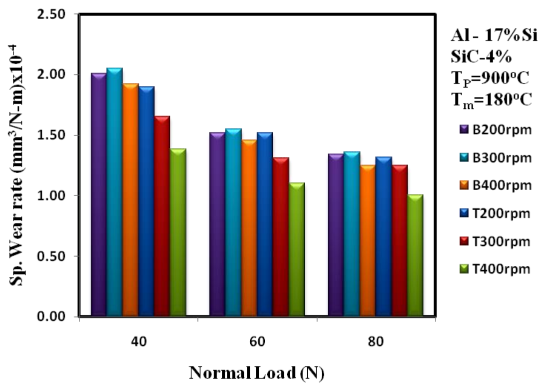

Figure 13. Specific Wear rate of Al-17wt%Si-4% SiC_P FGMMC.

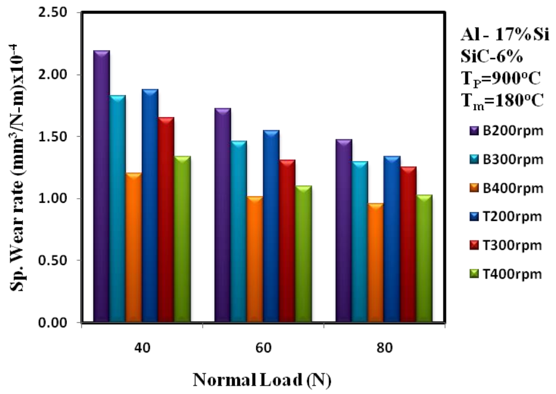

Figure 14. Specific Wear rate of Al-17wt%Si-6% SiC_P FGMMC.

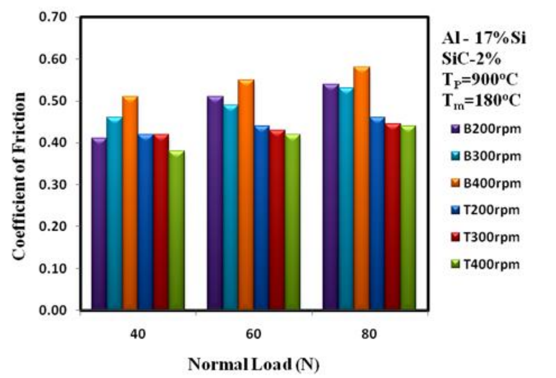

Figure 15. COF of Al-17wt%Si-2% SiC_P FGMMC.

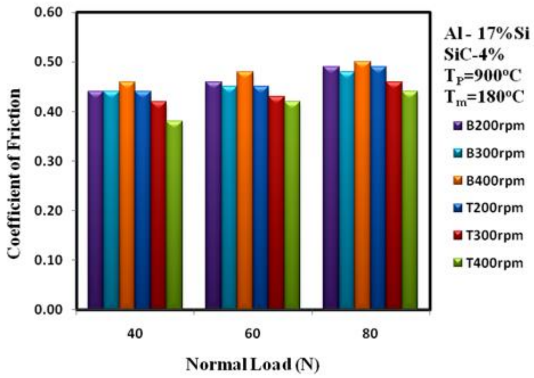

Figure 16. COF of Al-17wt%Si-4% SiC_P FGMMC.

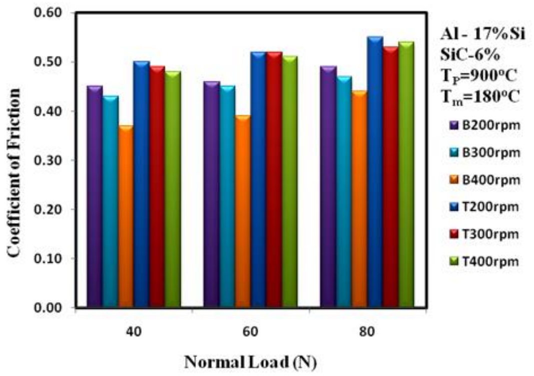

Figure 17. COF of Al-17wt%Si-6% SiC_P FGMMC.

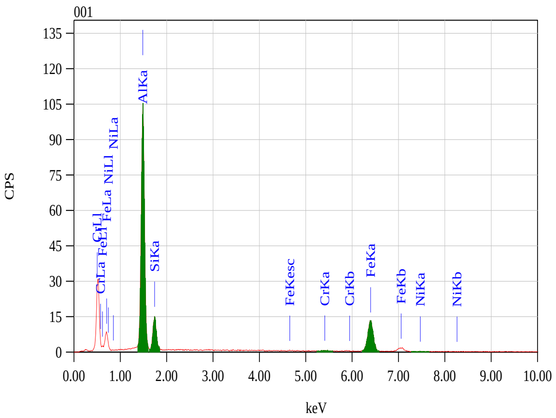

Figure 18. EDS spectrum showing material transfer of Fe on to Pin surface

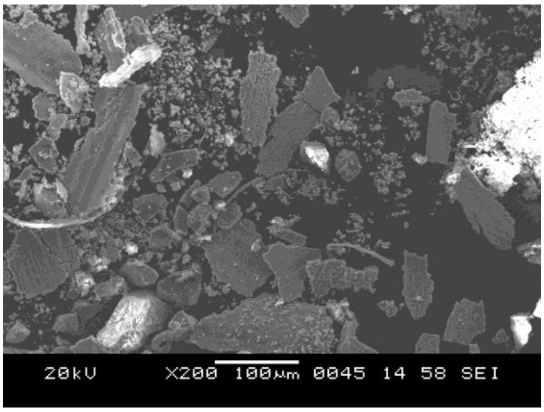

Figure 19. Flake or sheet like wear debris of delamination

It is seen that FGMMCs possess very good wear resistance. In this FGMMCs, the load is supported by SiC particles, which decrease the friction coefficient because of the lesser contact area between specimen and disc surface. This also prevents the surface from getting wear out from the hard little asperities, which intends to scratch and cut the surface. However, under high load, the reinforcing particles can longer protect the surface and does not remain stable. The abrasion grooves formed are very distinct in worn surfaces due to the ploughing and micro-cut action. During the wear test, it has been observed that flake type and stringer type debris are formed (material loss). The delamination occurs due to the removal of surfaces because of increase in shear strain near the cracks. It clearly shows that the main cause of wear is delamination, which causes cracking or breaking of the reinforcement and the matrix, results in weakening the wear resistance.

4. Conclusion

1. The segregation of SiC_P is more at 400rpm when compared to the other two rpms. For 2%SiC_P the rim thicknesses of the SiC_P rich zone from the bottom of the casting are 16mm, 12mm and 8mm respectively. Similarly, for 4% the rim thickness changed to 8mm, 12mm and 16mm and 8mm, 12mm and 20mm for 6%.
2. The segregation for SiC_P towards the bottom end of the casting depends not only on the speed of rotation of the mold but also on the matrix. The 'G' factor forces the SiC_P towards the bottom end along its direction due to the density difference between the melt and the SiC_P.
3. For Al-17wt% Si matrix alloy a reinforcement of 2% SiC_P yielded a hardness of about 66BHN at 400rpm while for 4% and 6% the hardness was found to be 82 and 94BHN.
4. The additions of SiC_P to Al-Si alloys enhanced the strength of matrix, reducing contact area at any given load leading to reduction in SWR. The effect of increase of test load in improving the wear resistance is higher in MMCs with harder reinforcement particles embedded in softer matrix and vice versa. The decrease of SWR with increase in test load is attributed to higher strain hardening of matrix.

Declaration:

Compliance with ethical standards: The authors declare that they have no conflict of interest.

References

[1] Gui M.-C.,Wang D.-B.,Wu J.-J.,Yuan G.-J. &Li C.-G.Microstructure and mechanical properties of cast (Al–Si)/SiCp composites produced by liquid and semisolid double stirring process. Materials Science and Technology, vol 16, pp 556-563

[2] Bai Pramila, Rameash B S, M K Surappa, (1992). Dry sliding wear of A356-Al-SiCp composites. *Wear* , vol 157, pp 295-304.

[3] Wang, K., Jiang, T., Huang, Z. et al. Mechanical and thermal expansion properties of SiCp/ZAlSi9Mg composites produced by centrifugal casting. J. Wuhan Univ. Technol.-Mat. Sci. Edit. 31, 197–203 (2016).

[4] Watanabe Y, Yamanaka N, Fukui Y, (1998). Control of composition gradient in a metal-ceramic functionally graded

material manufactured by the centrifugal method. *Composites part A* , 29A, 595-560.

[5] Castro Rodri´guez, Kelestemur, (2002). Microstructure and Mechanical behavior of functionally graded Al A359/SiCp composite. Materials Science and Engineering A , 323, 445-456.

[6] CastroRodri´guez, Kelestemur, (2002). Processing and microstructural characterization of functionally gradient Al A359/SiCp composite. Journal of materials Science , 37, 1813-1821.

[7] Verma, R.K., Parganiha, D. & Chopkar, M. A review on fabrication and characteristics of functionally graded aluminum matrix composites fabricated by centrifugal casting method. SN Appl. Sci. 3, 227 (2021). https://doi.org/10.1007/s42452-021-04200-8

[8] Ramesh Babu Narayanappa, Ramesh Motagondanahalli Rangarasaiah, Kiran Aithal Subbanna, Veeresh Kumar Shivakumar, and Manjunath H. Narayana Shetty , "Study of dry sliding wear behavior of Al-Si-C FG alloy developed through directional solidification", AIP Conference Proceedings 2080, 020009 (2019) https://doi.org/10.1063/1.5092892

[9] N. Ramesh Babu, M. R. Ramesh, R. N. Murthy, J. Sudheer Reddy, S. Kiran Aithal, and H. N. Manjunath, 'Study of tribological characteristics of AlSi based directional solidified FGM with graphite end chill', AIP Conference Proceedings 2274, 030045 (2020); https://doi.org/10.1063/5.0022478

[10] C.G. Shivaprasad; Kiran Aithal; S. Narendranath; Vijay Desai; P.G. Mukunda, Effect of combined grain refinement and modification on microstructure and mechanical properties of hypoeutectic, eutectic and hypereutectic Al-Si alloys, International Journal of Microstructure and Materials Properties, 2015 Vol.10 No.3/4, pp.274 - 284

[11] Shivaprasad Channappagoudar, Kiran Aithal, Narendranath Sannayallappa, Vijay Desai, Pudukottah Gopaliengar Mukundab, The Influence of the Addition of 4.5 wt.% of Copper on Wear Properties of Al-12Si Eutectic Alloy, Jordan Journal of Mechanical and Industrial Engineering, vol 9 Number 3, pp217-221.

[12] Kiran Aithal, Narendranath S, Vijay Desai, P G Mukunda "Microstructure, Hardness and Wear Characterization of Al-Si FGMs"- Vol 58, No.5, May 2012, Indian Foundry Journal

[13] Ramesh Babu N, Ramesh M R, Kiran Aithal S 'Evaluation of Mechanical and Tribological Properties of Directionally Solidified Al-Si Based FG Composite' Silicon (2019)

[14] Pace, (2011). Metallographic hand book. Tucson, Arizona: Pace Technologies.

[15] Ludema K. C. (2000). Sliding and Adhesive wear. ASTM, Friction, Lubrication and Wear technology, Vol18. ASTM International.

[16] Birman victor, Larry W Byrd, (2007). Modeling and Analysis of Functionally Graded Materials and Structures. Transactions of the ASME , 60, 195-215.

[17] Shamsi, Mehrotra, (1993). A two-dimensional heat and fluid-flow model of single-roll continuous-sheet casting process. Metallurgical And Materials Transactions B , Volume 24, Number 3, 521-535,

[18] Watanabe Y, Sato R, Kim IS, Miura S, Miura H, (2005). Functionally Graded Material Fabricated by a Centrifugal Method from ZK60A Magnesium Alloy. *Materials Transactions* , Vol. 46, No. 5, pp. 944 to 949.

[19] A.R.I. Kheder,G.S. Marahleh, D.M.K. Al-Jamea, (2011), Strengthening of Aluminum by SiC, Al_2O_3 and MgO, Jordan Journal of Mechanical and Industrial Engineering, Vol. 5, No. 6, pp. 533 to 541.

[20] Kasim M. Daws, Zouhair I. AL-Dawood, Sadiq H. AL-Kabi, (2008),Selection of Metal Casting Processes: A Fuzzy Approach, Jordan Journal of Mechanical and Industrial Engineering, Vol. 2, No. 1, pp. 45 to 52.

[21] Shivaprasad Channappagoudar, Kiran Aithal, Narendranath Sannayallappa, Vijay Desai, Pudukottah Gopaliengar Mukunda, (2015), ''The Influence of the Addition of 4.5 wt.% of Copper on Wear Properties of Al-12Si Eutectic Alloy'', Jordan Journal of Mechanical and Industrial Engineering, Volume 9, Number 3, Pages 217 – 221.

[22] Mondal D P, Das S, Rao R N, Singh M, (2005). Effect of SiC addition and running-in-wear on the sliding wear behaviour of Al–Zn–Mg aluminium alloy. *Materials Science and Engineering A* , Vol 402, 307–319.

[23] Alam, R I Marshall and S Sasaki (1996). Metallurgical and tribological investigations of aluminum bronze bushes made by a novel centrifugal casting technique. *Tribology International*, 29, No 6, 487-492.

[24] ASTMG-99, (1995). standard test method for wear testingwith a pin-on-disk apparatus. *ASTM standards* .

[25] Bai Pramila, Biswas S K, (1987). Charecterization of dry sliding wear of al-Si alloys. wear , Vol 120, 61-74.

[26] Bai Pramila, Rameash B S, M K Surappa, (1992). Dry sliding wear of A356-Al-SiCp composites. Wear , vol 157, pp 295-304.

[27] Blau, (1981). Interpretation of the friction and wear break-in behavior of metals in sliding contact. Wear , 71 (1), 29.

[28] Basavakumar, Madhusudan charaborty, Mukunda, (2007). Influence of grain refinement and modification on dry sliding wear behaviour of Al-7Si and Al-7Si-2.5Cu cast alloys. *Journal of Materials processing technology* , Vol 186, 236-245.

[29] Reddy T V S, Dwivedi D K, Jain N K, (2009). Adhesive wear of stir cast hypereutectic Al–Si–Mg alloy under reciprocating sliding conditions. *Wear* , 266, 1–5.

[30] Velhinho, Botas, Ariza, Gomes, Rocha, (2004), Tribocorrosion Studies in Centrifugally Cast Al-Matrix SiCp - reinforced Functionally Graded Composites. *Material Science Forum* , Vol 455-456, 871-875.

[31] Zhiqiang S, Di Z, Guobin L, (2005). Evaluation of dry sliding wear behavior of silicon particles reinforced aluminum matrix composites. *Materials and Design* , Vol26, 454–458.

[32] K S Chethan, S Kiran Aithal, B K Muralidhara,(2019) Enhancing the mechanical and tribological properties of solid cylindrical aluminum specimen by reinforcing alumina nanoparticulate through centrifuge casting technique. Mater. Res. Express 6 1065g9, vol. 6,no.10, pp.1-10.

المملكة الأردنية الهاشمية

الجامعة الهاشمية

المجلة الأردنية
للهندسة الميكانيكية والصناعية

JJMIE

مجلة علمية عالمية محكمة

تصدر بدعم من صندوق البحث العلمي

http://jjmie.hu.edu.jo/

ISSN 1995-6665

المجلة الأردنية للهندسة الميكانيكية والصناعية

المجلة الأردنية للهندسة الميكانيكية والصناعية: مجلة علمية عالمية محكمة تصدرعن الجامعة الهاشمية بالتعاون مع صندوق دعم البحث العلمي والابتكار- وزارة التعليم العالي والبحث العلمي في الأردن.

ترسل البحوث إلى العنوان التالي

رئيس تحرير المجلة الأردنية للهندسة الميكانيكية و الصناعية

الجامعة الهاشمية
كلية الهندسة
قسم الهندسة الميكانيكية
الزرقاء - الأردن

هاتف : 3903333 5 00962 فرعي 4147

Email: jjmie@hu.edu.jo

Website: www.jjmie.hu.edu.jo